

THESIS FOR THE DEGREE OF DOCTOR OF PHILOSOPHY

**Investigation of Issues Related to Electrical Efficiency
Improvements of Pump and Fan Drives in Buildings**

JOHAN ÅSTRÖM



Department of Energy and Environment
CHALMERS UNIVERSITY OF TECHNOLOGY
Göteborg, Sweden 2011

Investigation of Issues Related to Electrical Efficiency Improvements of Pump and Fan
Drives in Buildings
JOHAN ÅSTRÖM
ISBN 978-91-7385-528-0

© JOHAN ÅSTRÖM, 2011.

Doktorsavhandlingar vid Chalmers tekniska högskola
Ny serie nr. 3209
ISSN 0346-718X

Department of Energy and Environment
Chalmers University of Technology
SE-412 96 Göteborg
Sweden
Telephone +46 (0)31-772 1000

Chalmers Bibliotek, Reproservice
Göteborg, Sweden 2011

Abstract

This thesis deals with issues regarding energy efficiency of building related pump and fan drive systems. Different Induction Motor (IM) and permanent magnet motor drive systems are analyzed with focus on energy efficiency. A 4-pole, 4kW IM is the focus of the IM investigation, where different motor efficiency labels, (eff1/IE2, eff2/IE1 and eff3), different control strategies and switching schemes of the frequency converter are analyzed. Simulations as well as measurements are performed and a close correlation of the results is found. Furthermore, efficiency consideration regarding sizing of the IM for a given load are analyzed. It is shown that an oversized IM gives a higher efficiency than using one with the proper rating, provided that an adequate control of the motor supply is used.

A commercially available 375W BLDC and a 4kW PMSM are analyzed using FEM calculations coupled with circuit simulations, evaluating a large range of current control strategies.

It is shown that different zero voltage vector placements have a large impact on the iron losses in the motor as well as on the switching losses in the converter, especially at light load. It is further shown that the efficiency of a BLDC motor can be increased at rated operation by controlling it as a PMSM.

A comparison of inner and outer rotor BLDC motor is done. It is found that the efficiency easily can be increased for the 375W BLDC motor by changing the design to an outer rotor motor. It is shown that the outer rotor motor is more suitable when using ferrite magnet materials, increasing the potential of making a more energy efficient motor. Furthermore, the impact of iron grade and magnet material is quantified with respect to energy efficiency and power density.

An investigation of the energy efficiency difference between a 1.2kW BLDC and a 1.2kW PMSM motor is carried out. Two motor types are designed and constructed, showing that the BLDC motor has the highest efficiency in the whole operating range, as well as the lowest losses in the inverter stage due to decreased switching losses. The simulation result also verifies the modeling methods which includes a good accuracy regarding the iron loss modeling.

The simulation results of the IM are used in order to analyze the potential saving for different load profiles. The general conclusion is that economical savings will be made

during the life time of the drive system, both for an IM and frequency converter replacement. The analysis also show that the choice between an eff2 and eff1 IM always generate the highest energy saving for the eff1 IM in economical terms, for the given load profiles, including the increased cost for an eff1 motor. The potential savings between a 4kW IM and a 4kW commercially available PMSM are also quantified. It is shown that the PMSM in general is the best choice, for the given load profiles, providing an annual energy saving of 700-2600kWh. Finally quantification of the potential savings between a 375W IM, a 375W commercially available BLDC motor and a proposed 375W BLDC outer rotor motor are presented. The result presents an annual saving of 200-400kWh when replacing a commercially IM with the BLDC motor. In addition, 200-400 kWh can be saved annually using the proposed BLDC motor design compared with the original BLDC motor.

Index Terms: Induction motor, permanent magnet motor, frequency converter, loss model, zero vector placement, efficiency measurement, HVAC load profiles and saving potential.

Preface

This thesis is a part of a larger project that has been conducted in cooperation with the division of Building Service Engineering and the division of Electric Power Engineering, within the department of Energy and Environment at Chalmers. The common objective of this project has been to identify saving potentials in building related pump and fan operation. The focus of the work at the division of Building Service Engineering has been on the system side of the applications, whereas, the focus on the electrical part of the system has been the main target for the work conducted at Electric Power Engineering. It is of course not possible to make a clear distinction between the two areas, hence a cooperation has been important and valuable. This thesis will mainly deal with the electrical part of the system but in some extent also discuss Building Service related issues.

Acknowledgements

The financial support given by Göteborgs Energi, Energimyndigheten and Formas is gratefully acknowledged.

In addition, twenty companies have been involved in the project mainly by attending project meetings. Special thanks to FläktWoods, Grundfos, Systemair, Swegon, and Wilo for providing the project with test objects and for the time they have invested in many valuable company visits.

I would like to thank my supervisor Prof. Torbjörn Thiringer for his supervision, his encouraging attitude, constructive feedback and for many interesting discussions.

I would also like to thank all my colleges and especially Mikael Alatalo and Stefan Lundberg for interesting discussions and their excellent inputs. Also a special thank to Magnus Ellsén, Robert Karlsson and Aleksander Bartnicki for their help with many practical things during this time. Also, a special thank to Andreas Karvonen for many constructive discussions on a daily basis.

Finally, I would like to thank Prof. Per Fahlén and PhD student Caroline Markusson at the division of Building Service Engineering and Dr. Lennart Jagemar at CIT Energy Management for a good cooperation.

Johan Åström
Göteborg, Sweden
June, 2011

Contents

Abstract	iii
Preface	v
Acknowledgements	vii
Contents	ix
1 Introduction	5
1.1 Problem Background	5
1.2 Literature overview	6
1.3 Purpose of the thesis and contributions	7
1.4 Outline of Thesis	8
1.5 List of publications	9
2 Drives for pumps and fans	11
2.1 Induction motor	11
2.1.1 IM operation	12
2.1.2 Loss components	14
2.2 Permanent magnet motors	15
2.2.1 Brush Less DC motors and PMSM	15
2.2.2 Loss components	17
2.3 Frequency converters	19
2.3.1 Power Diodes	23
2.3.2 MOSFETs	24
2.3.3 IGBTs	26
2.4 Pumps and fans as loads	29
2.5 Load profiles	29
2.5.1 Load profile A	31
2.5.2 Load profile B	31
2.5.3 Fictive load profiles	31

3	Modeling of electrical drive systems	33
3.1	Induction motor	33
3.1.1	Dynamic modeling suitable for converter supply	33
3.1.2	Steady state modeling	37
3.1.3	Parameter identification	38
3.2	Permanent magnet motor modeling	41
3.2.1	Dynamic modeling of a BLDC motor	41
3.2.2	FEM modeling of Permanent magnet motors	42
3.3	Loss modeling of frequency converters	44
4	Field measurements on HVAC applications	47
4.1	Field measurements	47
5	Efficiency determination of different Induction motor drive systems	53
5.1	Induction motor setup	53
5.1.1	Comparison between different motor designs	53
5.1.2	Energy optimal control of the Induction motor	54
5.1.3	Efficiency calculation result of different design and control techniques	55
5.2	Influence of over sizing on the efficiency for an IM	56
5.2.1	Parameters identification for the case study	58
5.2.2	Calculation results	59
5.3	Frequency converter setup	61
5.3.1	Sinuousdial PWM	62
5.3.2	Sinuousdial PWM using third harmonic injection	63
5.3.3	Space Vector Modulation	63
5.3.4	Theoretical comparison of different PWM schemes	70
6	Efficiency determination of different permanent magnet motor drive systems	73
6.1	Model setup of a 375W BLDC motor in Maxwell/Simplorer	73
6.1.1	Setup of the 375W BLDC motor in Maxwell	73
6.1.2	Frequency converter setup in Simplorer	75
6.1.3	Iron loss calculation	76
6.2	Simulation result	78
6.2.1	Motor commutation	78
6.2.2	Calculated quantities	80
6.3	Efficiency comparison between different control schemes	83
6.3.1	Advanced angle BLDC control	83
6.3.2	Field Oriented Control	83
6.3.3	Basic hysteresis control	84
6.3.4	Direct Torque/Current Control	85
6.3.5	PMSM vs BLDC control	93

6.3.6	Advanced angle BLDC control	102
6.3.7	4kW PMSM	103
6.3.8	Influence of switching frequency	108
6.4	Comparison between 2D and 3D modeling	108
7	Efficiency difference between different PMSM and BLDC motor designs	111
7.1	Basic design considerations	111
7.2	Modifications of the original 375W BLDC	112
7.2.1	Replacement of magnet material	113
7.2.2	Inner vs outer rotor motor	113
7.3	Design of a 1.2kW 1000rpm PMSM and BLDC	117
7.3.1	Initial, analytical design settings	117
7.3.2	Influence of the number of stator turns	118
7.3.3	Simulation result PMSM vs BLDC	118
8	Experimental investigation of different PWM control schemes for IM	123
8.1	Measurement setup	123
8.1.1	Converter leg	123
8.1.2	Gate driver	125
8.2	On-state measurement	130
8.3	Temperature calibration	132
8.4	Measurement of switching transitions	132
8.5	Measurements of the frequency converter losses at IM operation	136
8.5.1	SVM	136
8.5.2	Varying switching frequency	140
8.5.3	DPWM60 and DPWM30	142
8.5.4	Comparison of the different switching schemes	142
8.5.5	Influence on IM efficiency	145
8.6	Efficiency measurements at optimal V/Hz operation	145
9	Experimental investigation of BLDC and PMSM drives	147
9.1	Measurement setup of 375W	147
9.2	Measurement results of the original 375W BLDC	148
9.3	Measurement setup for the 4kW PMSM	150
9.4	Measurement results of a 1.2kW PMSM and BLDC motor	152
9.4.1	1.2kW PMSM	152
9.4.2	1.2kW BLDC	154
10	Energy potential savings for different load profiles	157
10.1	Energy consumption calculation	157
10.2	Induction motor drive setups	158

Contents

10.2.1 Load profile A	159
10.2.2 Load profile B	162
10.2.3 Load profile C	164
10.2.4 Load profile D	166
10.3 Evaluation of the potential saving	168
10.4 BLDC, PMSM vs AM	168
11 Concluding Remarks and future work	171
11.1 Concluding Remarks	171
11.1.1 Induction motor drive system	171
11.1.2 Permanent magnet motor drive systems	172
11.1.3 PMSM/BLDC vs IM	173
11.2 Proposals of Future Work	173
References	175
A Derivation of maximum active power for non sinusoidal voltage and current	181

Symbols and Glossary

Symbols

A_{to}	Area of the flux path in the stator tooth (mm ²)
A_{save}	Annual saving (SEK/year)
B_{to}	Magnetic flux density in the stator tooth (T)
b_f	Friction constant of bearings in a motor (Nms/rad)
D_m	Motor diameter (mm)
$E, e(t)$	Induced voltage in the stator winding (V)
H	Pressure provided by a pump/fan (m)
I_0	Initial investment cost (SEK)
I_{sN}	Rated motor current (A)
L_m	Y-equivalent, magnetizing inductance in an IM (H)
$L_{\sigma r}$	Y-equivalent, rotor leakage inductance (H)
$L_{\sigma s}$	Y-equivalent, stator leakage inductance (H)
\mathbf{L}_{rr}	Rotor inductance matrix (H)
\mathbf{L}_{rs}	Rotor-stator inductance matrix (H)
\mathbf{L}_{sr}	Stator-rotor inductance matrix (H)
\mathbf{L}_{ss}	Stator inductance matrix (H)
J	Moment of inertia (kgm ²)
M_{xy}	Mutual inductance in pahse x caused by phase y (H)
NPV	Net present value (SEK)
n_N	Rated speed of a motor (rpm)
N_r	Number of stator turns ()
p	Number of pole pair ()
P_c	Conductive losses in a semiconductor (W)
P_{core}	Core losses (W)
P_{Cu}	Resistive losses in the stator windings (W)
P_{fric}	Friction losses (W)

P_{mec}	Mechanical output power (W)
P_{sw}	Switching losses (W)
P_{mecN}	Rated mechanical power (W)
P_T	Transistor losses (W)
P_F	Freewheeling diode losses (W)
Q	Flow provided by a pump/fan (m^3/h)
R_c	Y-equivalent core resistance (Ω)
R_g	Gate resistance (Ω)
$R_{stray50Hz}$	Y-equivalent stray resistance at 50Hz (Ω)
R_s	Y-equivalent stator resistance (Ω)
R_r	Y-equivalent rotor resistance (Ω)
T_e	Electromechanical torque (Nm)
T_{Life}	Life time of an installation (year)
T_p	Payback time (years)
T_{sw}	Time of the switching period (s)
V_s	DC-bus voltage (V)
V_{gs}	Gate-source voltage (V)
W_{cost}	Price of 1kWh (SEK)
W_g	Air-gap length (mm)
W_m	Magnet thickness (mm)
W_o	Slot opening (mm)
W_y	Stator yoke width (mm)
W_t	Stator tooth width (mm)
Ψ	Flux linkage (Wb)
φ_1	Phase angle (fundamental) ($^\circ$)
ω_s	Synchronous speed (rad/s)
ω_r	Rotor speed (rad/s)
Θ_m	Rotor magnet embrace ($^\circ$)
Θ_r	Rotor position ($^\circ$)

Abbreviations

BLDC	Brushless DC
DCC	Direct current control
DCM	DC-machine
DPWMMAX/MAX	Discontinuous pulse with modulation that only using SV7 or SV0
DPWMM60	Discontinuous pulse with modulation using SV0 and SV7 in order to stop the switching in each phase leg for 60°, symmetrically around the peak of the phase voltage
DPWMM30lag	Discontinuous pulse with modulation using SV0 and SV7 in order to stop the switching in each phase leg for 60°, lagging the peak of the phase voltage with 30°
DTC	Direct torque control
EPBD	EU directive on the energy performance of buildings
FEM	Finite element method
FOC	Field oriented control
HVAC	Heating ventilation and air conditioning
ICP	Individual current control of the phase currents
IEC	The international electrotechnical commission
IGBT	Insulated gate bipolar transistor
IM	Induction motor
MOSFET	Metal oxide field effect transistor
OEM	Original equipment manufacturer
PMSM	Permanent magnet synchronous motor
PWM	Pulse width modulation
SVI	Space vector control of the current vector choosing the zero vector that leaves the switch with the highest current magnitude at its on-state during the zero vector activation
SVM	Space vector modulation
SVMSW	Same as SVI but the zero vector that needs the lowest number of switches will be activated
SVML	Same as SVI but the zero vector that results in the lowest switching losses will be activated
EMC	Electromagnetic compatibility
EMI	Electromagnetic interference

Contents

Chapter 1

Introduction

1.1 Problem Background

A common goal of nations world wide is to produce and supply electricity in a way that is safe and environmentally friendly to the lowest cost possible. However, the majority of energy production causes negative effects on the environment and many environmental experts points out the connection between CO₂ emission and the increase of global mean temperature. In order to reduce the energy consumption from non renewable energy sources, it is not only important to increase the use of renewable energy sources but also to reduce the energy use itself. Today, the electric power consumption in Sweden accounts for 125TWh where 25% is consumed by the permanent installations in the building sector (industries excluded), where pumps and fans accounts for a significant part of this consumption [1]. One problem is that the end user is not always responsible for all sources of electrical consumption and especially not for the permanent installations made by the proprietor. Another problem is related to the interest of making an energy efficient installation. In the past, the proprietor was more interested in a low initial cost, not in the electrical operating cost of the building [2]. In order to overcome this problem, energy performance certification of buildings has become mandatory (2008/2009) [1], as a result of the EU directive on the energy performance of buildings (EPBD) 2003. The energy certificate reports the energy performance of a building and indicates if the building is well adapted compared to similar building types. Furthermore, the international influence on the Swedish energy and climate policies is increasing resulting in a series of climate goals eg. decreased energy intensity with 20% during 2008-2020 and decreased greenhouse gas emission with 40% to 2020. [1]. Hence, all factors points at an increasing need for energy efficient solutions.

Studies have been made in the area of heating Ventilation and Air Condition (HVAC) applications with respect to different system concepts as well as for different electric drive technologies. Focus has been on large machines [3]. As a result, few studies have been made on small and medium sized pumps and fans [4, 5]. However, buildings contain a

large number of small and medium sized pumps and fans which altogether are responsible for a non insignificant part of the electrical consumption.

The large assortment of different drive systems on today's market results in a difficult task in making the correct decision for a given application. The differences in potential savings between different concepts have not been established and is far from common knowledge by the installer or consumer.

Another aspect worth to consider is the dimensioning of HVAC systems. In an example taken from [6], approximately 40% savings were possible for a Constant Air Volume (CAV) system delivering 20% higher flow than needed. One of the reasons for this poor efficiency is that Induction Motors (IM) have a low efficiency at light load. An interesting issue is accordingly if these "over dimensioning losses" can be reduced by using modern converter technology.

1.2 Literature overview

The energy efficiency of electric drives has been extensively studied in the literature. The IM is the most commonly used motor today and studies have been made on optimal control regarding IM efficiency [7, 8, 9]. Focus has been placed on different control methods in order to obtain optimal operation and evaluation of the resulting IM efficiency improvement. Furthermore, different loss models have been proposed [10, 11], in order to include all the loss components in the IM together with evaluation of its validity.

Efficiency improvements of frequency converters have also been the target of extensive research. Frequency converter control schemes, using different switching schemes to decrease switching losses, [12, 13, 14] are a common approach. Moreover, the development in power electronic devices has also made it possible to choose from a larger range of components. Comparative studies have been made of different devices and their counterparts [15, 16, 17]. Features such as switching transitions, thermal behavior and conduction losses are frequently analyzed in the comparisons.

Studies of permanent magnet motors have also been made to a large extent. Focus is often placed on high dynamic performance and sensorless control strategies [18]. Loss modeling has also been extensively studied where the difficulties of accurate modeling of iron losses often are stressed [19, 20, 21] comparing different iron loss modeling methods. Investigations of the so called proximity losses in the stator windings have been performed [22, 23] focusing on conductor placement and shape, as well as influence of PWM motor supply. The topic of eddy current losses in the rotor magnets has also been investigated, [24] gives a comprehensive literature review on the topic.

1.3 Purpose of the thesis and contributions

As stated above, the area of energy efficiency has been a target of research for a long time. However, there is still a lack of comparative studies of saving potential for different HVAC applications when using different drive system setups. Furthermore, development in power electronics, electrical motors, different system concepts etc introduces new areas of investigation on a daily basis. Also there is a lack of literature regarding the possible energy savings that can be made in pump and fan applications. The general objectives of this work can be summarized as follows:

- Establish suitable models for energy loss estimation in different drive systems with good enough accuracy in order to compare different motor topologies, control strategies and motor designs. The drive system as a whole will be considered in most cases, without neglecting important factors such as the influence of the frequency converter supply.
- Analyze the potential savings using improved motor and power electronic technology as well as improved control methods for different load profiles and establish guidelines for the pump/fan manufacturer, installers as well as the end user on which drive system to install for a given application and when it is economically justified to replace an existing drive system.
- Perform an investigation on which factors to consider when maximizing the efficiency of a PM motor drive, both control of a given PM motor drive but also motor design aspects coupled to pump and fan load profiles.

Due to the wide range of topics in this thesis, most contributions relates to comparative studies quantifying differences between different drive system setups but also some specific topics are considered to provide a scientific contribution. To the best knowledge of the author the contributions are summarized as follows:

- Determination of what is worth to change in a drive system for different pump/fan load profiles. For instance, when it is beneficial to replace an existing drive systems.
- Comparative studies of a wide range of drive system setups, quantifying the difference between different control strategies, motor topologies (IM, BLDC and PMSM) and motor designs with focus on energy efficiency.
- Comparative studies with resulting example quantifications on different control schemes for BLDC and PMSM with focus on energy efficiency where the drive system has been modeled as a complete unit, using FEM calculations together with circuit calculations simultaneously, in order to include the effect of the frequency converter supply on the loss components.

- Determination, based on the investigated motor sizes, of the impact on energy efficiency using different current control techniques for BLDC motors at high load, where problems with phase commutation occurs using classical BLDC control.
- Determination of the iron losses in PM motors for pump/fan applications and how the harmonic content in the inverter supply affects the iron loss component.
- Determination of energy efficiency consequences due to sizing of IM and frequency converter in pump/fan application and the impact on motor control.
- Quantification of the difference in energy efficiency between inner and outer rotor motors given the outer physical dimensions.
- Quantification of the difference in motor size and efficiency using ferrites and NdFe magnet material.
- Derivation of dynamic models for frequency converter supply, based on the line to line voltage supply, instead of phase voltages.
- Comparative studies on PMSM vs BLDC motor designs with focus on energy efficiency, using same physical size.

1.4 Outline of Thesis

Chapter 2 will describe the different types of electric drives used for HVAC applications. Furthermore, the chapter also aims to give readers, not familiar with electric drive systems, power electronics, enough insight in order to understand later chapters dealing with these concepts. Finally basic pump/fan operation and possible load profiles will be provided. Chapter 3 will present the drive system models used in this thesis. Both steady state and dynamic models will be provided with focus on energy efficiency determination. In Chapter 4 the result from the field measurements on different pump applications are presented where measurements of the electric input power has been logged for 22 months. Chapter 5 will describe different control strategies for improving the efficiency in the IM and the frequency converter. Furthermore, simulation results will be provided using the models presented in Chapter 4. Chapter 6 will present the simulation result of the analysis of a BLDC and a PMSM motor where different control strategies have been evaluated. Chapter 7 will investigate different motor design in order to improve the efficiency of the motor. In Chapter 8, the control strategies presented in Chapter 5 will be analyzed using laboratory measurements on an IM fed by a frequency converter. Chapter 9 will present the measurement made on the BLDC and PMSM's analyzed in Chapter 6 and 7. Finally Chapter 10 will analyze, the potential savings in an IM drive system for different load profiles, based on Chapter 2, 6 and 7. Furthermore, the potential savings between IM and PM motors will be investigated.

1.5 List of publications

The following publications have been made during the course of this project.

- Johan Åström and Torbjörn Thiringer, Efficiency of Induction Motor Drives for HVAC Applications - Based on a Case Study with Measurements on 3 Induction Motor Drives, 9th REHVA World congress Clima 2007 Wellbeing Indoors, Helsinki, Finland, June 2007.
- Johan Åström and Torbjörn Thiringer, Modeling and Measurements of Loss Components for Different Switching Schemes in a Three Phase Converter Using CoolMOS Transistors, The Eighth International Conference on Power Electronics and Drive Systems November 2-5, 2009, Taipei, Taiwan, conference paper - peer reviewed.
- Johan Åström and Torbjörn Thiringer, Potential Savings for Induction Motor Drive Systems for HVAC Applications, The Eighth International Conference on Power Electronics and Drive Systems November 2-5, 2009, Taipei, Taiwan, conference paper - peer reviewed.
- Johan Åström and Torbjörn Thiringer, Considerations when Modernizing Drives for Buildings Based on an Energy Efficiency and Cost Perspective, The 9th International Power and Energy Conference IPEC 2010 27-29 October, Singapore, conference paper - peer reviewed.
- Johan Åström, Investigation of Issues Related to Electrical Efficiency Improvements of Pump and Fan Drives in Buildings, Licentiate thesis, Chalmers University of Technology, Göteborg, Sweden, June, 2008

Chapter 2

Drives for pumps and fans

This chapter will describe the different types of electric drives that are used for fan and pump applications. Furthermore, it also aims to give readers not familiar with electric drive systems and power electronics, enough insight in order to understand later chapters dealing with these concepts.

The basics of the Induction motor (IM) and permanent magnet (PM) motors will be presented. Furthermore, frequency converter operation will be described.

2.1 Induction motor

The Induction motor (IM) is the most widely used electrical motor today and can be found in all sorts of applications and power levels. The main advantage compared to other motor technologies is the possibility to connect the IM directly to the grid, without any additional power electronics. Furthermore, by using a frequency converter it is easy to control the speed in an open loop manner provided that the dynamic performance is of less importance.

Induction motors sold in EU has previously been classified by an efficiency label eff1-eff3 where eff1 is the most energy efficient. This classification was introduced 1998 by the EU and CEMEP (the European Committee of Manufacturers of electrical Machines and Power electronics). The motors included in this classification are two and four pole IM in the range 1.1kW-90kW representing 75-80% of the European market [25].

The goal of CEMEP was to decrease the number of eff3 motor sales by 50% between 1998-2003. CEMEP had 36 members during this period, (eg ABB Siemens) which together sold 20 million units in Europe. The result was that, the eff2 label took most of the market share (86%, and eff1 8%). This can be explained by the increased cost of an eff1 motor, (20% higher compared to eff2), and that 80-90% are sold to OEM companies (original equipment manufacturer) [25]. Hence, eff labeled motors are still used to a large extent in today's installations and will be the focus in later chapters.

The International Electrotechnical Commission (IEC) has introduced a new efficiency classification, IEC 60034-30, replacing the eff1, eff2 and eff3 labels [26]. The motors included are single speed squirrel cage IM motors in the power range 0.75-375kW. The classification consists of four labels, IE1 (comparable to eff2), IE2 (comparable to eff1) IE3 and IE4, where IE4 is the most energy efficient label. It should be noted that IE4 are not yet commercially available (2008) [26], the goal is to reduce the losses with an additional 15% compared to IE3. Furthermore, IE3 is only available for ratings above 11kW but will be introduced during 2011 for smaller ratings according to one of the largest manufacturer.

The efficiency limits for 4-pole IM in the range 1.1-30kW can be seen in Table 2.1. The values are given for 75% of the rated load operation at rated voltage/frequency, (V/Hz).

Table 2.1 Efficiency limits for 4-pole IM at 75% of rated operation

kW	Efficiency, Eff3	Efficiency, eff2/IE1	Efficiency, eff1/IE2	Efficiency, IE3
1.1	<76.2	≥76.2, <83.8	≥ 83.8	≥84.1
1.5	<78.5	≥78.5, <85.0	≥ 85.0	≥ 85.3
2.2	<81.0	≥81.0, <86.4	≥ 86.4	≥ 86.7
3	<82.6	≥82.6, <87.4	≥ 87.4	≥ 87.7
4	<84.2	≥84.2, <88.3	≥ 88.3	≥ 88.6
5.5	<85.7	≥85.7, <89.2	≥ 89.2	≥ 89.6
7.5	<87.0	≥87.0, <90.1	≥ 90.1	≥ 90.4
11	<88.4	≥88.4, <91.0	≥ 91.0	≥ 91.4
15	<89.4	≥89.4, <91.8	≥ 91.8	≥ 92.1
18.5	<90	≥90.0, <92.2	≥ 92.2	≥ 92.6
22	<90.5	≥90.5, <92.6	≥ 92.6	≥ 93.0
30	<91.4	≥91.4, <93.2	≥ 93.2	≥ 93.6

2.1.1 IM operation

The IM consists of a stator, (stationary part) and a rotor, (rotating part). The stator and rotor can be regarded as electromagnets consisting of a number of pole pairs. The stator consists of an iron core in order to conduct the magnetic flux, and of copper windings, distributed in order to create a sinusoidal magnetic flux wave when the motor is connected to a sinusoidal voltage. When a current is flowing in a winding, a magnetic flux is produced around the winding. If the IM has a balanced three phase winding, the net flux becomes constant in magnitude and will rotate at the same speed as the voltage frequency, ω_s (rad/s).

Assume now that the rotor is at stand still and a sinusoidal voltage is applied to the stator. A stator magnetic flux will now be created in the IM, crossing the air gap to the

rotor. The rotating magnetic flux induces a rotor voltage perpendicular to the direction of the flux. As a result, a current is starting to flow in the rotor creating a force, acting on the rotor. The rotor will accelerate according to

$$J \frac{d\omega_r}{dt} = T_e - T_L \quad (2.1)$$

where J is the moment of inertia, ω_r is the rotor speed and T_e and T_L is the electromagnetic and load torque respectively.

A torque is produced as long as the stator flux is rotating relative to the rotor. Hence, when no load is applied to the IM the speed will increase until $\omega_r = \omega_s$.

When the IM is loaded, ω_r decreases slightly in order for the IM to create the electromagnetic torque needed for the applied load. The difference in speed is called the slip speed which at rated operation is in the range of 1-5% of ω_s depending on motor size, for motor ratings approximately above 200kW the slip is $<1\%$.

Figure 2.1a shows the torque speed diagram for an IM together with a load characteristic. The operating point will be in the intersection of the two curves. In order to change the speed the load curve or the IM curve has to change.

Figure 2.1b shows the torque speed diagram, for three fixed setup of voltages and frequencies. An important relationship regarding the operation of an IM is the ratio of the voltage and frequency (V/Hz) which is proportional to the flux produced in the motor. Furthermore, the maximum torque is proportional to the flux for a given rated current. As a result, by keeping the V/Hz constant, the rated torque will be produced by the same current magnitude which results in a constant rated torque as can be seen for the first two T- ω curves in figure 2.1b. However, when the frequency is increased above a certain limit, in this case the synchronous speed ω_{s2} , the voltage will be constant due to the limitations of the frequency converter, and also due to the voltage rating of the IM. The motor is now running in its so called field weakening region which results in a lower rated torque, (operation in the field weakening region is more common in automotive applications).

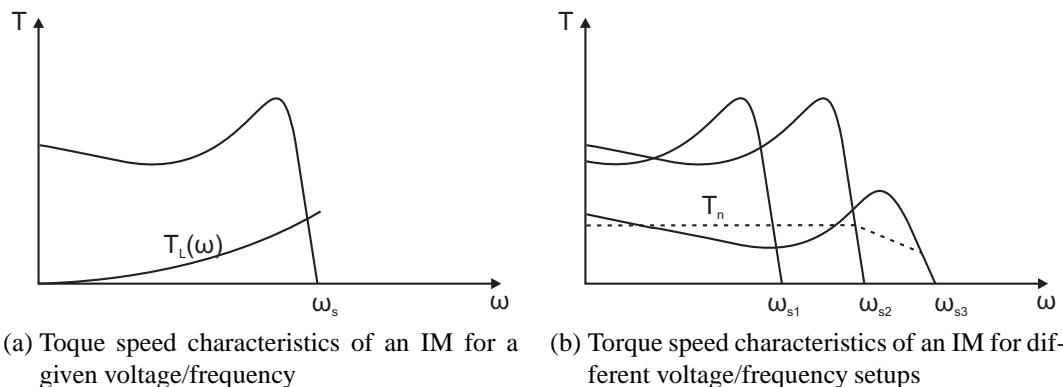


Fig. 2.1 Torque speed diagram of an IM.

2.1.2 Loss components

The efficiency of an IM is relatively high when running at its optimal operating point, which usually is located around 75% of its rated load, but can decrease substantially from its optimum at light load. This gives an opportunity to optimize the control of the IM in order to minimize the losses at each operating point which will be discussed more in detail in Chapter 5.

The different losses that occur in an IM are the following:

- Resistive losses
- Core losses
- Mechanical losses
- Harmonic losses
- Stray losses

The stator and rotor losses are represented by the resistive losses in the stator and the rotor windings. These losses constitute 55-60% of the total losses, according to [27] (not including the losses due to harmonics).

The mechanical losses produced in the IM are friction losses in the bearings and losses caused by the cooling fan, (if a fan cools down the motor); these losses contribute with 5-10% of the total losses [27].

Furthermore, the hysteresis and eddy currents in the core of the stator and the rotor cause core losses. This loss component contributes to approximately 20-25% of the total losses [27].

The harmonic losses are produced from the harmonics in the supply voltage and currents, which do not contribute to the mechanical output power. The amount of harmonics depends on the the frequency converter supply but can constitute 10-15% of the total losses [27].

Finally, the stray losses are the losses that are not accounted for by the other losses discussed above. These losses constitute 10-15% of the total losses [27].

These values are naturally dependent on load, motor size, motor design etc and are only given to quantify the possible difference between the different loss components for a grid connected IM operated at rated load.

2.2 Permanent magnet motors

Permanent magnet motors have become more popular recent years due to cost reduction in PM material and its high efficiency also at low load, high power density and high dynamic performance.

All PM motors fall under the category of synchronous motors. Usually power electronics is needed in order to operate the PM motor, accordingly a converter is needed to operate the motor.

This thesis will focus on a type of PM motor often referred to as Brush Less DC motors (BLDC), in addition it will also investigate the the differences regarding sinusoidally commutated PM motors, using surface mounted permanent magnets, here after referred to as PMSM. The focus here has been placed on the BLDC type due to its advantage in design and manufacturing, resulting in lower cost, as well as in control simplicity compared to a PMSM. It should be noted that the BLDC has a reduced dynamic performance compared to the PMSM. However, high dynamic performance is not needed in HVAC applications. Moreover, improvements in power electronics have made the BLDC an interesting competitor to the PMSM. As a result, the trends point to a wider use of BLDC motors compared to PMSM motors for loads with low dynamic performance such as pump and fans, [28, 29, 30].

2.2.1 Brush Less DC motors and PMSM

BLDC motors, also referred to as EC and BLCM in the literature, differs from PMSM in its construction and the commutation of the currents. A BLDC motor is designed in order to create a trapezoidally induced voltage in the stator windings, called back emf which can be seen in figure 2.2, whereas a PMSM is designed to get a sinusoidal induced voltage.

The electromechanical torque T_e produced by the motor can be expressed as

$$T_e = \frac{e_a i_a + e_b i_b + e_c i_c}{\omega_r} \quad (2.2)$$

where ω_r is the mechanical rotor speed. It is evident, from (2.2), that it is desirable to keep the phase currents constant when the back emf is kept constant in order to have a constant torque.

Hence the phases should ideally be excited according to figure 2.2b, resulting in a constant torque. However, due to the inductance in the motor, the phase currents will not decrease to zero or increase to its desired value at the same time instant as the phase voltage is turned off or on. This will result in a ripple in the torque which is one of the problems related to BLDC motors. This will be investigated in more detail in later chapters. Furthermore, the induced voltage will of course never have the ideal waveform shown in figure 2.2b. Figure 2.3a shows a more realistic emf waveform for a BLDC motor.

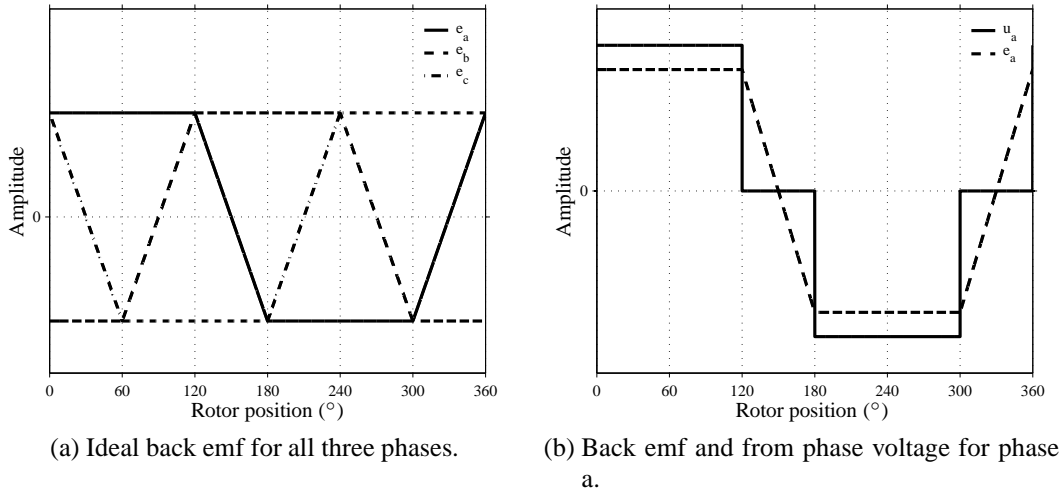


Fig. 2.2 Ideal emf and voltage for a BLDC motor.

Since the induced voltage is no longer constant during 120° as in the ideal case, the desired current wave form also changes. In fact, it can be shown that the harmonic content in the current ideally should be equal to the harmonic content in the induced voltage, and even have the same amplitude ratio, meaning that the current wave form should be identical to the emf as can be seen in figure 2.3b. The derivation can be found in Appendix A. However, the classical BLDC current control assumes an ideal emf waveform resulting in a reference current that is constant during its on state and zero for two 60° interval per period.

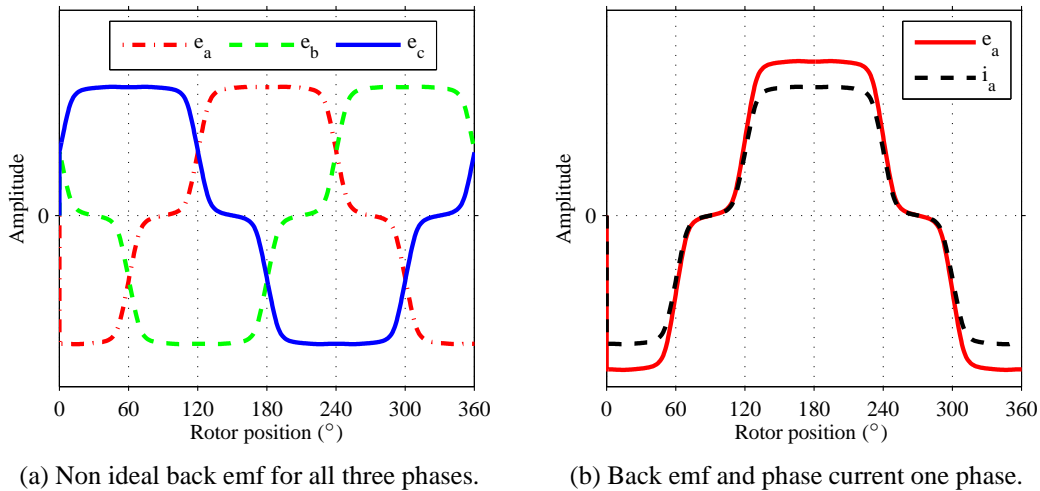


Fig. 2.3 Induced voltage in the stator windings for a non ideal BLDC motor and suggested current waveform.

Figure 2.4 shows an equivalent per-phase circuit of the BLDC motor at steady state operation, (constant applied voltage, constant back emf and constant current). The steady state expression of the stator voltage can be expressed as, (ideally $di/dt=0$ at steady state)

$$V_a = I_a R_s + E_a = I_a R_s + k_e \omega_r \quad (2.3)$$

Since the commutation of the motor only depends on the rotor position it is not possible to increase the speed using faster commutation, instead the stator voltage magnitude needs to be changed. As a result, the rotor speed is proportional to the magnitude of the stator voltage. Furthermore, due to limitations in the voltage magnitude from the supply and allowed maximum current and voltage of the motor, the operating range can be described by figure 2.5. The maximum torque is decreasing with increasing speed since the emf comes closer to the maximum voltage, dc link voltage, which makes it impossible to maintain the current at the desired level.

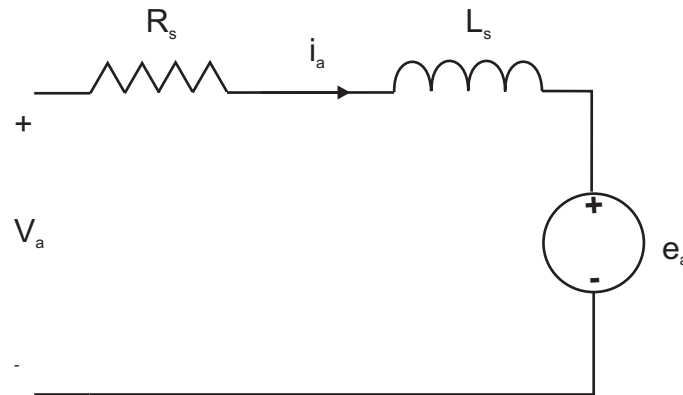


Fig. 2.4 Equivalent circuit of a BLDC.

For a PMSM motor the the excitation of the windings should be sinusoidal and in phase with the induced voltage in order to keep the torque constant and to have a high torque/ampere ratio. Hence, the position of the rotor needs to be known at all time which makes the control more complex.

2.2.2 Loss components

Since the rotor of a BLDC/PMSM motor consist of permanent magnets, creating the rotor flux, the rotor current will be negligible. As a result, the rotor losses are assumed to be zero. The remaining losses are same as for the IM but different in magnitude. The power factor (PF) of a permanent magnet motor is higher than that of an IM of similar rating since less magnetizing current, (less reactive power), is needed for magnetization. Hence, for a given output power, increased PF results in decreased current amplitude which in turn gives lower resistive losses in the motor.

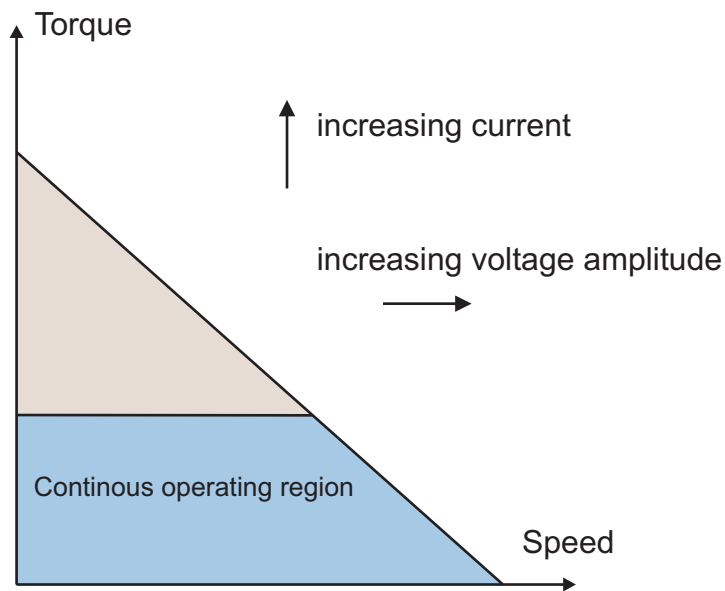


Fig. 2.5 Torque speed diagram of a BLDC motor.

The efficiency of PMSM/BLDC motors are more constant as a function of load compared to the IM where the efficiency drops quite rapidly with decreasing load as explained in Section 2.1. This can also be explained by the PF since the reactive current component in an IM is much larger and more or less constant, while the active current component is decreasing. As a result, the relative losses will increase with decreasing load (decreasing active current).

It is difficult to draw any immediate conclusions between the difference in efficiency between a PMSM and a BLDC motor and this issue will be analyzed in more detail in later chapters. Studies have been made in order to determine the difference, [31], but it was not possible to make a general efficiency distinction between the two motor types.

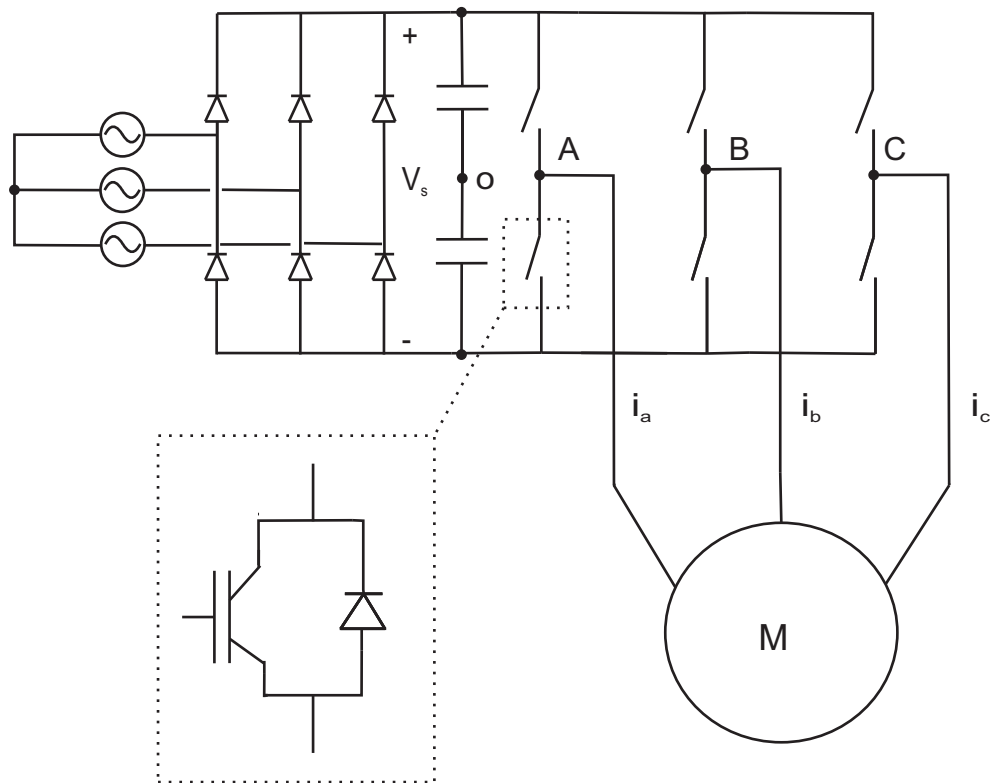


Fig. 2.6 Three phase frequency converter with a motor load.

2.3 Frequency converters

In order to best change the speed of an IM and to operate a PM motor, a frequency converter is needed. Figure 2.6 shows a schematic diagram of a three phase frequency converter. The rectifier stage, which in this case consists of diodes, rectifies the grid voltage, v_r , v_s , v_t . In order to create a stable DC voltage after the rectifier, a capacitor is connected in parallel. This part is called the DC link of the converter. The inverter, consisting of transistors can now be controlled in order to provide the motor with an arbitrary voltage and frequency.

By turning the transistors in each inverter leg on and off quickly, (several kHz), changing the output, (point A, B and C in the figure), from $\pm V_{dc}$, and by controlling the width of each pulse, a variable-frequency, voltage can be created. This technique is called Pulse Width Modulation (PWM). Figure 2.7 shows one leg of the frequency converter and the pulse pattern during one half of the fundamental period. It should be pointed out that in the figure the switching frequency is fairly low in relation to the fundamental wave in order to illustrate the operation. During the time interval t_0-t_1 , T_2 is on and the negative DC bus voltage is applied to the load. The current will flow through either D_2 or T_2 , depending on the direction of the current i_a , shown in figure 2.8. If i_a is negative the current goes through the transistor otherwise through the freewheeling diode. At the time instant

t_2 , T_2 turns off and T_1 turns on. The direction of i_a determines which component of T_1 and D_1 that will start to conduct. T_1 is now on during the time interval t_1-t_2 . The resultant sinusoidal voltage can be seen in figure 2.7. The time duration of each pulse is determined by the reference voltage and it can be noted that the positive pulse width increases as the amplitude of the voltage increases.

The different loss components present in the converter are conductive losses and switching losses. The switching losses occur in two of the four components at each switching instant depending on the direction of the load current. Four cases are possible, also shown in figure 2.8:

T2 turns on (T1 turns off)

i_a is positive, results in turn off losses in T1 and turn on losses D2, (case 1).

i_a is negative, results in turn off losses in D1 and turn on losses T2, (case 2)

T1 turns on (T2 turns off)

i_a is positive, results in turn off in D2 and turn on losses T1 (case 3)

i_a negative, results in turn off losses in T2 and turn on losses in D1 (case 4)

One special case occurs when i_a is zero, which results in zero switching losses. The switching losses can now be estimated using the switching characteristics presented in Section 2.3.2.

Details regarding the control of the frequency converter is described in Chapter 5.

The following subsections will describe the different loss components present in a frequency converter. The basic operation and physical structure of the most commonly used semiconductors in frequency converters are also provided in order to understand the different losses.

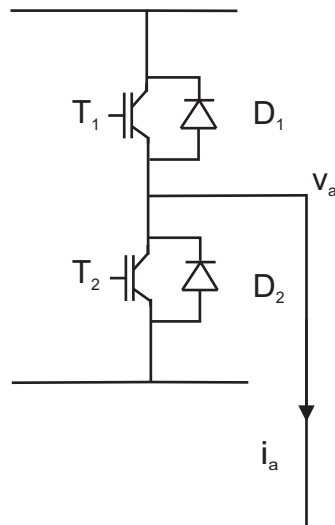
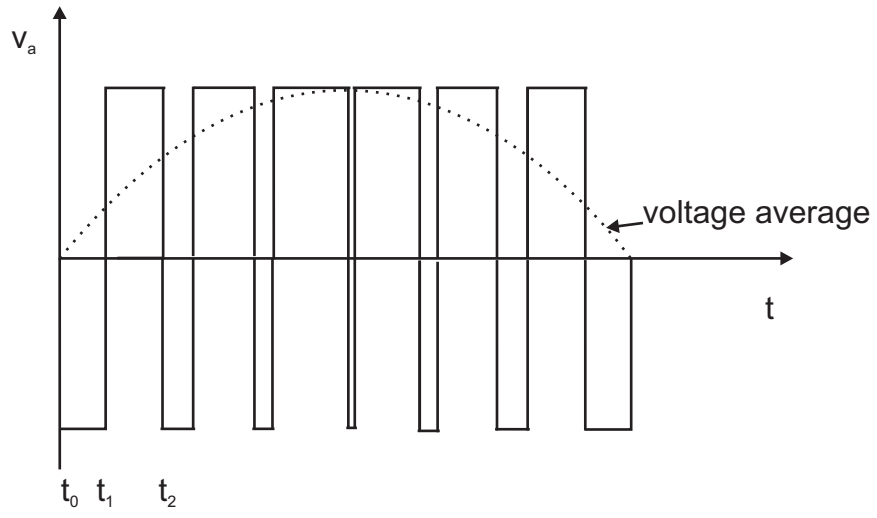


Fig. 2.7 Pulse pattern of one phase during half of the fundamental period.

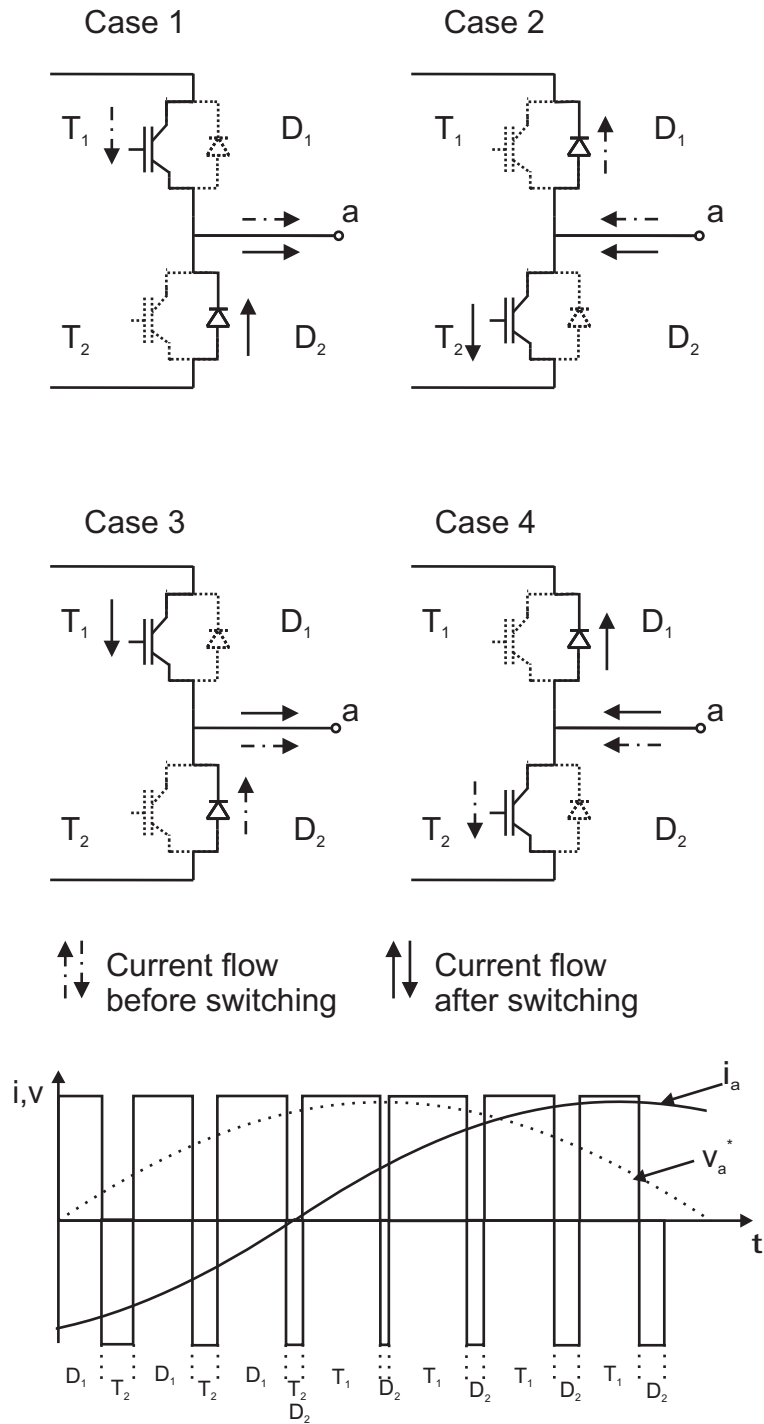


Fig. 2.8 Four cases of switching transitions.

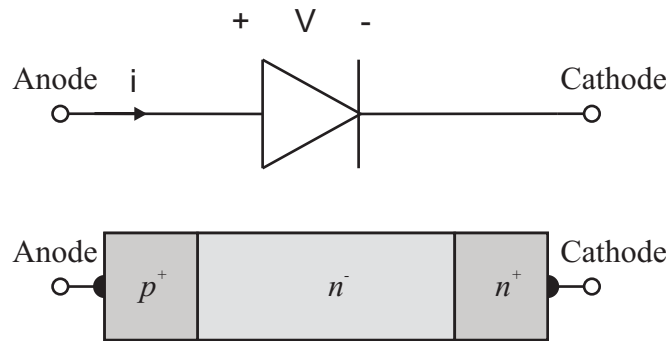


Fig. 2.9 Circuit symbol and the physical structure of a power diode.

2.3.1 Power Diodes

Power diodes have different physical structure and operational characteristics compared to low power diodes. However, the basic operating principle are the same, namely that the diode blocks the current when a reverse voltage is applied across the diode and conducting when the voltage over the diode is positive. Figure 2.9 shows the circuit symbol and the physical structure of the device. The difference compared to a low power diode is the n^- layer which is a region consisting of a lightly n-doped silicon material. The thickness of the n^- region decides how large reverse voltage the diode can withstand before it reaches its breakdown voltage. When the diode is conducting the voltage drop is approximately $V + R_{on}I$, where V is in the range of 0.8-1V and $R_{on}I$ is in the range of 1V at rated current.

The magnitude of the voltage drop also depends on the dimensions of the diode. If the reverse blocking capability is increased, an increased length of the n^- layer will result, and the on-state voltage drop will increase. The losses in the diode comes mainly from conductive losses but also in some extent from switching losses.

Schottky Diodes

A Schottky diode is a metal semiconductor junction consisting of a thin film of metal in contact with a semiconductor, usually Si. The advantage compared to a pn junction diode is the decreased voltage drop at on-state and the decrease of the recovery transitions, resulting in lower power dissipation and in addition also decreases the emitted electromagnetic interference (EMI). However, the reverse blocking capability is limited to a maximum of 250V for Si based Schottky diodes, [32], which makes it unsuitable for use in frequency converters. In order to increase the reverse blocking capability SiC can be used instead. However, SiC schottky diodes have a high on-state voltage drop. The interested reader can find more detailed information in [33] and [32].

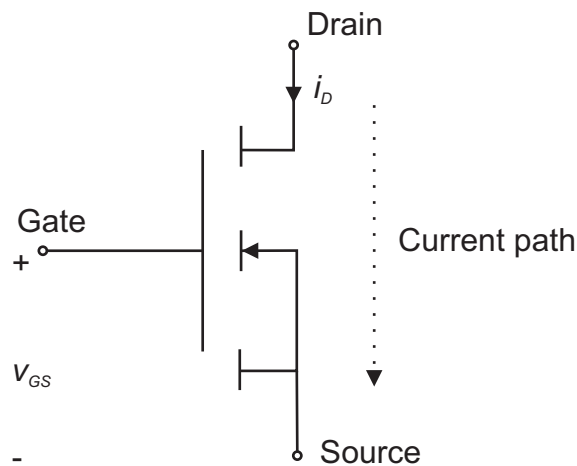


Fig. 2.10 Circuit symbol for an n-channel MOSFET.

2.3.2 MOSFETs

Power MOSFET transistors are today used for blocking voltages up to a DC-level of 300V [34]. The advantages of the MOSFET compared to its counterparts are high switching speed and low gate drive power consumption. The current through the MOSFET is controlled by the gate voltage. Figure 2.10 shows the circuit symbol where v_{GS} and i_D denotes the gate-source voltage and the drain current respectively.

Figure 2.11 shows the physical structure of a n-channel MOSFET cell. Usually many cells are packed together in parallel in order to increase the current capability. The drain and source consists of an aluminium metallization grown on the drain n-region and across the pn material at the source. Between the two source terminals an isolated dielectric material is grown, isolating the gate from the source. When a positive gate voltage is applied, with respect to the source, an n-channel is formed between the drain and source, due to an accumulation of electrons, and the MOSFET is turned on. The thickness of the n-channel depends on the magnitude of the gate voltage. So, in principle, the MOSFET operates as a valve, where the Gate voltage determines how "open" the valve is.

Figure 2.12 shows different operating states of a MOSFET for different v_{GS} where $v_{GS4} > v_{GS3} > v_{GS2} > v_{GS1}$. When the MOSFET is in its on-state it is operated in the ohmic region. It can be noted that, as v_{GS} is increased i_D increases, for a constant v_{DS} . Hence, by increasing the gate voltage the on-state voltage drop decreases for a constant current.

The idealized switching characteristics of one leg in a frequency converter, described in figure 2.13, using a MOSFET can be seen in figure 2.14, where the effects of parasitic inductance and reverse recovery are ignored. The load current is assumed to be of constant magnitude, I_{load} during this very short time period, less than $1\mu s$. Hence, the load current is freewheeling through the diode prior to the MOSFET turn on. At turn on, a positive gate-source voltage is applied and at time t_0 the gate voltage has reached the threshold voltage V_{th} which is the voltage level when the current starts to rise. The voltage across the

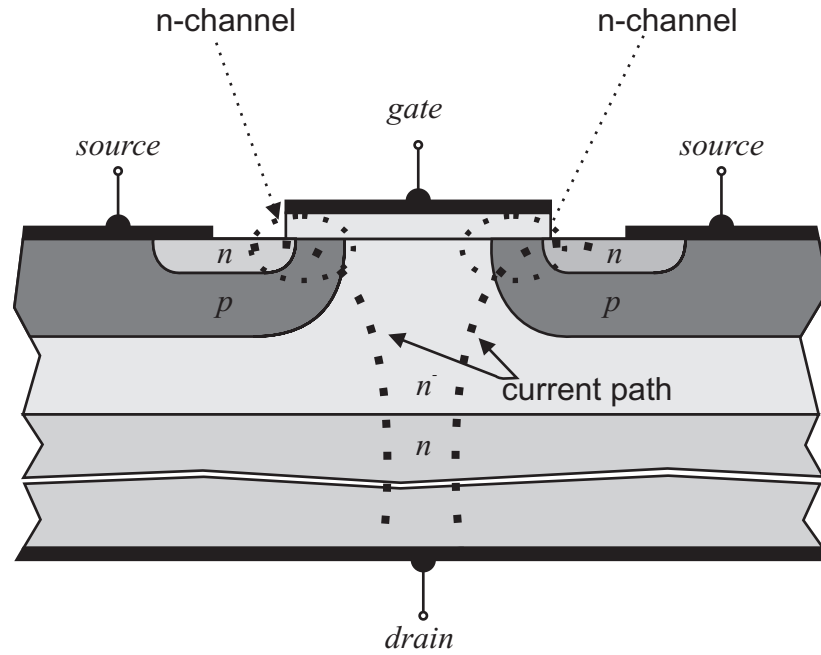


Fig. 2.11 Physical structure of cell in a power MOSFET.

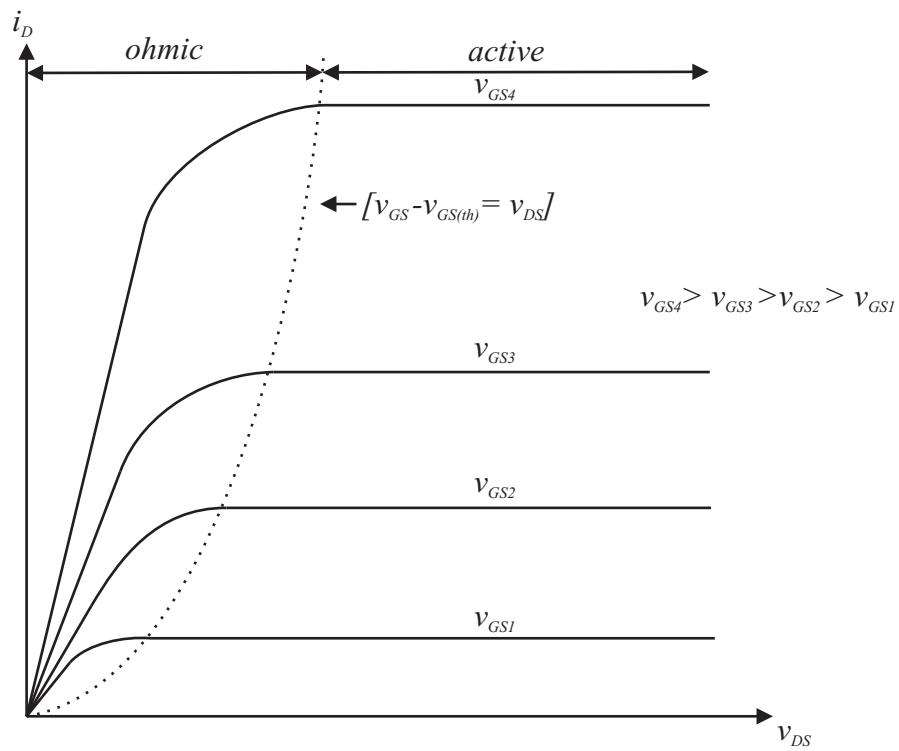


Fig. 2.12 I-V characteristics of an n-channel MOSFET for different v_{GS} .

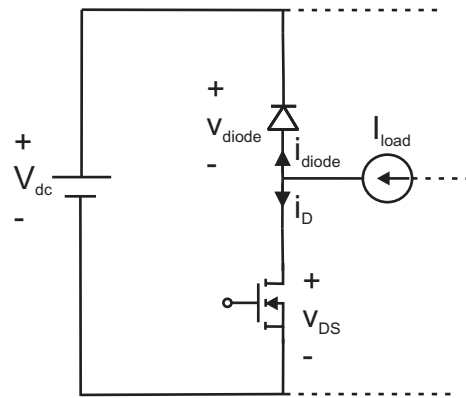


Fig. 2.13 Circuit diagram of the active components in one leg in a converter, valid for negative load current.

MOSFET will remain at its high value as long as the freewheeling diode is conducting. When the current in the MOSFET has reached I_{load} and accordingly the diode current comes to zero, the diode turns off and the voltage starts to increase over the diode and decrease across the MOSFET. At turn off of the MOSFET, the gate voltage applied to the gate is reduced to zero. The following time intervals shows the reverse characteristics as was described at turn on. There are some more important non-ideal characteristics for this switch procedure, and the interested reader can find more details in [33]. Details regarding how the stray inductance in the circuit gives over-voltage and how the discharge of the n-region results in recovery of the components is described in detail.

One important thing to point out is that in the reverse direction, the power MOSFET act as a diode, observe the p-n from drain to source in figure 2.11. In the type of MOSFET transistor used in this work, CoolMOS, it is important to avoid that this diode turns on, which gives a circuit complication, as shown later.

2.3.3 IGBTs

An Insulated Gate Bipolar Transistor (IGBT) is the most commonly used transistor for high voltage applications from 400VAC and upwards. The physical structure of an n-channel IGBT is shown in figure 2.15. There are also different types of IGBTs having slightly different characteristics. By adding a n^+ layer between the p and n^- layer, often referred to as a non-punch-through IGBT, the switching speed can be increased. However, the on-state voltage drop will increase, the interested reader can find a detailed description of different IGBTs in [35].

The drawback of the IGBT compared to the MOSFET is the switching speed which is lower for the IGBT.

The hard switched voltage and current waveforms for the IGBT are similar to those of the MOSFET. The main difference is that the current trough the IGBT at turn off decreases

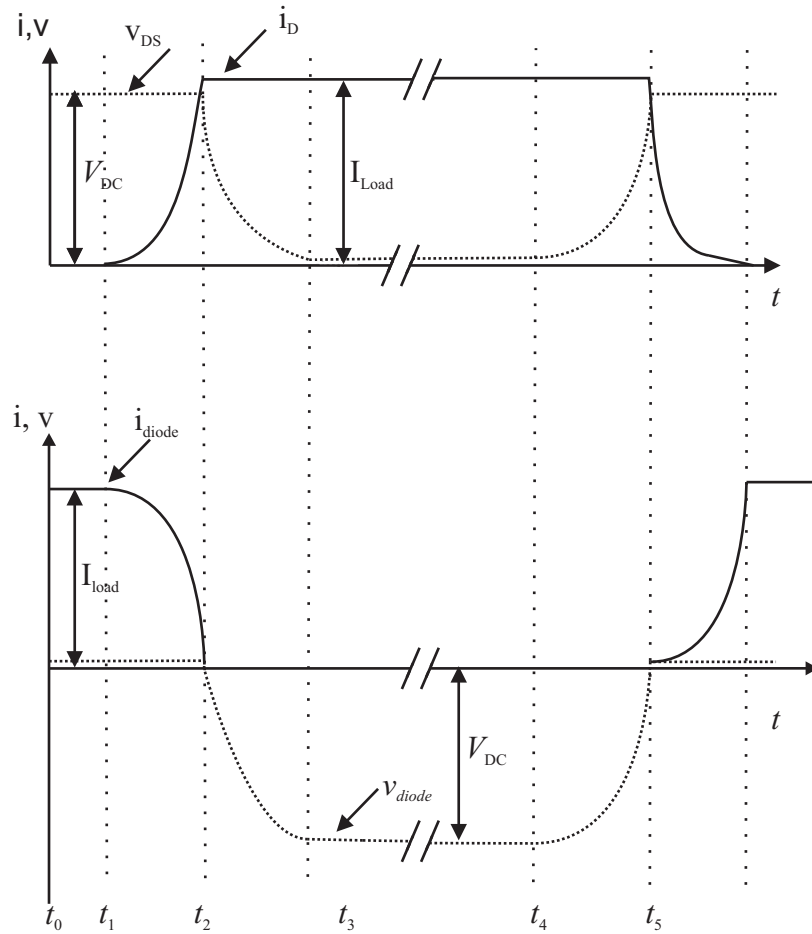


Fig. 2.14 Turn on and off characteristics of the MOSFET and diode with an inductive load.

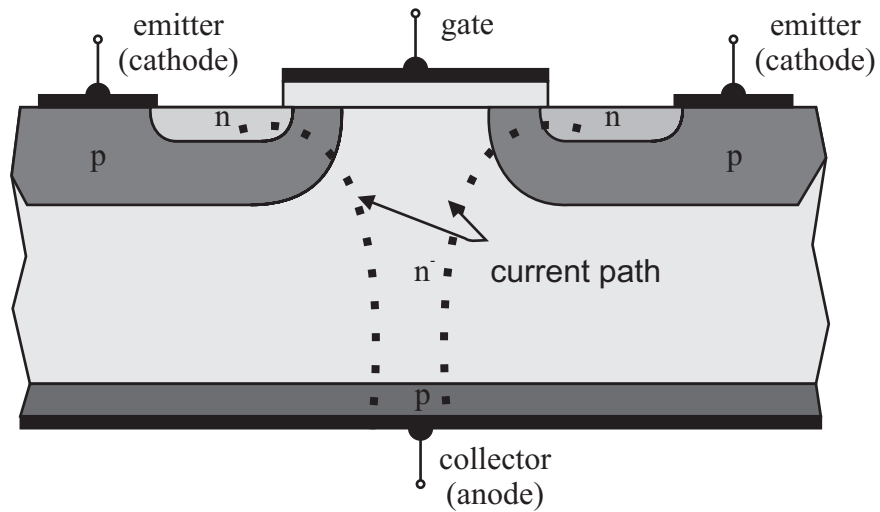


Fig. 2.15 Physical structure of an IGBT.

slowly at the end of the transition. This is often referred to as current tailing which makes the IGBT slower than the MOSFET.

2.4 Pumps and fans as loads

This section will describe the load characteristics of pumps and fans. The operating characteristics of a pump and fan can be described by a Head-Flow, (H-Q), diagram seen in figure 2.16, [36]. The shape of the curve varies between different types of fans and pumps but are of minor importance for this illustration. Each curve in the diagram corresponds to a constant pump/fan speed and the steady state operating point will be defined at the intersection between the system curve and the pump/fan curve. The system curve represents the pressure drop in the system as a function of flow, where pressure drops arise from friction in pipes valves etc. In order to change the operating point, either the speed or the system characteristics needs to be changed. Figure 2.17 shows how a reduction of 50% in the flow, from Q_1 (point A) to Q_2 , (B or B'), can be achieved. When the pump/fan speed is constant at n_1 the system characteristic needs to be changed in order to reduce the flow, eg using a valve, and the new operating point becomes B', (H_3, Q_2). If the system is kept unchanged and the the speed of the pump/fan is varied instead, the resulting operation point becomes B, (H_2, Q_2). It is evident that the power demand is much higher when the speed is kept constant. The affinity laws describes the relation between speed, head and flow and can be expressed as [36],

$$\frac{Q_1}{Q_2} = \frac{n_1}{n_2} \quad (2.4)$$

$$\frac{H_1}{H_2} = \frac{n_1^2}{n_2^2}. \quad (2.5)$$

As a result, the difference in power between two operating points can be expressed as

$$\frac{P_1}{P_2} = \frac{Q_1 H_1}{Q_2 H_2} = \frac{n_1^3}{n_2^3}. \quad (2.6)$$

Hence, by reducing the speed by 50%, the power is theoretically reduced by 87.5% provided that the system curve is proportional to Q^2 which is the most common made assumption in the literature. The power difference between B' and B depends on the characteristics of the pump/fan, however the difference is always substantial.

2.5 Load profiles

This section will describe two basic load profiles obtained from the literature and two fictive profiles. The load demand refers to the demanded flow from a pump or fan. The torque demand can then be calculated using the affinity laws presented in Section 2.4 assuming that the efficiency of the pump and fan is constant. The load profiles presented in this section will be used for the saving potential analysis in Chapter 10. It should be

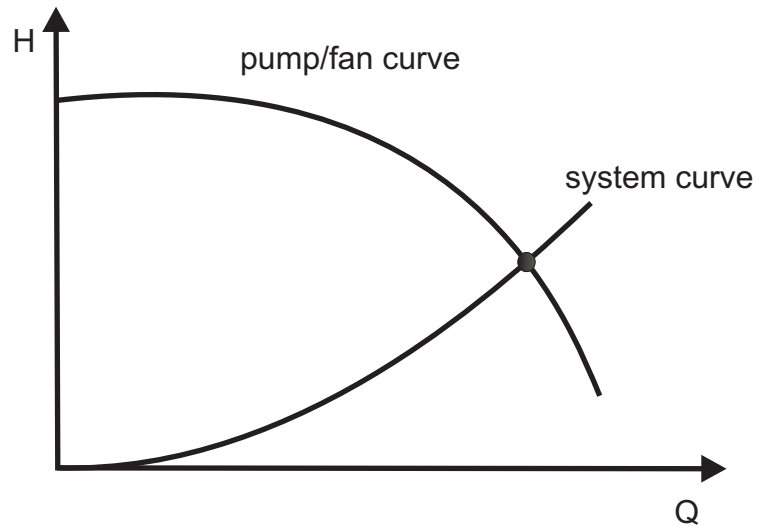


Fig. 2.16 Pump/fan characteristic for a given speed together with a system curve

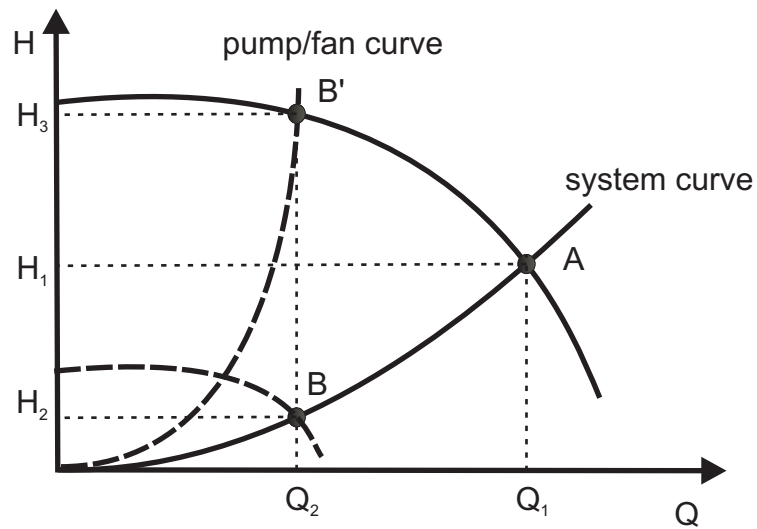


Fig. 2.17 Pump/fan characteristics for two different speeds together with two different system curves

noted that the profiles only show how a certain load can operate and that deviations can, and will, occur from case to case.

2.5.1 Load profile A

Load profile A describes a two level load operating at 100% for two thirds of the time and at 50% for one third of the time. This profile is can be found for Constant Air Volume system (CAV) using part time reduced flow [38]. Figure 2.19 shows the load demand and its annual distribution.

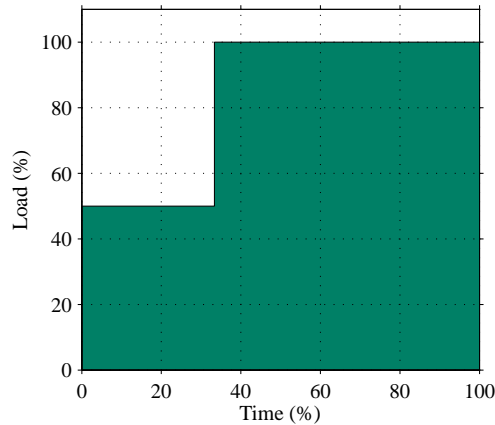


Fig. 2.18 Load profile representing a 100% load demand for 2/3 of the time and 50% 1/3 of the time (A).

2.5.2 Load profile B

Load profile B is taken from [39] and refers to a typical load profile for a Variable Air Volume system. Figure 2.18 shows the annual load demand.

2.5.3 Fictive load profiles

Figures 2.20a and 2.20b shows load profiles C and D respectively. Profile C describes a load with 30% load demand for 80% of the time and 100% for 20% of the time. Load profile D describes a constant load demand.

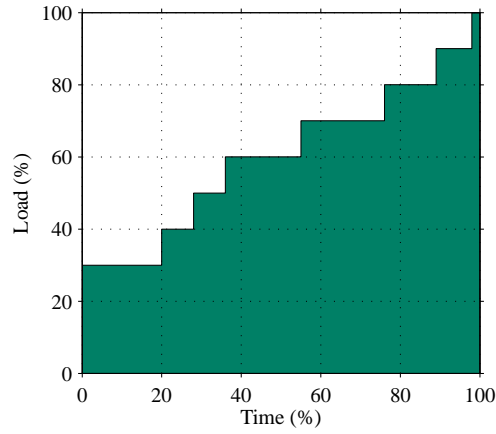
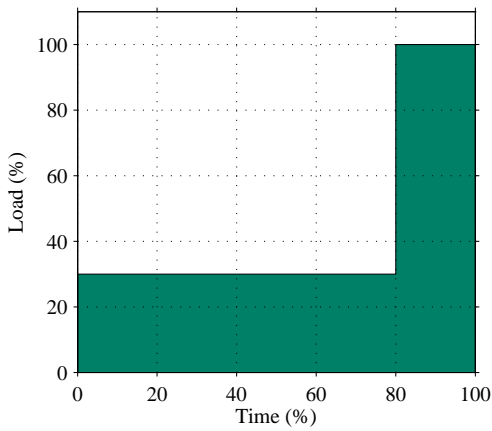
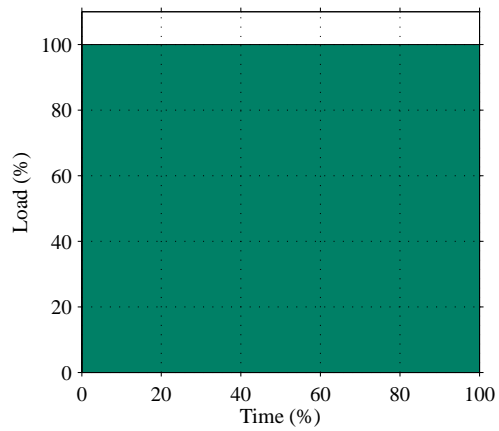


Fig. 2.19 Load profile representing a load profile for a VAV system (B).



(a) Load profile with a low load demand during 80% of the time and 100% load demand 20% of the time (C).



(b) Load profile with constant power demand (D).

Fig. 2.20 Fictive load profiles

Chapter 3

Modeling of electrical drive systems

There are many different types of motor models presented in the literature. This chapter will present the models used in this work and motivate why these have been chosen. The overall goal is to model the losses in a drive system as accurate as possible. Due to the relative complex nature of the losses in drive systems, it is not possible to account for all factors. However, it will be possible to identify trends between different control schemes and motor designs. Both dynamic modeling and stationary modeling are used.

3.1 Induction motor

3.1.1 Dynamic modeling suitable for converter supply

Dynamic models are for apparent reasons more complex than stationary models. Furthermore, the efficiency at stationary conditions are of interest since HVAC applications are assumed to operate at constant load demand for time durations that are much longer than the transient transitions. However, in order to estimate the converter loss components, the motor current at each switching instant needs to be known. Hence, a dynamic model is more convenient which makes it easy to determine the instantaneous current magnitude at each switching instant.

A dynamic Matlab Simulink [®] model of the IM, used for the purpose of estimating the switching losses in a frequency converter and compare different switching schemes will be considered, derived for the line to line voltage. The IM model will be made as simple as possible, not containing iron losses nor stray or mechanical losses.

The derivation of the IM equations are well documented in the literature [40] and will therefore only be described briefly. It is assumed that the IM has a balanced three phase winding. The stator and rotor voltages can be expressed as

$$\mathbf{v}_{abc}^s = R_s \mathbf{i}_{abc}^s + \frac{d}{dt} \Psi_{abc}^s, \quad (3.1)$$

$$\mathbf{v}_{abc}^s = R_r \mathbf{i}_{abc}^s + \frac{d}{dt} \Psi_{abc}^s \quad (3.2)$$

where the stator and rotor voltages are denoted by \mathbf{v}_{abc}^s , \mathbf{v}_{abc}^r and the stator and rotor fluxes Ψ_{abc}^s and Ψ_{abc}^r respectively. The superscript *s* refers to the reference frame which in this case is the stationary reference frame.

The flux is defined as

$$\Psi = L\mathbf{i} \quad (3.3)$$

which gives the following expression for the derivative of the flux

$$\frac{d}{dt} \Psi = \frac{d}{dt} (L\mathbf{i}) = \left(\frac{d}{dt} L\right)\mathbf{i} + L\left(\frac{d}{dt} \mathbf{i}\right). \quad (3.4)$$

Since the inductance in the IM is a function of the rotor position it is more convenient to express the derivative as

$$\frac{d}{dt} L = \frac{d\Theta}{dt} \frac{dL}{d\Theta} = \left(\frac{dL}{d\Theta}\right)\omega_r. \quad (3.5)$$

where Θ is the electrical rotor position and ω_r is the electrical rotor speed. The equations can now be written on the following general form

$$\mathbf{V} = \mathbf{R}\mathbf{i} + \frac{d}{dt} L\mathbf{i} + L\frac{d\mathbf{i}}{dt} = \left(\mathbf{R} + \frac{d}{dt} L\right)\mathbf{i} + L\frac{d\mathbf{i}}{dt} \quad (3.6)$$

The next step is to express the inductance in the motor. All windings are coupled to each other where M_{xy} defines the mutual inductance in phase *x* caused by the current in phase *y*. Since the IM is symmetrical it is assumed that the expression for the inductance in each phase are equal. The mutual inductances between two stator windings, displaced 120°, can be expressed as

$$M_{xy(s)} = M_s \cos(\Theta) = M_s \cos(2\pi/3) = -0.5M_s \quad (3.7)$$

where M_s is the mutual stator inductance. It should be noted that the magnetizing inductance, L_m , in the equivalent circuit of the IM is not the same as M_s . The relation between the two quantities are

$$M_s = \frac{3}{2}L_m. \quad (3.8)$$

This term is a result from the derivation of the equivalent circuit, for details refer to [40].

The inductance matrix for the stator can now be expressed as

$$\mathbf{L}_{ss} = \begin{pmatrix} M_s + L_{s\sigma} & -0.5M_s & -0.5M_s \\ -0.5M_s & M_s + L_{s\sigma} & -0.5M_s \\ -0.5M_s & -0.5M_s & M_s + L_{s\sigma} \end{pmatrix}. \quad (3.9)$$

The leakage inductance for each phase does not contribute to the coupling.

The coupling between the stator and rotor windings are a bit more complex since the mutual inductance depends on the rotor position. The mutual inductance matrix, \mathbf{L}_{sr} , can be expressed as

$$\mathbf{L}_{sr} = \begin{pmatrix} M_{sr}\cos(\Theta) & M_{sr}\cos(\Theta + \frac{2\pi}{3}) & M_{sr}\cos(\Theta + \frac{4\pi}{3}) \\ M_{sr}\cos(\Theta + \frac{4\pi}{3}) & M_{sr}\cos(\Theta) & M_{sr}\cos(\Theta + \frac{2\pi}{3}) \\ M_{sr}\cos(\Theta + \frac{2\pi}{3}) & M_{sr}\cos(\Theta + \frac{4\pi}{3}) & M_{sr}\cos(\Theta) \end{pmatrix}. \quad (3.10)$$

Since the parameters are determined assuming equal numbers of turns in the stator and rotor,

$$M_s = M_r = M_{sr} = M_{rs}. \quad (3.11)$$

Continuing with the rotor equations, using the similar reasoning as for the stator, the inductance matrixes can be expressed as

$$\mathbf{L}_{rs} = \begin{pmatrix} M_{rs}\cos(\Theta) & M_{rs}\cos(\Theta + \frac{4\pi}{3}) & M_{rs}\cos(\Theta + \frac{2\pi}{3}) \\ M_{rs}\cos(\Theta + \frac{2\pi}{3}) & M_{rs}\cos(\Theta) & M_{rs}\cos(\Theta + \frac{4\pi}{3}) \\ M_{rs}\cos(\Theta + \frac{4\pi}{3}) & M_{rs}\cos(\Theta + \frac{2\pi}{3}) & M_{rs}\cos(\Theta) \end{pmatrix} \quad (3.12)$$

$$\mathbf{L}_{rr} = \begin{pmatrix} M_r + L_{r\sigma} & -0.5M_r & -0.5M_r \\ -0.5M_r & M_r + L_{r\sigma} & -0.5M_r \\ -0.5M_r & -0.5M_r & M_r + L_{r\sigma} \end{pmatrix}. \quad (3.13)$$

The inductance matrix is now completely determined for the physical stator and rotor voltages and currents. However, it is possible to transform it to an arbitrary reference frame, refer to [40].

The next step is to define the \mathbf{R}' matrix which can be expressed as,

$$\mathbf{R}' = \mathbf{R} + \frac{d\mathbf{L}}{dt}. \quad (3.14)$$

The expression for the \mathbf{R} matrix can be expressed as

$$\mathbf{R} = \begin{pmatrix} R_s & 0 & 0 & 0 & 0 & 0 \\ 0 & R_s & 0 & 0 & 0 & 0 \\ 0 & 0 & R_s & 0 & 0 & 0 \\ 0 & 0 & 0 & R_r & 0 & 0 \\ 0 & 0 & 0 & 0 & R_r & 0 \\ 0 & 0 & 0 & 0 & 0 & R_r \end{pmatrix}. \quad (3.15)$$

The model of the IM is now described using the phase voltages as input. However, the phase voltage is not well defined when the IM is fed with a PWM voltage since the sum

of the phase voltages do not equal zero (as for a balanced sinusoidal voltage). Hence, it is more convenient to use the line to line voltages as inputs. It is further assumed that

$$i_a + i_b + i_c = 0. \quad (3.16)$$

The system equations can easily be modified, and by using (3.16) the system can be expressed using two line to line voltages as inputs.

In order to simplify the expression the following variables are defined,

$$A_1 = \cos(\Theta) \quad (3.17)$$

$$A_2 = \cos\left(\Theta + \frac{2\pi}{3}\right) \quad (3.18)$$

$$A_3 = \cos\left(\Theta + \frac{4\pi}{3}\right) \quad (3.19)$$

$$B_1 = \sin(\Theta) \quad (3.20)$$

$$B_2 = \sin\left(\Theta + \frac{2\pi}{3}\right) \quad (3.21)$$

$$B_3 = \sin\left(\Theta + \frac{4\pi}{3}\right). \quad (3.22)$$

By rearranging the \mathbf{L} and \mathbf{R} matrix in order to suit the line to line voltages u_{a-bs} , u_{b-cs} , u_{b-cr} and u_{b-cr} and furthermore eliminating i_{cs} and i_{cr} , \mathbf{L} and \mathbf{R} can be expressed as

$$\mathbf{L} = \begin{pmatrix} 1.5M + L_{s\sigma} & -1.5M - L_{s\sigma} & M(A_1 + A_2 - 2A_3) & M(-A_1 + 2A_2 - A_3) \\ 1.5M - L_{s\sigma} & 3M + 2L_{s\sigma} & M(A_1 - 2A_2 + A_1 + A_3) & M(2A_1 - A_2 - A_3) \\ M(A_1 - 2A_2 + A_3) & M(-A_1 - A_2 + 2B_3) & 1.5M + L_{r\sigma} & -1.5M - L_{r\sigma} \\ M(A_1 + A_2 - 2A_3) & M(2A_1 - A_2 - 3B_3) & 1.5M - L_{r\sigma} & 3M + 2L_{r\sigma} \end{pmatrix} \quad (3.23)$$

$$\mathbf{R} = \begin{pmatrix} R_s & -R_s & 0 & 0 \\ R_s & 2R_s & 0 & 0 \\ 0 & 0 & R_r & -R_r \\ 0 & 0 & R_r & 2R_r \end{pmatrix}. \quad (3.24)$$

The \mathbf{U} matrix can now be defined as

$$\mathbf{U} = \begin{pmatrix} u_{a-bs} \\ u_{b-cs} \\ u_{a-br} \\ u_{b-cr} \end{pmatrix} \quad (3.25)$$

The electrical state derivatives can be expressed in the \mathbf{x} matrix as

$$\mathbf{x} = \begin{pmatrix} i_{as} \\ i_{bs} \\ i_{ar} \\ i_{br} \end{pmatrix}. \quad (3.26)$$

The \mathbf{U} matrix can now be expressed as,

$$\mathbf{U} = \mathbf{L} \cdot \dot{\mathbf{x}} + \left(\mathbf{R} + \frac{d}{dt} \mathbf{L} \right) \cdot \mathbf{x}. \quad (3.27)$$

The electrodynamic torque, T_e , can be expressed as

$$T_e = \frac{p\sqrt{3}M}{2} [(B_1 i_{ra} + B_2 i_{rb} + B_3 i_{rc}) i_{sa} + (B_1 i_{rb} + B_2 i_{rc} + B_3 i_{ra}) i_{sb} + (B_1 i_{rc} + B_2 i_{ra} + B_3 i_{rb}) i_{sc}]. \quad (3.28)$$

The rotor speed derivative can be expressed as

$$\frac{d}{dt} \omega = \frac{p}{J} (T_e - T_L) \quad (3.29)$$

where p and J is the number of pole pairs and the moment of inertia respectively and T_L is the load applied to the motor.

3.1.2 Steady state modeling

A steady state model of the IM, corresponding to the dynamic model presented in previous section can be described with the Y-equivalent circuit shown in figure 3.1. In order to include the iron losses and the stray losses the circuit needs to be modified according to [10] and are presented in figure 3.2. The difference is the the resistance in parallel with the rotor leakage inductance. This resistance, R_{stray} , represents the stray losses in the rotor circuit. This results from studies made on the stray losses [11], showing that the stray losses are proportional to the square of the shaft torque. In addition, [11] has further shown that the stray losses are proportional to the operating frequency. Hence, R_{stray} can be expressed as

$$R_{stray}(f) = R_{stray50Hz} \frac{f}{50}. \quad (3.30)$$

The iron losses are represented by R_c and are also dependent on the frequency. The value of R_c as a function of the frequency are calculated from measurement, refer to Section 3.1.3.

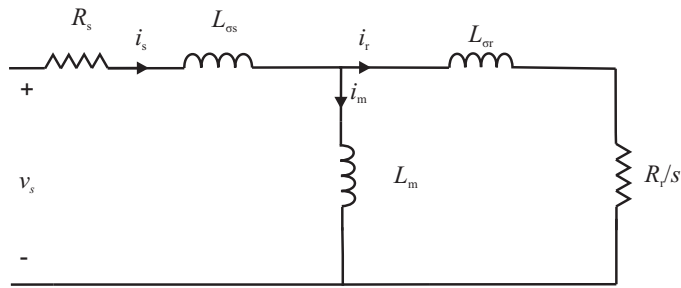


Figure 3.1 Y-equivalent circuit of an IM neglecting the iron and stray losses.

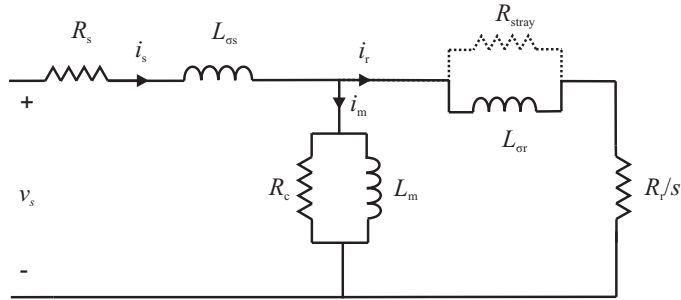


Figure 3.2 Y-equivalent circuit of an IM including iron and stray losses.

3.1.3 Parameter identification

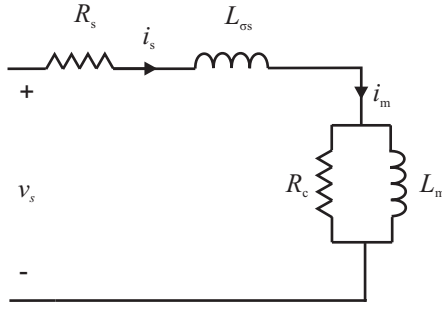
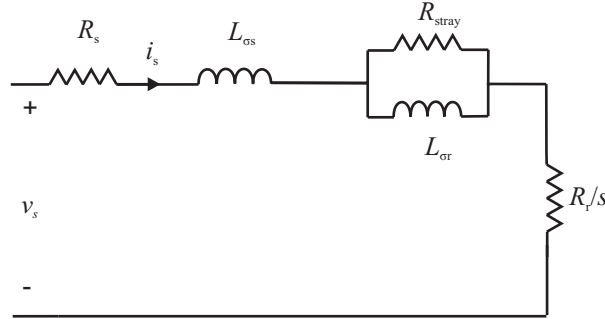
The IM parameters can be calculated from the motor design or be identified using different series of tests. The stator resistance can be obtained by by measuring the line to line DC resistance R_{DC} . The per phase stator resistance is then half R_{DC} .

When the IM is running at no load, the sum of the core losses and the mechanical losses, P_{cm} , can be established. At no load, the rotor part of the circuit is open and s approximately equals zero,

$$\frac{R_r}{s} = \infty, \quad (3.31)$$

and the resistance and the inductance on the rotor side can be ignored. To separate the mechanical and the core losses a test named *the no load test* has to be performed. The measured quantities required for *the no load test* are

- The no load input power P_0 (P_0 includes the resistive loss ($P_{Cu} = 3I^2 R_s$), the core loss, P_{core} , and the mechanical loss, P_{mecl})
- The no load line current, I_0
- The phase voltage U_{ph}
- The stator resistance R_s


 Figure 3.3 Y-equivalent circuit of an IM at no load, $s = \infty$.

 Figure 3.4 Y-equivalent circuit of an IM with locked rotor, $s=1$, neglecting L_m and R_c .

The mechanical losses and the core losses can be obtained by subtracting the resistive stator losses from the total losses. To separate the core losses from the mechanical losses, the sum of the two losses can be plotted against the square of the phase voltage, U_{ph} , since the core loss is proportional to U_{ph}^2 , where U_{ph} is ranging from 125% of its rated value down to the value where the current is increased, according to [45]. Linear regression is performed on the measured values, which results in the best linear approximation. The mechanical loss P_{mecl} can now be obtained from the plot where the voltage $U_{ph}^2=0$ (since P_{mecl} is independent of U_{ph}).

Finally, R_c can be calculated as

$$R_c = \frac{3|(\mathbf{U}_{ph} - \mathbf{I}_0 R_s - \mathbf{I}_0 j\omega L_{\sigma s})|^2}{P_{core}}. \quad (3.32)$$

In order to avoid losses caused by switching harmonics, the motor has in this work been fed by a pure sinusoidal at the no load test. As a result, only the fundamental iron loss component will be obtained.

The remaining components can now be estimated by measuring the phase voltages and current at no load and at locked rotor, refer to figure 3.3 and 3.4.

The stator and rotor leakage inductances can be calculated from the locked rotor test

$$X_{r\sigma} + X_{s\sigma} = \Im\left[\frac{\mathbf{U}_{ph}}{\mathbf{I}_{lock}}\right] \quad (3.33)$$

a common assumption is that,

$$X_{r\sigma} = X_{s\sigma}. \quad (3.34)$$

R_r is calculated as

$$R_r = \Re\left[\frac{\mathbf{U}_{ph}}{\mathbf{I}_{lock}}\right] - R_s \quad (3.35)$$

Finally, the magnetizing inductance is estimated from the no load voltage and current. By calculating the reactive power, Q , the magnetizing inductance can be obtained as,

$$X_m = \frac{3|(\mathbf{U}_{ph} - \mathbf{I}_0 R_s - \mathbf{I}_0 j\omega L_{\sigma s})|^2}{Q - 3I_0^2 \omega L_{\sigma s}}. \quad (3.36)$$

The resistance representing the stray losses in (3.30), $R_{stray50Hz}$ can be estimated by approximating the stray losses at rated output power presented in different standards (IEC, IEEE). However, the standards are not in agreement [10]. Stray losses of 0.5-2.5% of the rated output power are proposed, depending on the motor rating, (the relative stray loss component increases with decreasing motor rating). By assuming that the stray losses are $x\%$ of the rated output power, the real part of $R_{stray50Hz}$ in parallel with $X_{r\sigma}$ can be calculated as,

$$\Re\left[\frac{R_{stray50Hz} j X_{r\sigma}}{R_{stray50Hz} + j X_{r\sigma}}\right] = \frac{x}{100} \frac{P_{mecN}}{3I_{rN}^2} \quad (3.37)$$

It is now straight forward to calculate $R_{stray50Hz}$.

All parameters in the equivalent circuit can now be determined. However, the parameters are not constant in the operating region of the IM. Following list describes how the motor parameters are affected during the operation.

- R_s : The stator resistance is temperature dependent. When the temperature increases the resistivity increases, increasing the stator resistance and hence the stator losses. The temperature coefficient for copper is approximately $39(10^{-3}/^\circ\text{C})$ meaning that a 50°C increase in temperature results in approximately 20% increase of the stator resistance.
- R_r : The same reasoning as for the rotor resistance. However, the rotor often consists of aluminium instead of copper, having a temperature coefficient of $43(10^{-3}/^\circ\text{C})$
- $L_{\sigma x}$: The leakage inductance in the motor are dependent on the magnitude of the current. A reasonable parameter value changes is 2% for a motor with open slots [46].
- L_m : The magnetizing inductances in the motor is mainly dependent on the magnetizing current and decreases with increasing current. An example of parameter

changes are 10% increase in L_m when the magnetizing current decreases with 20% [46].

- R_c : R_c is only a function of the frequency given that the flux level are below the nominal value.
- R_{stray} : The uncertainties are already discussed above.

3.2 Permanent magnet motor modeling

The topic of BLDC and PMSM modeling has been well documented in the literature [47, 48]. However, usually only general models, which are not straightforward to implement are presented, therefore, a more detailed model of a BLDC motor will be explained in this section, suited for control analysis when the motor is fed with a converter. Furthermore, Finite Element method (FEM) modeling of permanent magnet motors will be presented.

3.2.1 Dynamic modeling of a BLDC motor

The general state space model is expressed in (3.38), where L_s and R_s represents the per phase self inductance and resistance respectively, M the mutual inductance and e_x the back emf of phase x.

$$\begin{pmatrix} v_a \\ v_b \\ v_c \end{pmatrix} = \begin{pmatrix} R_s & 0 & 0 \\ 0 & R_s & 0 \\ 0 & 0 & R_s \end{pmatrix} \begin{pmatrix} i_a \\ i_b \\ i_c \end{pmatrix} + \begin{pmatrix} L_s - M & 0 & 0 \\ 0 & L_s - M & 0 \\ 0 & 0 & L_s - M \end{pmatrix} \begin{pmatrix} \frac{di_a}{dt} \\ \frac{di_b}{dt} \\ \frac{di_c}{dt} \end{pmatrix} + \begin{pmatrix} e_a \\ e_b \\ e_c \end{pmatrix}. \quad (3.38)$$

However, the phase voltages v_a , v_b and v_c are not known for the same reason as for the induction motor model presented in Section 3.1.1. Hence, the model is modified in order to satisfy the line to line voltages as inputs. It is also assumed that the sum of the phase currents equals zero. The model can now be written according to (3.39) and (3.40)

$$\begin{pmatrix} v_{ab} \\ v_{bc} \end{pmatrix} = \begin{pmatrix} R_s & -R_s \\ R_s & 2R_s \end{pmatrix} \begin{pmatrix} i_a \\ i_b \end{pmatrix} + \begin{pmatrix} L_s - M & -L_s + M \\ L_s - M & 2(L_s - M) \end{pmatrix} \begin{pmatrix} \frac{di_a}{dt} \\ \frac{di_b}{dt} \end{pmatrix} + \begin{pmatrix} e_{ab} \\ e_{bc} \end{pmatrix}, \quad (3.39)$$

where

$$i_c = -i_b - i_a. \quad (3.40)$$

It is now straight forward to implement the model in Matlab Simulink for evaluation of the controller and calculations of converter losses. However, in order to determine the losses in the motor a more accurate motor model is needed using FEM modeling.

3.2.2 FEM modeling of Permanent magnet motors

The goal of the permanent magnet motor drive system modeling in this thesis is to quantify the relative loss difference between different PM motor topologies, control strategies and motor designs. The difference is expected to be relatively small in some cases which makes it important to establish a detailed model of the drive system, without neglecting important factors such as, nonlinearities in the iron core and iron losses due to harmonic content in the supply. Hence, detailed Finite element method (FEM) modeling will be used. FEM is a numerical method to solve the partial differential equations (PDE) that expresses the physical quantities of interest, in this case Maxwell's equations. This will result in a more accurate result compared to analytical modeling, which can be regarded as a simplification of the PDE.

The software used for modeling is Ansoft Maxwell and Simplorer. Maxwell is a FEM program where the motor model is made. The frequency converter is made in Simplorer, coupled with the FEM model in Maxwell. As a result, the FEM model is solved simultaneously with the converter, taking into account the switched voltage supply.

The Model procedure is as follows:

1. Design of the motor in Maxwell using the tool RMXprt which is an analytical tool for initial designs of motors. This makes it possible to derive a suitable design, iterating many design parameters with relatively short computational time, before making a more detailed FEM analysis.
2. Creating a FEM model in Maxwell. RMexp makes all the basic settings automatically (2D or 3D), which makes it easy to quickly get a working FEM model. However, in order to improve the accuracy, many different modifications needs to be done.
3. Setup the Maxwell model to be connected to Simplorer.
4. Build the frequency converter and the control scheme in Simplorer and connect it to the Maxwell model.

Model simplifications

Factors that can be taken into account are eddy current effects in the magnet material and effects of the harmonics in the magnetic field when calculating the iron losses. However, there are of course assumptions made that will reduce the accuracy of the model. The following approximations/simplifications are made compared to the actual motor.

1. 2D. The largest saving in computation time is made by doing the simulation in 2D instead of 3D. The difference is investigated in Chapter 6. The analyze will be fairly

limited due to the large increase in simulation time, approximately 4 minutes per time step compared to 5 seconds for a corresponding 2D model.

2. Skewing effect will not be accounted for in 2D.

3. Post processing of the iron losses in the stator. The effect of the losses does not have any impact on the calculated quantities. It should be noted that it is possible to include the effect of the stator iron losses on the field calculations in the software. However, the simulation time and stability is highly affected.

4. Iron quality. The data of the stator lamination are obtained from data sheets and gives a maximum loss for a given frequency. As a result, the actual iron loss curve as a function of magnetic flux density and frequency can be different. Furthermore, usually only the loss curves for 50Hz, 100Hz, 200Hz, 400Hz, 1000Hz and 2500Hz are given in the data sheet, for higher frequencies Maxwell interpolates.

5. BH-curve. The data used is only valid for one frequency component, eg 50Hz. Hence, larger frequency components will not be correctly modeled. Especially the current ripple that has frequency components of several kHz. As the frequency increases, the relative permeability decreases. Hence, the current ripple is expected to be underestimated since the inductance seen by the current ripple is much higher in the model than the actual one. This simplification will not be analyzed any further but will be pointed out when simulation results are compared to measurements. It should also be pointed out that the leakage inductance will be underestimated in a 2D model, counteracting the possible decrease in current ripple.

6. Proximity losses arise from induced currents in the stator windings due to a varying magnetic field. The stator resistance is obtained from a DC measurement. Hence, proximity losses and skin effects are not taken into account, which results in an underestimate of the actual stator resistance. Analytical estimation has been presented in the literature, [22], by neglecting the eddy current redistribution effect, the proximity loss per unit length can be expressed as

$$P_{prox} = \left[\frac{\pi d^4 \omega^2 B^2}{128 \rho_{Cu}} \right] \quad (3.41)$$

where d is the diameter of the wire, ω is the angular velocity of the flux component, B is the peak value of the flux density and ρ_{Cu} is the resistivity of the conductor. The interested reader can refer to [22] for a more detailed analyze.

Iron loss calculation

Iron loss calculation in electrical machines is a challenging task especially for non sinusoidal excitation. An often used method is the Steinmetz equation that calculates the core losses as

$$P_{core} = k_h f B^\beta + k_c f^2 B^2 + k_e f^{1.5} B^{1.5} \quad (3.42)$$

where k_h , k_c and k_e β are empirical determined constants for the given material and B is the peak magnetic field density [49]. The parameters are determined under sinusoidal excitation and (3.42) will not be useful for motor with non sinusoidal emf waveform and non sinusoidal motor supply. Instead the so called modified Steinmetz equation has been used in the literature

$$P_{core} = (C_m f_{eq}^{\alpha-1} B^\beta) k_h f B^\beta f \quad (3.43)$$

where f_{eq} is an equivalent frequency of the non sinusoidal waveform and f is the fundamental component, C_m α β are empirical parameters [49]. This model of the iron losses is only useful in the frequency domain and is not suitable for a transient model of a converter driven motor.

To the best knowledge of the author, the method used by the software uses a time domain model, presented in [49]. The instantaneous hysteresis loss, p_h , eddy current loss, p_c and excess loss, p_e can be expressed as,

$$p_h = H_{irr} \frac{dB}{dt} \quad (3.44)$$

$$p_c = \frac{1}{2\pi^2} k_c \left(\frac{dB}{dt} \right)^2 \quad (3.45)$$

$$p_e = \frac{1}{C_e} k_e \left| \frac{dB}{dt} \right|^{1.5} \quad (3.46)$$

where H_{irr} is the irreversible component of the H field, k_c , k_e and C_e are empirical constants.

3.3 Loss modeling of frequency converters

This section will present the assumptions made for estimating the losses in the frequency converter. The losses consists of switching losses and conductive losses. Typical switching characteristics were presented in Section 2.3. The switching loss for a component during a switching transition can be calculated as

3.3. Loss modeling of frequency converters

$$W_{sw} = \int_{t_1}^{t_2} u(t)i(t)dt \quad (3.47)$$

where $u(t)$ and $i(t)$ are the voltage over the component and the current through the component during the switching interval and t_1 to t_2 is the time duration of the switching transition. The shape of $i(t)$ and $u(t)$, level and time duration, can be measured or in some extent be obtained from data sheets. In many cases loss curves are presented in the data sheet, for typical converter setups (DC voltages, gate resistance and temperature), as a function of current and can be used as lookup tables for the losses at each transition. If this information is not available, a good approximation can be to assume that the losses at each switching instant are proportional to the current and voltage at the switching instant. Hence, the power dissipation in a component x can be expressed as

$$P_{swx} = k_x f \sum_{i=1}^n I_i \quad (3.48)$$

where k_x is a constant for component x (or calculated from the loss curves for the given current), f is the fundamental frequency I_i is the current magnitude at a switching instant and n is the number of switching instants during one period of the fundamental.

The conductive losses in a component depends on the voltage drop across the component U_{on} as a function of the on-state current, I_{on} . The voltage drop is dependent on both the current magnitude and the temperature of the component. The characteristics can be obtained from data sheets to some extent. However, it is fairly easy to obtain U_{on} as a function of the temperature and current from measurements. Given $U_{on}(I_{on})$ and I_{on} , the power dissipation can be calculated as

$$P_{cx} = f \sum_{i=1}^n U_{on}(I_i) I_i t_i \quad (3.49)$$

where t_i is the time duration of the conduction i and the sum includes one period of the fundamental.

The losses in the converter are now modeled and can be estimated for a given current and switching pattern.

Chapter 4

Field measurements on HVAC applications

This chapter will present the results obtained from the field measurements that have been performed. One commercial building has been the target of a long period of measurement in order to establish the power demand of different applications but also to investigate the dimensioning of the drive systems.

4.1 Field measurements

Field measurements have been performed on five different pump applications in an office building. The electrical power has been measured with CEWE DQ 235 power meters and logged each minute. This section will present the most interesting result from this study.

Figure 4.1 shows a schematic over a part of the pump system. Pump p_1 is the main pump on the heating side, serving a number of branches including a radiator circulator and a floor heating circulator, referred to as p_2 and p_2 respectively. Pump p_1 is a PMSM type with a rating of 450W, operating at a constant pressure of 4.5m. Note that the rated power is given for the electrical input power. Figure 4.2 shows the distribution of the electrical power to the pump from June 2006 to April 2008. It can be noted that the operating power is at maximum 50% of the rated power.

Pump p_2 is a variable speed pump using an IM rated at 250W. It serves 70 radiators and is operated at a constant pressure of 1.1m. The pump is turned off when the outdoor temperature is above 20°. The temperature of the circulating water is controlled by a valve mixing the return water from the radiators with the water delivered from the main pump. Figure 4.3 shows the distribution of power demand of the pump for the period June 2006 to April 2007. It can be noted that also in this case the maximum electrical power input is approximately 50% of the rated power.

Pump p_3 is of a constant speed type and is turned off when the outdoor temperature is above 18° otherwise its turned on. The power demand of the pump can be seen in figure

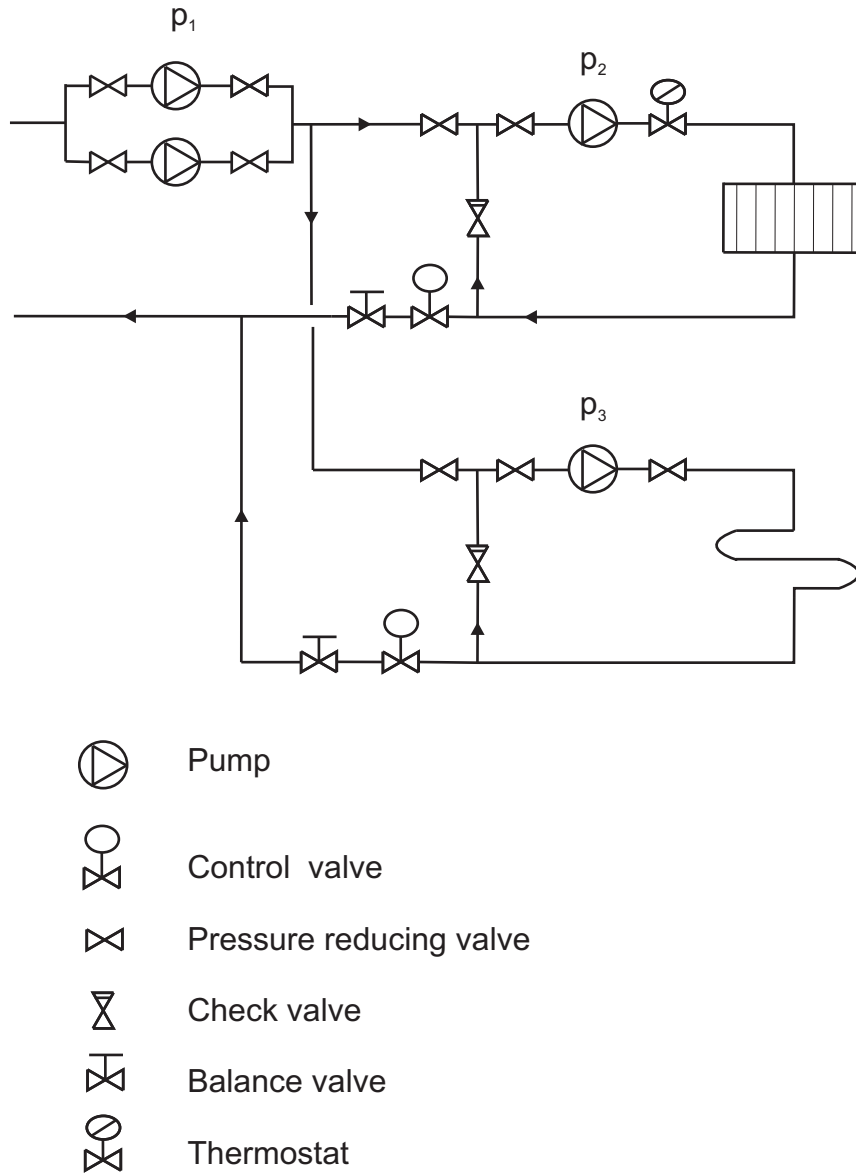


Fig. 4.1 Overview of one part of the pumping system including the main pump (p_1), radiator pump (p_2) and the floor heating pump (p_3)

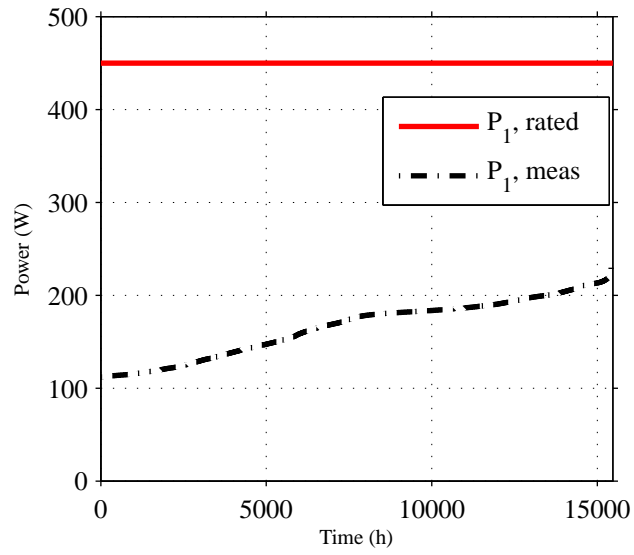


Fig. 4.2 Electrical input power the main pump during June 2006 to April 2008

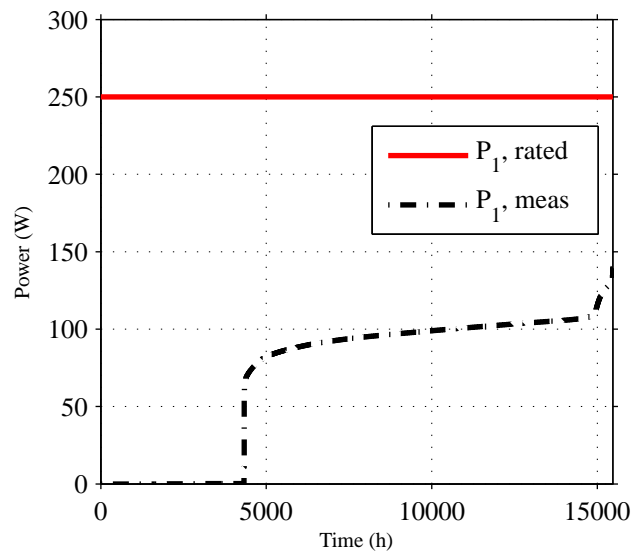


Fig. 4.3 Electrical power demand of the radiator circulator during June 2006 to April 2008

4.4 for the same time distribution as above.

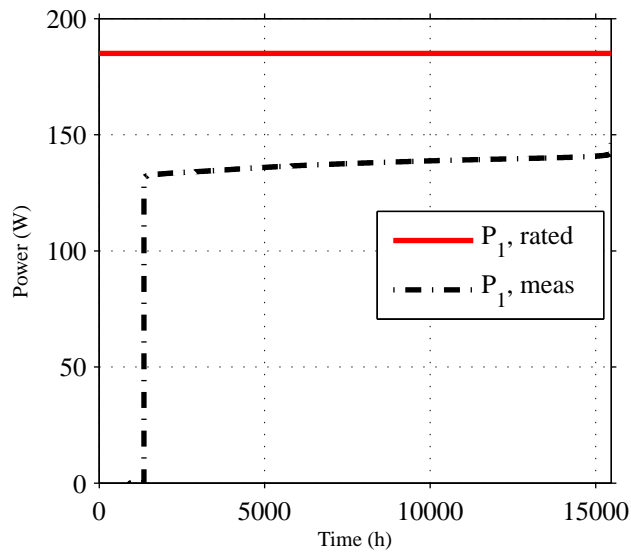


Fig. 4.4 Electrical power demand for the floor heating circulator during June 2006 to April 2007

Measurement has been also been carried out on a pump serving a cooling coil. The pump is a dry rotor pump of variable speed type with an IM, rated at 1.5kW. Figure 4.5 shows the input power distribution for the same period as above. It should be noted that the rated value for dry pumps are given for the mechanical output power of the motor. Hence, it can be noted that the motor is over dimensioned by far more than 100% referred to the electrical input power need.

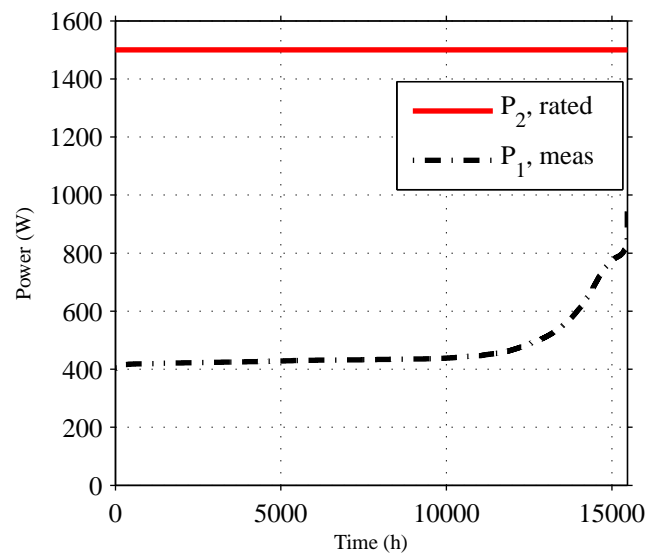


Fig. 4.5 Electrical input power to pump 4 during June 2006 to April 2008

Chapter 5

Efficiency determination of different Induction motor drive systems

Improvements of energy efficiency in a frequency converter and IM can be achieved either by changing the design or using different control schemes. This chapter will investigate the impact on efficiency in the IM using different design, control techniques and comparing different motor ratings. Furthermore, different switching techniques will be investigated.

5.1 Induction motor setup

This section will present the energy efficiency of an IM and its dependence on motor design and control. Simulations have been carried out which are further used in Chapter 10 for determination of potential HVAC savings.

5.1.1 Comparison between different motor designs

This section will focus on the difference between the efficiency using eff1-eff3 motors described in Section 2.1. The motors under test is labeled with the eff labels and not according to the new standard, IE1-IE3. However, IE1 and IE2 corresponds to eff2 and eff1 respectively, and IE3 are not yet available for IM below 11kW as was mentioned in Section 2.1. The stationary model of the IM will be used together with the method presented in Section 3.1.3 for parameter identification.

Parameter identification has been performed on a 4-pole 4kW standard eff3 IM and a corresponding eff1 IM. The parameters are presented in Table 5.2.

The parameters are now modified in order to suit an eff2 IM. The efficiency at 75% rated output power operating at rated voltage/frequency is assumed to increase 2% for an eff2 compared to the eff3 IM. The following assumptions have been made:

Table 5.1 Motor data

Parameter	Eff3	Eff2	Eff1
R_s	1.5Ω	1.28Ω	1Ω
R_r	1.3Ω	1.3Ω	0.9Ω
$R_{c,50Hz}$	606Ω	760Ω	984Ω
$R_{stray50Hz}$	9.89Ω	8.13Ω	7.5Ω
$L_{\sigma s}$	8mH	8mH	7mH
$L_{\sigma r}$	8mH	8mH	7mH
L_m	0.14H	0.14H	0.14H
P_{mecN}	4kW	4kW	4kW
n_N	1435rpm	1445rpm	1455rpm
U	3x400V	3x400V	3x400V
I_{sN}	9.1A	9.0A	8.6A

- R_r : The value for an eff2 IM is unchanged
- R_s : More copper is used in the stator winding, resulting in a reduced stator resistance. It is assumed to be 15% lower for eff2 IM.
- R_c : The rest of the increased efficiency is tuned in by increasing R_c by using improved iron grade or thinner laminations.
- $R_{stray50Hz}$: The stray losses are still assumed to be 2% of the rated output power. However, the value needs to be modified since the operating condition has changed due to the modified motor parameters
- The inductances are assumed to be unchanged.

Section 5.1.3 will present simulation results of the eff3 and eff1 motor.

5.1.2 Energy optimal control of the Induction motor

The torque characteristics of an IM was briefly discussed in Section 2.1. It was stated that a simple control technique of an IM is to use constant V/Hz control, meaning that the ratio of the voltage and frequency is kept constant. As a result, the magnetic flux in the motor is kept constant which makes it possible to load the IM with its rated torque even at low frequencies. However, an operating point can be achieved with different sets of V/Hz as can be seen in figure 5.1, it must be emphasized that the slopes of the curves are exaggerated for the purpose of illustration. It can be noted that the slip is increasing when the slope of the T - n -curve is decreased, resulting in an increased current and thereby higher resistive losses. On the other hand, since the voltage is decreased, the core losses are lowered. It can be shown that each operating point has its unique V/Hz combination

that minimize the losses in the motor [9]. Figure 5.2 shows an example of the core losses together with the resistive losses for a constant operating point, $(T, n) = (3.7 \text{ Nm}, 800 \text{ rpm})$, as a function of frequency. The efficiency of the IM is also presented and it can be seen in the figure that the maximum efficiency occurs, approximately, when the core and resistive losses intersect. The phase voltage at this operating point has been reduced from 126.5V, operating at constant V/Hz, to 76.4V.

Many loads have a lower torque demand at lower speeds, especially pumps and fans. Hence, it is possible to make substantial energy savings by controlling the motor to its optimal V/Hz.

The oncoming sections will present simulation results of the losses in an IM.

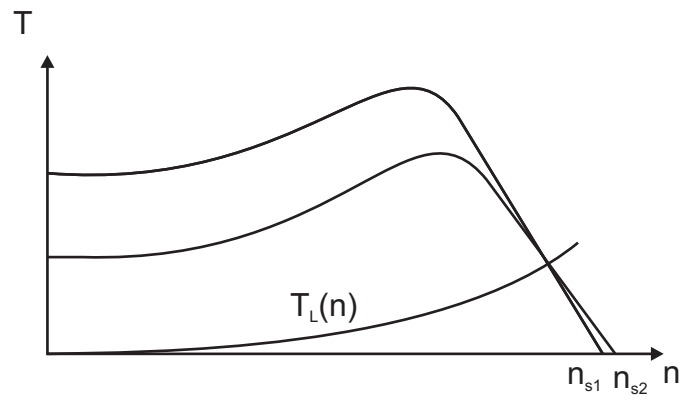


Fig. 5.1 Torque speed characteristics for two different setups of voltage/frequency resulting in identical operating point for the given load.

5.1.3 Efficiency calculation result of different design and control techniques

Calculations have been performed using the steady-state model presented in Section 3.1.2. Different types of motor designs, according to Section 5.1.1, and different V/Hz control, according to Section 5.1.2, have been investigated. The result in this section will be further used in order to investigate the potential savings in HVAC applications, refer to Chapter 10.

4kW 4-pole IM

The efficiency has been calculated for an eff3 and eff1 IM, controlled with constant V/Hz and the eff1 IM with optimal V/Hz. Two different loads was used in the calculations, $T = b_1 \omega^2$ and $T = b_2 \omega$, where b_1 and b_2 are constants resulting in rated torque at rated speed. Figure 5.3 shows the efficiency of the IM with the quadratic load demand and figure 5.4 shows the efficiency using the linear load demand. It should be noted that the voltage is

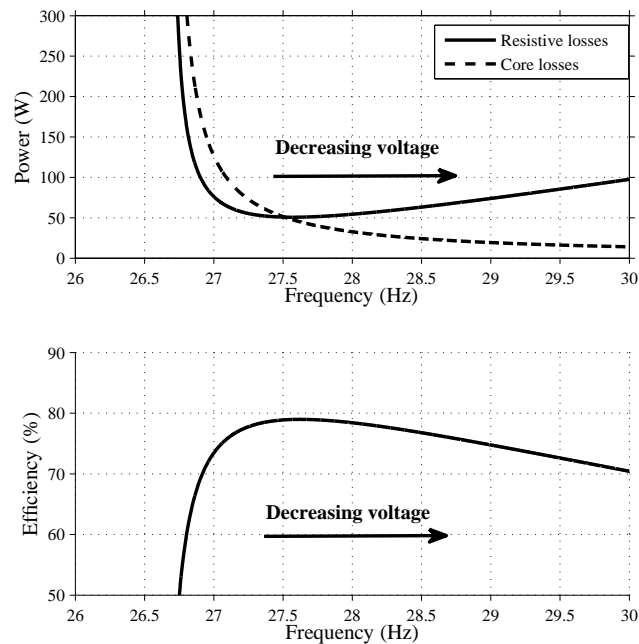


Fig. 5.2 Core and resistive losses in the stator and rotor for a given operating point, $(T, n) = (3.7 \text{ Nm}, 800 \text{ rpm})$, and the resulting efficiency of the IM.

limited to its rated value. As a result, the optimal control of V/Hz will be limited at higher load. For example, the calculated optimal voltage becomes 15% above the rated value at at 100% load demand.

The calculations assumed a load that was ideally dimensioned for the motor, 100% load demand gave the rated power of the motor.

5.2 Influence of over sizing on the efficiency for an IM

Chapter 4 presented results from field measurements made on different HVAC load profiles. It was shown that over dimensioning of the drive system was present in all applications tested. The efficiency for an IM controlled with a constant flux level ($V/\text{Hz} = \text{constant}$) is poor at light load, as was shown in section 5.1.3. However, when the motor is controlled with an energy efficiency optimal flux at each operating point, the efficiency is increased. An interesting issue is how these "over dimensioning losses" are influenced by using efficiency optimal V/Hz control. Is the efficiency still lower for a larger rating, and can it be worth keeping an existing over dimensioned, low efficiency IM if it is to be replaced by a smaller IM rating having a high efficiency energy label? This section determine the efficiency for different motor ratings, 1.1kW -4kW operating with identical loads. Chapter 10 will quantify the results obtained.

5.2. Influence of over sizing on the efficiency for an IM

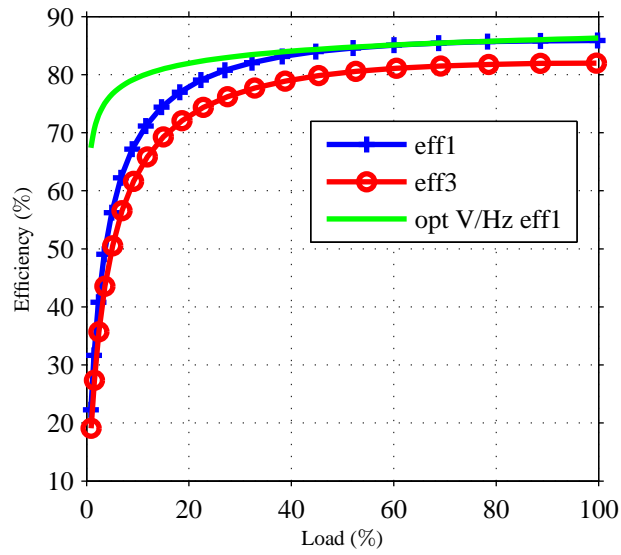


Fig. 5.3 Efficiency of the different IM setups applied to a quadratic load.

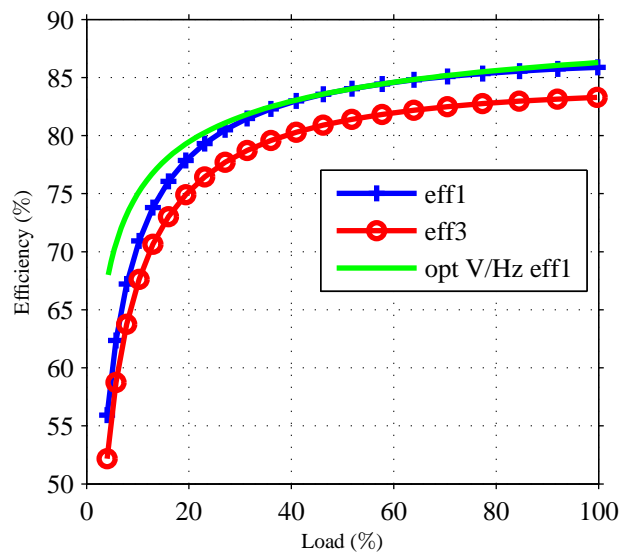


Fig. 5.4 Efficiency of the different IM setups applied to a linear load.

5.2.1 Parameters identification for the case study

Parameter identifications have been performed on five 4-pole eff1 motors, 1.1, 1.5, 2.2, 3 and 4kW, according to Chapter 3. For calculation of $R_{stray50Hz}$, it is assumed that the stray losses are 2% of the rated output power for each IM [11]. R_r is calculated from the locked rotor test at a 20Hz supply instead of 50Hz. The reason is that the physical rotor currents have a frequency that are only a fraction of 50Hz at normal operation and by decreasing the frequency a more accurate value of R_r is obtained due to the skin effect, (approximate skindepth at 20Hz is 19mm for Aluminium and 15mm for copper).

The parameters are presented in Table 5.2 and 5.3, all parameters are referred to the stator side.

Table 5.2 Motor data

Parameter	1.1kW	1.5kW	2.2kW
R_s	5.0Ω	3.0Ω	1.7Ω
$R_{r,20Hz}$	4.7Ω	3.3Ω	2.0Ω
$R_{c,50Hz}$	2457Ω	1861Ω	1543Ω
$R_{stray50Hz}$	14.6Ω	10.3Ω	8.0Ω
$L_{\sigma s}$	19.5mH	13.6mH	10.1mH
$L_{\sigma r}$	19.5mH	13.6mH	10.1mH
L_m	0.48H	0.33 H	0.23H
P_{mecN}	1.1kW	1.5kW	2.2kW
n_N	1420rpm	1440rpm	1450rpm
U	3x400V	3x400V	3x400V
I_{sN}	2.4A	3.2A	4.8A

Table 5.3 Motor data

Parameter	3.0kW	4.0kW
R_s	1.5Ω	1.0Ω
$R_{r,20Hz}$	1.3Ω	0.9Ω
$R_{c,50Hz}$	1733Ω	984Ω
$R_{stray50Hz}$	9.1Ω	7.5Ω
$L_{\sigma s}$	9.5mH	7.0mH
$L_{\sigma r}$	9.5mH	7.0mH
L_m	0.21H	0.14H
P_{mecN}	3kW	4kW
n_N	1455rpm	1455rpm
U	3x400V	3x400V
I_{sN}	6.2A	8.6A

It should be noted that R_c for the 3kW IM differs from the general trend that increased rating results in decreased R_c .

The mechanical losses were obtained from the no load test and are presented in figure 5.5.

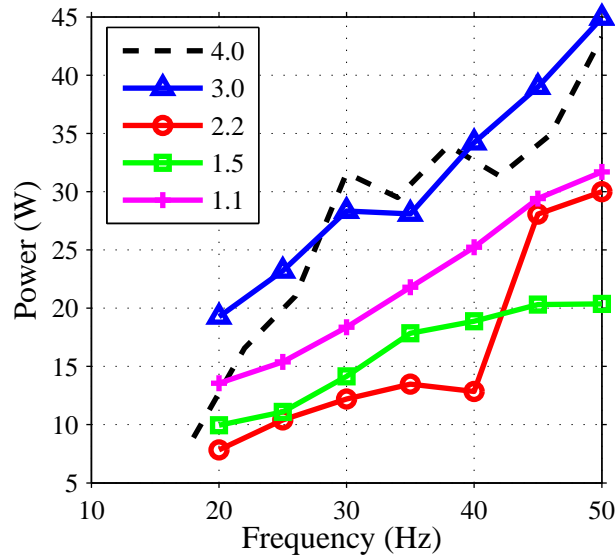


Fig. 5.5 Mechanical losses for the different IM ratings obtained from the no load test, performed according to [45].

5.2.2 Calculation results

The motor efficiency for the different ratings is now calculated using a search algorithm to find the optimal efficiency point. All the losses, including the mechanical losses, are accounted for. Figure 5.6 shows the efficiency of the different motor ratings operated at constant V/Hz ratio. The load characteristic is $T_L = b\omega^2$ where 100% load corresponds to the rated power for each motor. As expected the efficiency increases for increased motor rating except for the 3kW and 4kW motor.

Figure 5.7 shows the efficiency of the different motor ratings operated at constant V/Hz ratio and applied to identical loads where 100% load corresponds to 1.1kW. It can, as anticipated, be noted that the 4kW IM has the lowest efficiency in the operating range.

If the control of the motors are changed from constant V/Hz to an optimized ratio the situation changes. Figure 5.8 shows the efficiency for the different motor ratings.

It is thus quite clear that the increase in mechanical losses using a larger motor is less than the decrease in electrical losses for the calculated scenario.

Another factor that is not discussed yet is the temperature dependence. When the smaller motor rating is used, the higher the temperature becomes since more losses are generated in a smaller volume. Hence, it is evident that if the temperature dependence

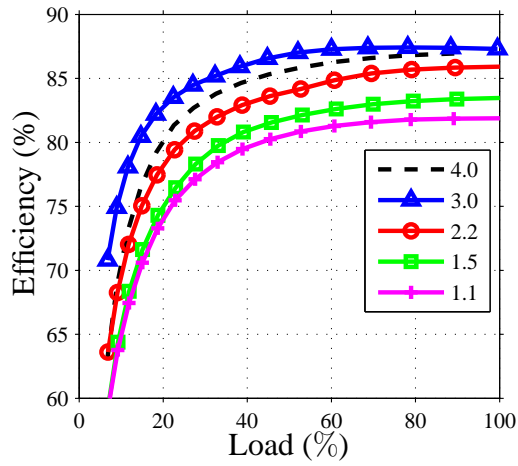


Fig. 5.6 Motor efficiency for constant V/Hz where each motor is operating at its rated load.

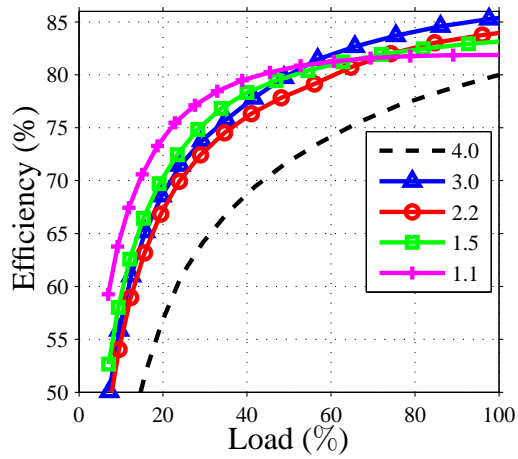


Fig. 5.7 Motor efficiency for constant V/Hz for identical loads where 100% corresponds to 1.1kW.

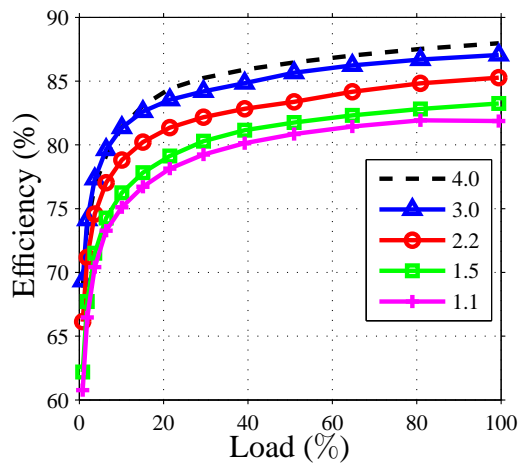


Fig. 5.8 Motor efficiency for optimal V/Hz for identical loads where 100% corresponds to 1.1kW.

where considered, the rotor and stator losses would increase more for the smaller rating, resulting in an even better loss situation for an oversized motor.

Another important factor to consider is the losses in the inverter stage. If the inverter is selected to have the same rating as the motor, the efficiency will be decreased for the larger ratings. Figure 5.9 shows the switching and conductive losses of the inverter stage for different 1200V IGBT modules, having 15A, 25A and 35A current rating respectively. The calculation is made when the inverter is supplying a 4kW IM, connected to the 1.1kW load. The inverter is controlled using a continuous space vector modulation (CSVM) control, with a switching frequency of 10kHz, CSVM will be described in more detail in Section 5.3.3. It can be noted that the increase in switching losses are approximately proportional to the increase of the current rating of the IGBT module. It can further be noted that the conductive losses are decreasing when the current rating increases. However, the total loss component will be larger for the larger IGBT modules. It should be pointed out that, since identical loads are considered for the different motor ratings it is possible to use identical converters resulting in higher overall efficiency due to the lower power flow in the converter for a larger motor rating.

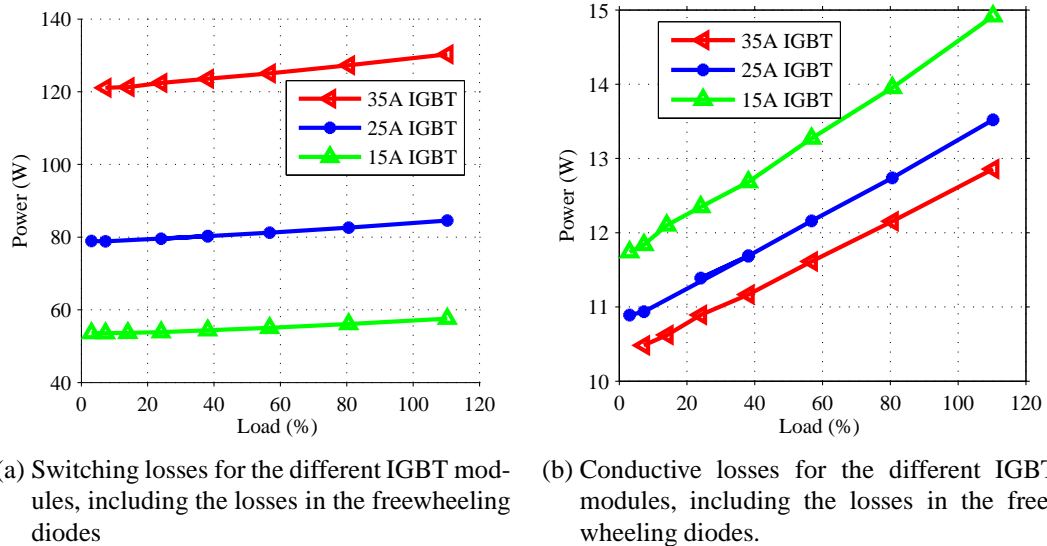


Fig. 5.9 Loss components in different IGBT modules, including freewheeling diodes, when the inverter is connected to the 4kW IM operated at 1.1kW at 100% load. The inverter is operated at 10kHz and controlled with a continuous space vector modulation strategy.

5.3 Frequency converter setup

The basic operation of a frequency converter was described in Section 2.3. The production of a variable voltage and frequency using pulse with modulation (PWM) was described

briefly.

This section will focus on how different PWM schemes affects the efficiency of the converter and motor.

5.3.1 Sinusoidal PWM

Sinusoidal PWM was briefly introduced in the introduction to frequency converter in Section 2.3 since it gives a simple illustration of the PWM technique. However, this method has several drawbacks compared to more advanced techniques. For a modulation index, M , defined as,

$$M = \frac{V^*}{V_s/2} \quad (5.1)$$

where V^* is the amplitude of the reference voltage and V_s is the DC bus voltage, $M=1$ is the maximum value for linear control, . With $M=1$ the line to line voltage, V_{l-l} becomes

$$V_{l-l} = \sqrt{3} \frac{V_s}{2}. \quad (5.2)$$

For an ideal three phase inverter connected to a 400V grid V_s equals the peak value of the $l - l$ voltage, 565V, resulting in a maximum output peak line to line voltage of 490V (approx 87% of the rated value). Hence, it will not be possible to operate an IM at its commonly used rating of 50Hz 400V which is one of the major drawbacks using this technique.

It is possible to increase the amplitude above $M = 1$ by using so called over modulation. However, the nonlinear relationship between M and the voltage magnitude is not desirable from a control point of view. Furthermore, over modulation results in low frequency harmonics. Instead a method to increase the linear control range will be discussed in the next section.

The current ripple will be used as an indicator of the harmonic losses. Assuming a delta connected load and a constant internal emf voltage during a switching transition, the current ripple through a delta load element can be expressed as,

$$I_{ab}^2 = \frac{V_s^2}{4L_\sigma^2} \frac{\Delta T^2}{48} \left[\frac{3}{2} M^2 - \frac{4\sqrt{3}}{\pi} M^3 + \frac{9}{8} M^4 \right] \quad (5.3)$$

where ΔT is half of the switching period. The term L_σ is defined as,

$$L_\sigma = L_{s\sigma} + \frac{L_{r\sigma} L_m}{L_{r\sigma} + L_m} \quad (5.4)$$

where $L_{s\sigma}$ and $L_{r\sigma}$ are the leakage inductances of the stator and rotor respectively and L_m is the magnetizing inductance.

The interested reader can find the derivation in [12].

5.3.2 Sinusoidal PWM using third harmonic injection

It is possible to increase the modulation index above one and still have the linear relationship between M and the voltage reference. This is done by changing the common mode reference voltage. By adding a third harmonic component to the phase voltage references it is possible to increase the modulation index. It can be shown [12] that a 15% increase is possible if the magnitude of the third component is 1/6 of the fundamental. However, this technique introduces low order harmonics. [12] also suggests a 1/4 third harmonic injection in order to improve the harmonic content at the cost of reduced output voltage.

The current ripple, using the same assumption as in (5.3), for the techniques can, according to [12], be expressed as

$$I_{ab1/6}^2 = \frac{V_s^2}{4L_\sigma^2} \frac{\Delta T^2}{48} \left[\frac{3}{2} M^2 - \frac{4\sqrt{3}}{\pi} M^3 + M^4 \right] \quad (5.5)$$

$$I_{ab1/4}^2 = \frac{V_s^2}{4L_\sigma^2} \frac{\Delta T^2}{48} \left[\frac{3}{2} M^2 - \frac{4\sqrt{3}}{\pi} M^3 + \frac{63}{64} M^4 \right]. \quad (5.6)$$

5.3.3 Space Vector Modulation

This section will describe the basics of space vector modulation (SVM) and different SVM schemes purposed in the literature.

A balanced three phase voltages, v_a , v_b and v_c can be transformed to an equivalent voltage vector $v_\alpha + j v_\beta$, where v_α and v_β are defined as

$$\begin{pmatrix} v_\alpha \\ v_\beta \end{pmatrix} = \begin{pmatrix} 1 & 0 & 0 \\ 0 & \frac{1}{3} & -\frac{1}{3} \end{pmatrix} \begin{pmatrix} v_a \\ v_b \\ v_c \end{pmatrix}. \quad (5.7)$$

Figure 5.10 shows the three phase voltage and its equivalent $\alpha \beta$ components.

The $\alpha \beta$ components can now be mapped in the $\alpha \beta$ -plane shown in figure 5.11 where V_1 - V_{12} denotes examples of instantaneous voltage vectors during one period of the fundamental voltage. It is evident that the inverter generates a finite number of voltage vectors

Figure 5.12 shows the different switch combinations possible for a three phase inverter. The stationary space vector in the $\alpha \beta$ plane, created by the different switch states are shown in figure 5.13. Note that the magnitude of space vectors **SV0** and **SV7** are zero. An arbitrary space vector, \mathbf{V}^* , can now be created by switching between the different space vectors. If, for example, \mathbf{V}^* at a time instant is located between **SV1** and **SV2** the vector is created by switching between **SV1**, **SV2** and the zero space vectors **SV0** and **SV7**. During half the switching period, $T_{sw}/2$, \mathbf{V}^* can be expressed as,

$$\mathbf{V}^* = \frac{T_{SV1}}{T_{sw}/2} \mathbf{SV1} + \frac{T_{SV2}}{T_{sw}/2} \mathbf{SV2} \quad (5.8)$$

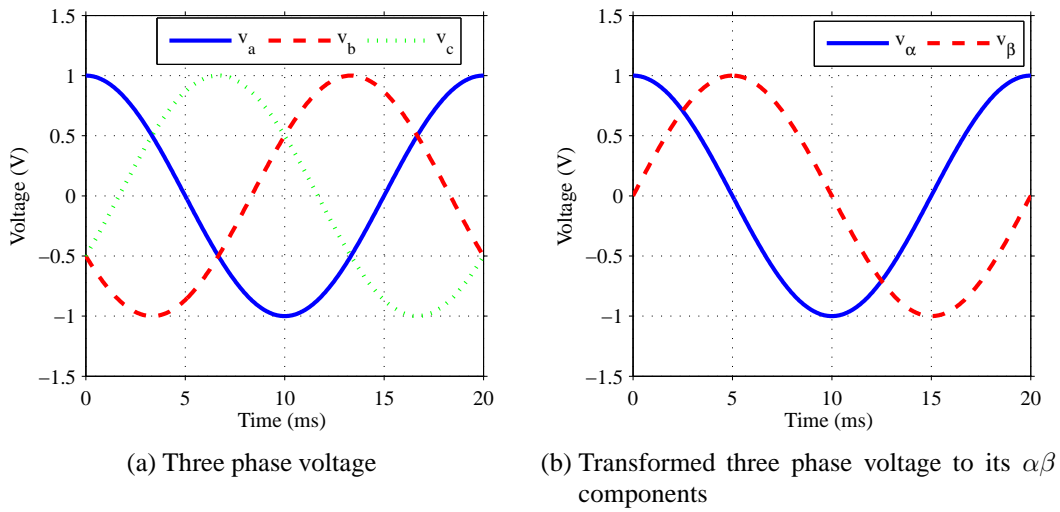


Fig. 5.10 Three phase voltage and its $\alpha\beta$ equivalent.

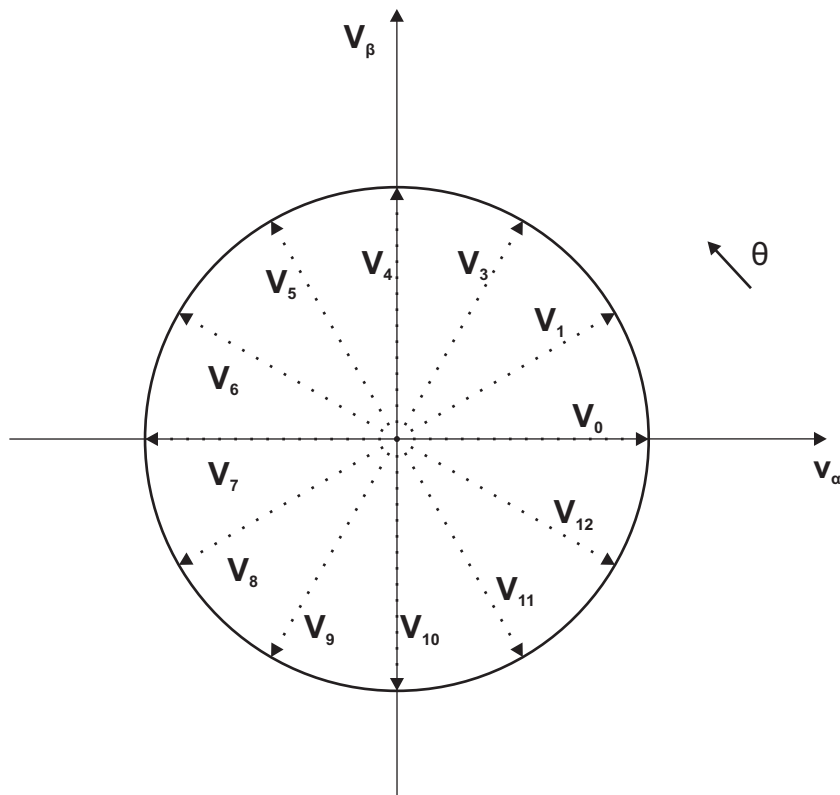


Fig. 5.11 Space vector voltage in the $\alpha\beta$ -plane.

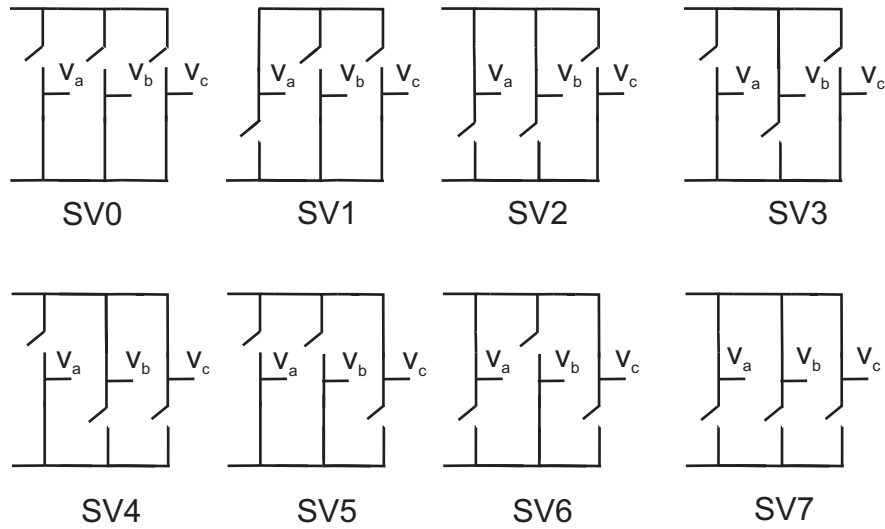


Fig. 5.12 Possible switching states for a three phase inverter.

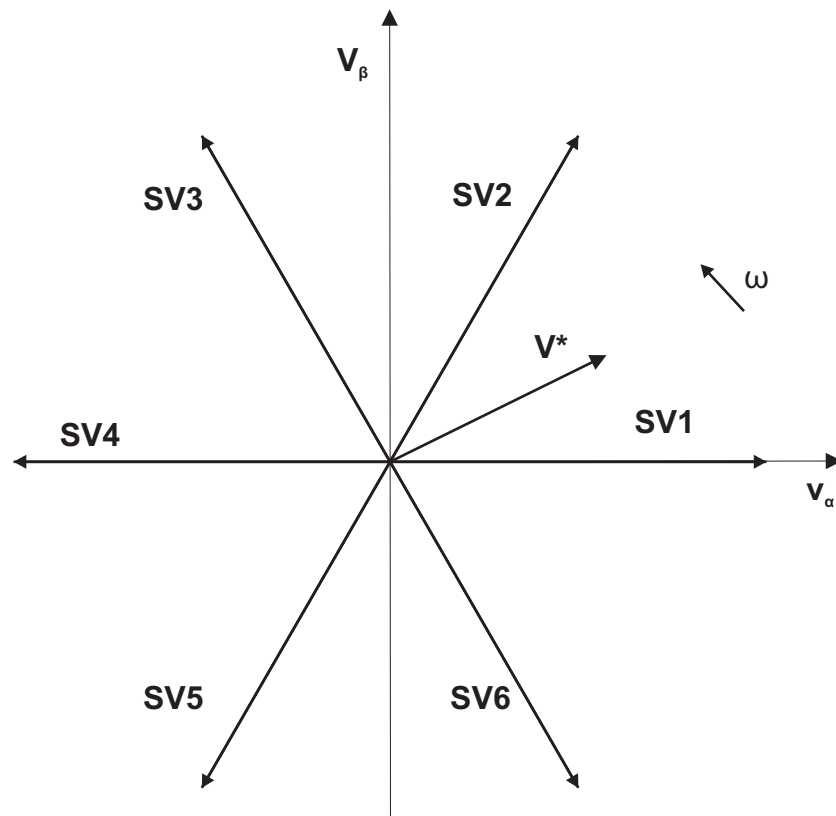


Fig. 5.13 Space vectors for the different switching states. SV0 and SV7 have zero magnitude and are left out in the figure.

where T_{SVx} is the time \mathbf{SVx} is on and T_{sw} is the time of the switching period. The time duration of the zero space vectors can now be defined as

$$T_{SV0} + T_{SV7} = T_{sw}/2 - T_{SV1} - T_{SV2}. \quad (5.9)$$

However, the time distribution between $\mathbf{SV0}$ and $\mathbf{SV7}$ is left undefined as well as the placement of the space vectors. It can be shown, [12], that the space vector placement shown in figure 5.14 should be used in order to achieve the lowest harmonic content. The zero space vectors are symmetrically placed during each switching period as figure 5.14 shows. In order to achieve this pulse pattern a phase leg voltage reference, different from the sinusoidal reference, needs to be determined. For details regarding the derivation of the reference voltage refer to [12]. Figure 5.15 shows the reference voltage for modulation index 0.9. However, as mention in the introduction of this section, optimal harmonic content does not necessarily results in optimal overall efficiency.

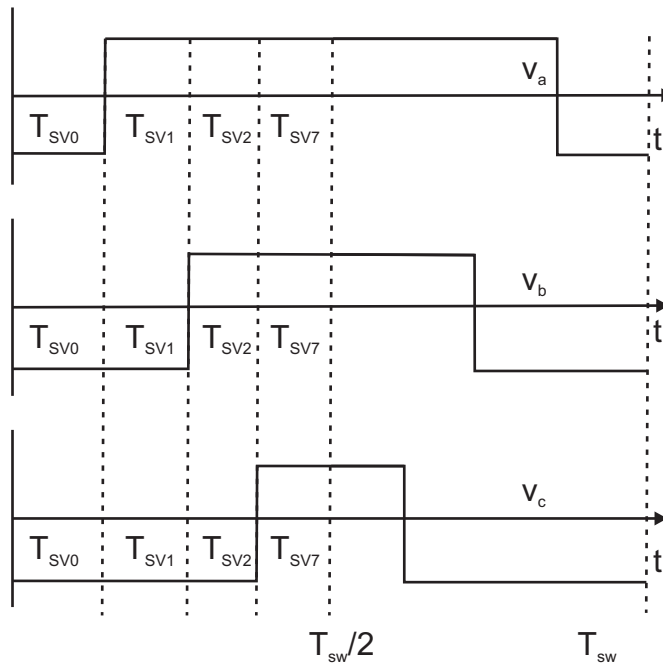


Fig. 5.14 Example of pulse pattern when the voltage reference is located between space vectors $\mathbf{SV1}$ and $\mathbf{SV2}$.

It is possible to rearrange the space vector placement in order to decrease the number of switchings and hence decrease the switching losses. [12] explains in detail different discontinues SVM techniques in order to decrease the switching instants. This section will describe the following techniques.

- 120° Discontinuous PWM modulation Max DPWMMAX
- 120° Discontinuous PWM modulation Max DPWMMIN

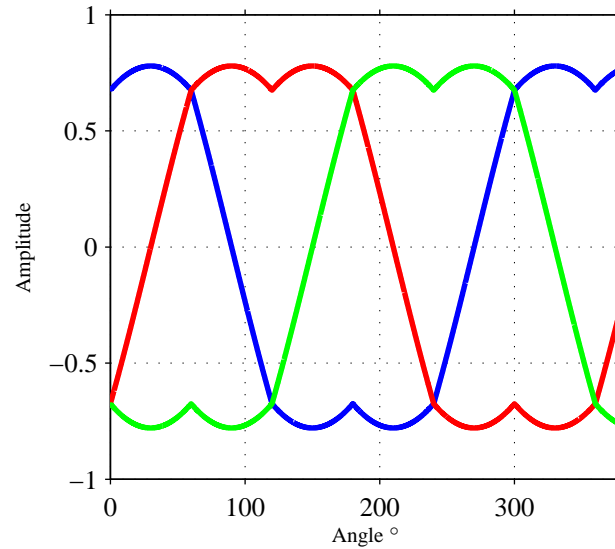


Fig. 5.15 Phase leg reference for SVM.

- 60° Discontinuous PWM modulation Max DPWM60
- 30° Discontinuous PWM modulation Max DPWM30lag

DPWMMAX

This technique is called MAX since it only uses the **SV7** as the zero vector. Furthermore, **SV7** is concentrated at each switching period indicated in figure 5.16. It should be noted that the voltage average during the switching period T_{sw} is equal to the one resulting from the pulse pattern used in figure 5.14. During each 120° interval, one phase leg is clamped to the positive DC bus of the converter.

DPWMMIN

This technique is similar to DPWMMAX. Instead of using **SV7**, **SV0** is used clamping each phase to the negative DC bus for 120°. The result in the decreased switching and the harmonic content are identical to DPWMMAX. Figure 5.17 shows the pulse pattern for the same voltage reference as in the previous case.

DPWM60 and DPWM30lag

It is evident that the losses in each device, using 120° SVM schemes, are not equally distributed. It is possible to switch equally between the MIN MAX technique. Each phase leg is now clamped to the upper and lower DC bus for 60° respectively. The non switching period will now be located around the peak of each phase voltage. As a result, the switching losses will be decreased compared to DPWMMIN or DPWMMAX technique. This

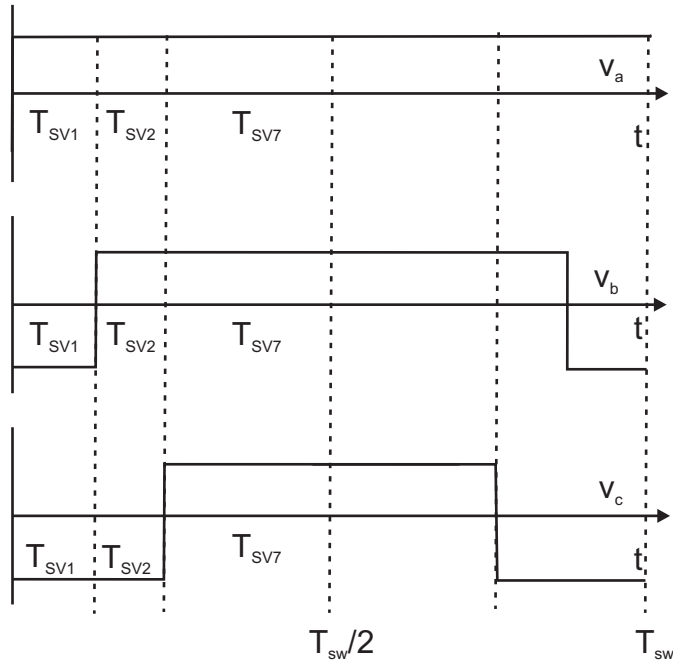


Fig. 5.16 Example of pulse pattern when the voltage reference is located between space vectors SV1 and SV2 for DPWMMAX.

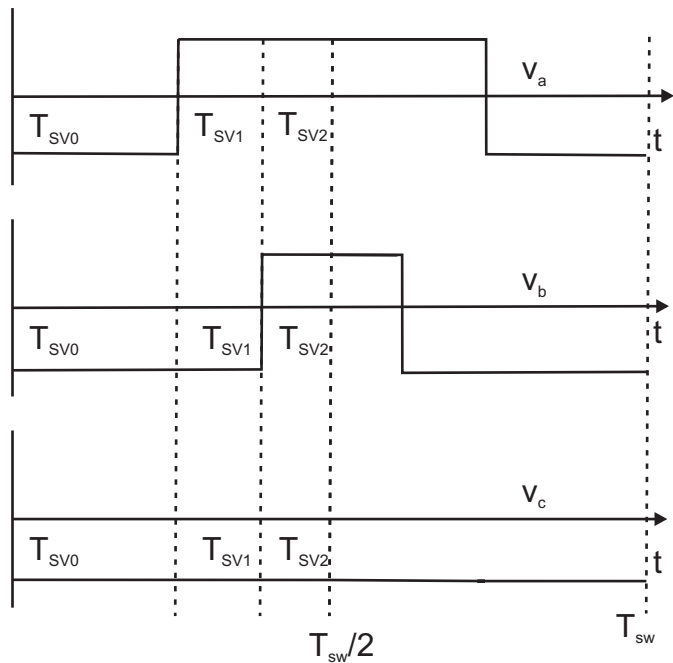


Fig. 5.17 Example of pulse pattern when the voltage reference is located between space vectors SV1 and SV2 for DPWMMIN.

is clearly ideal for a resistive load where the switch stop also occurs at the peak current. However, it is possible to center the switch stop anywhere within the 120° interval. If v_a is taken as an example, it is possible to place the 60° switch stop anywhere around **SV1** ($\pm \pi/3$). As a result, it is possible to move the switch stop period if the load is inductive in order to decrease the switching losses, i.e to move the switching stop to a position closer to where the current has its maximum. When the load is an IM it is clearly desirable to lag the switching stop by 30° . This ensures a switching stop as close to the maximum current as possible due to the power factor of an IM.

The current ripple, using the same assumption as for 5.3, for the different SVM methods can be expressed as

$$I_{abSVM}^2 = \frac{V_s^2}{4L_\sigma^2} \frac{\Delta T^2}{48} \left[\frac{3}{2} M^2 - \frac{4\sqrt{3}}{\pi} M^3 + \frac{9}{8} \left(\frac{3}{2} + \frac{9\sqrt{3}}{8\pi} \right) M^4 \right] \quad (5.10)$$

$$I_{abDPWMMIN}^2 = \frac{V_s^2}{4L_\sigma^2} \frac{\Delta T^2}{48} \left[6M^2 - \frac{35\sqrt{3}}{2\pi} M^3 + \left(\frac{27}{8} + \frac{81\sqrt{3}}{64\pi} \right) M^4 \right] \quad (5.11)$$

$$I_{abDPWM60}^2 = \frac{V_s^2}{4L_\sigma^2} \frac{\Delta T^2}{48} \left[6M^2 - \left(\frac{45}{2\pi} + \frac{4\sqrt{3}}{\pi} \right) M^3 + \left(\frac{27}{8} + \frac{27\sqrt{3}}{32\pi} \right) M^4 \right]. \quad (5.12)$$

The current ripple of the DPWMMIN, DPWMMAX and DPWM30lag are identical. Figure 5.18 shows the current ripple magnitude of the different PWM schemes as a function of the modulation index M . Note that the constant term is equal in each expression and therefore removed.

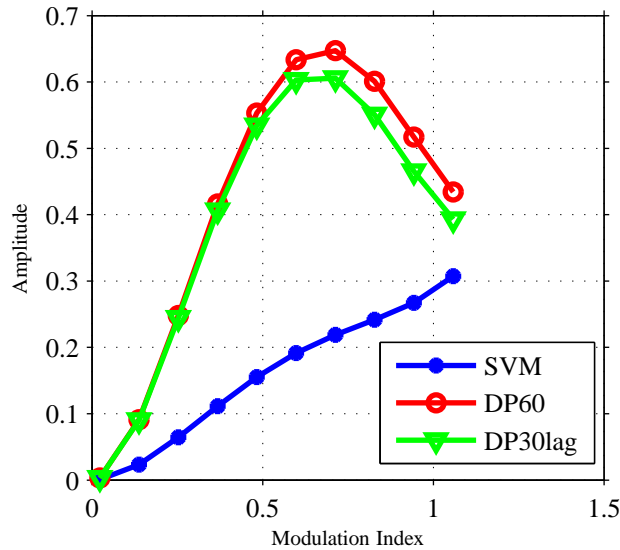


Fig. 5.18 Calculated current ripple for different PWM schemes.

5.3.4 Theoretical comparison of different PWM schemes

A Simulink model of a 4kW IM loaded with $T=b\omega^2$ has been simulated using different SVM techniques. In order to compare the switching losses it has been assumed that the switching loss at each switching transition is proportional to the current at that time. Furthermore, no loss contribution has been accounted for in the freewheeling diodes. The switch loss component for the different techniques has been calculated as, using SVM as a reference

$$P_{sw\%} = \frac{\sum_{i=1}^{n_1} I_{ix}}{\sum_{i=1}^{n_2} I_{iSVM}} \quad (5.13)$$

where I_{ix} is the current through the transistor at the i^{th} switching instant, n_1 and n_2 are the number of switching instants during one period of the fundamental and x refers to the technique.

Figure 5.19 shows the relation between the different techniques normalized to SVM, which has been chosen as a reference. Figure 5.20 shows the switch loss relation normalized to the maximum loss of SVM. It can be noted that DP30lag has the lowest losses, as expected. The decrease in the switching losses becomes higher at higher load due to the increased power factor which results in a switch stop closer and closer to the maximum current amplitude.

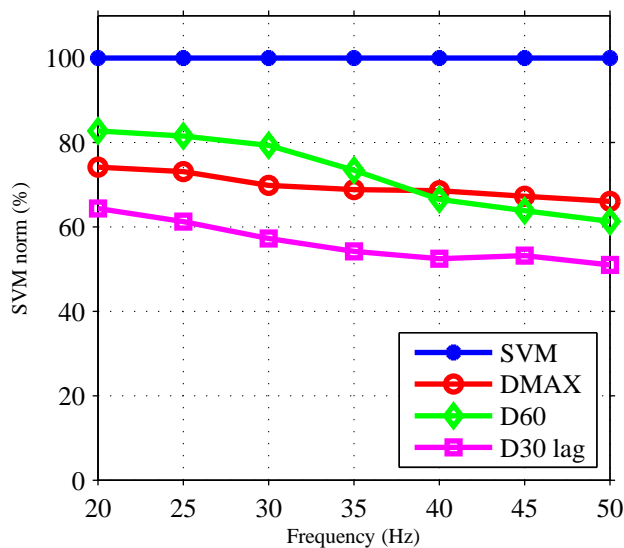


Fig. 5.19 Calculated switching losses, normalized to the SVM at each operating point.

The losses due to harmonics presented in figure 5.18 were not possible to reproduce in the simulations, and will be a topic for future work.

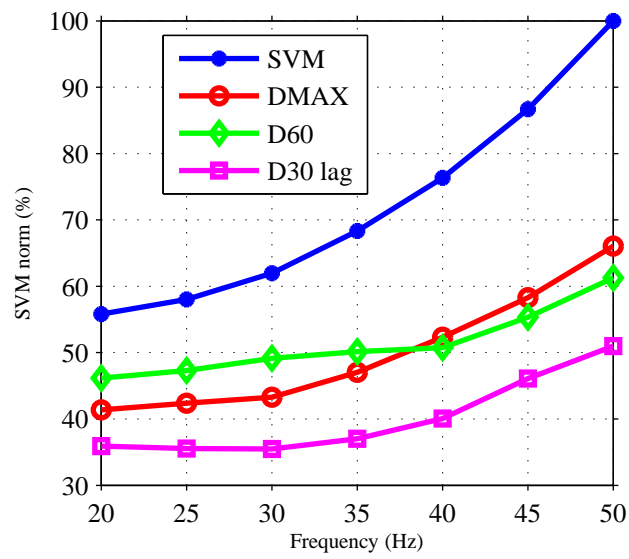


Fig. 5.20 Calculated switching losses, normalized to the SVM loss component at 100%.

Chapter 6

Efficiency determination of different permanent magnet motor drive systems

The efficiency of a PM motor can be affected using different control strategies, different PM motor topologies and different motor designs. This chapter will to a great extent be based on the design of a couple of commercially available PM motors. Focus will be placed on modeling of the loss components in the drive system and comparison between different control schemes. The result will be compared to measurement presented in Chapter 9 and used for evaluation of the potential savings in HVAC applications in Chapter 10

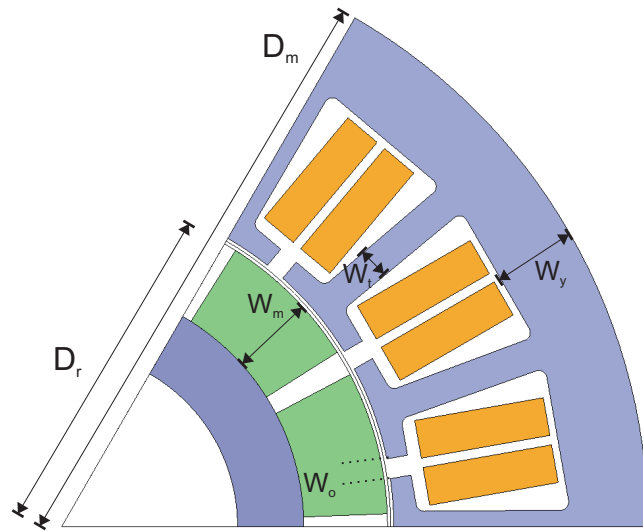
6.1 Model setup of a 375W BLDC motor in Maxwell/Simplorer

Chapter 3 described the modeling procedure in Maxwell/Simplorer which now is applied on a 375W 1000rpm BLDC motor, used in fan applications. It should be noted that the purpose of the modeling is to estimate the loss components of a PM drive system with sufficient accuracy in order to compare different control strategies, motor technologies and motor designs. Hence, the absolute accuracy is not as important as the relative accuracy/trend.

6.1.1 Setup of the 375W BLDC motor in Maxwell

The physical dimensions of the motor are obtained from detailed measurements of the stator and rotor. Figure 6.1 shows a 2D drawing of the motor, where the motor length is 38mm. The magnets are known to be of the type Ceramic 8, having a remanence, B_r of 0.43T. The iron assumed to be of the type M800-65A, where 800 stands for the maximum loss per kg at 1.5T and 50Hz, (8W/kg), and 65 stands for the thickness of the lamination, 0.65mm. The basic design are set in the Maxwell tool RMexp where all the dimensions

and material properties are defined. After creating a FEM model in Maxwell the following settings are changed in order to improve the accuracy of the result:



$$\begin{aligned} \underline{W}_y &= 8.5\text{mm} & D_r &= 38.5\text{mm} & D_m &= 77\text{mm} \\ W_g &= 0.75\text{mm} & W_m &= 10\text{mm} & W_t &= 3.8\text{mm} \\ W_o &= 2.7\text{mm} & & & & \text{magnet embrace } 85\% \end{aligned}$$

Fig. 6.1 Cross section of the 375W BLDC motor, where the length is 38mm.

1. The rotor set angle δ_{set} is a value that determines at which relative rotor position change the software should update the rotor movement. Hence, a smaller value increases the accuracy of the solver but increases the simulation time. The value is reduced from its default value 2.5 degrees to 0.6 degrees. Reducing this value further has no big influence on the result, (less than 0.1%). By reducing the angle the mesh in the airgap is automatically improved which also increases the accuracy of the result.
2. Increasing the number of mesh elements in the stator with a factor of two. This makes the calculation of the iron losses and torque more accurate, more elements makes no big difference (less than 0.1%).
3. Include iron loss calculation in the stator core. The iron losses in the rotor for this motor was found to be negligible and are neglected ($<1\text{W}$)
4. The nonlinear residual is decreased from its default value 10^{-4} to 10^{-6} increasing the accuracy due to nonlinearities in the iron core, at the cost of longer simulation time. Smaller value gives identical results.

The final mesh for the 1/6 symmetry sector consists of approximately 4000 elements.

6.1.2 Frequency converter setup in Simplorer

The FEM model in Maxwell is connected to the circuit program Simplorer in order to include the effects of the switched voltage supply which will have a large impact on the iron losses which will be exemplified in 6.1.3.

Since two phases are active at the same time for a BLDC motor, only one phase current is controlled at each time instant. In this case the positive current is controlled whereas the lower transistor in the negative current phase are left at its on-state. The current is compared to its reference value and switches when the current is above or under the reference value. Figure 6.2 shows an example of the inverter operation when phase A and C are active and when the current is positive in phase A.

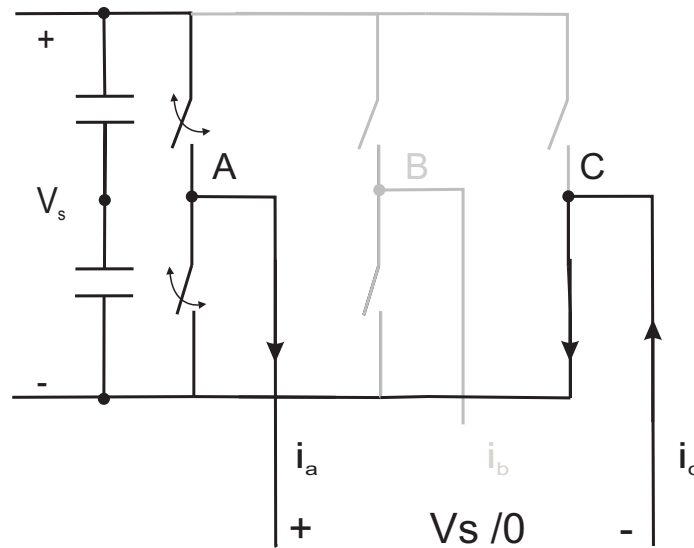


Fig. 6.2 Example of the inverter operation when the current reference in phase A is positive, current in phase B is zero and the current is negative in phase C.

The converter setup are based on the configuration used in the laboratory setup that will be presented in Chapter 9. The converter will use a constant DC supply of 300V. The current is sampled at 20kHz, resulting in a maximum switching frequency of 10kHz.

The transistors and diodes consists of system level components, meaning that they are on or off, neglecting the switching transitions. The voltage drop when the devices are at its on-state, are accounted for. The IGBT module FS10R06VE3 is used for the loss calculations, where the on-state voltage drop as a function of the current is obtained from the data sheet. The switching loss component is calculated by identifying each switching transition and the switched current at the switching instant. The energy dissipated at the given current are then obtained using the loss curves obtained in the data sheet, using the typical condition, assuming a junction temperature of 125°. It should be pointed out that

the loss data presented in the data sheet corresponds to a DC bus voltage of 300V. Hence, the loss curves were used directly without any modifications.

One problem with FEM calculations together with power electronic simulations is that the difference in time constant between the different systems are extremely large. The power electronic circuit needs a relatively small time step (μs) and the mechanical system, in this case, needs approximately 500-600ms to reach steady state. As a result, the simulation time becomes extremely long. In order to overcome the mechanical time constant a constant speed source is used, where the speed is updated based on the calculated electromechanical torque and known load profile. The average torque is calculated after one electrical period, and the speed is updated. This iteration continues until there is no change in speed. As a result, instead of simulating for 500-600ms it is now possible to obtain the same result during 3-4 electrical periods, reducing the simulation time substantially. It should be noted that, in order to simulate for only three or four electrical periods, a good initial guess of the mechanical speed needs to be done otherwise more electrical periods are needed.

6.1.3 Iron loss calculation

Section 3.2.2 described how the iron losses are calculated in Maxwell. The big advantage by using a Simplorer Maxwell co-simulation is the ability to take into account the switched voltage supply. By neglecting the current ripple, using an ideal current source, large errors can be introduced, underestimating the iron losses. This is due to the iron losses that arise from the harmonics in the magnetic flux density, caused namely from the current ripple. As an example, the BLDC motor was simulated using a sinusoidal current waveform, both with an ideal sinusoidal current source and with the converter supply. The motor was connected to a speed dependent load, $T=b\omega$, loading the motor with 375W at 100%. Figure 6.3 shows the difference when the motor is fed by a converter compared to the ideal case. It can be noted that the iron loss calculation differs substantially, especially at low speed/load due to the relatively large current ripple at low speed. As a result, by including the iron losses due to the current ripple a much more accurate estimate of the iron losses is obtained.

It should also be noted that the calculation of the iron losses by default are a post processing calculation in Maxwell.

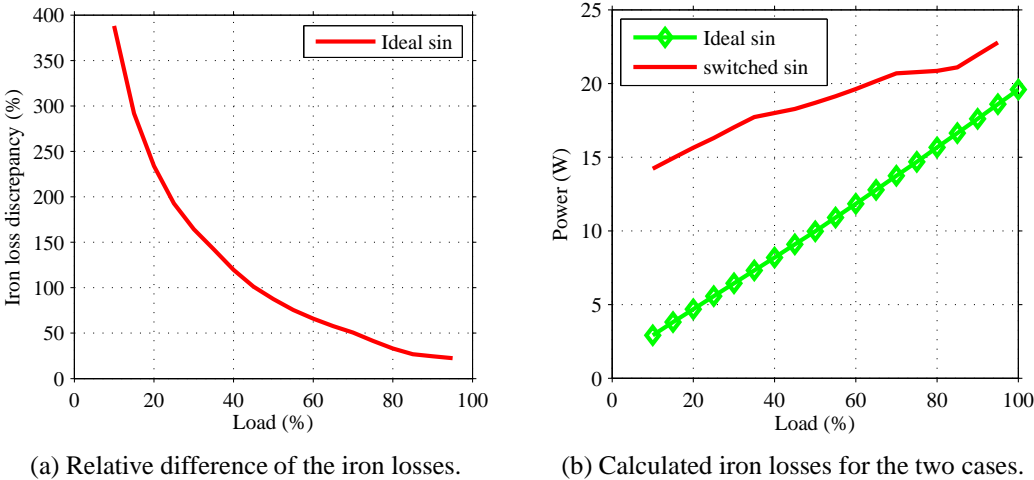


Fig. 6.3 Calculated difference in iron losses when the motor is operated with converter supply and a pure sinusoidal current supply for a speed depended load, $T=b\omega$, where 100% corresponds to rated operation of 375W

6.2 Simulation result

The motor was first operated at no load in order to obtain the induced voltage in the windings, presented in figure 6.4. The motor was then connected to a linear load having its rated operation at 1000rpm. The stator resistance was in this case calculated to be 5.4 Ω , corresponding to a temperature of 50°C. The friction losses was defined as

$$P_{fric} = b_f w_r^2 \quad (6.1)$$

where b_f was calculated to obtain a friction loss of 5W at 1000rpm in accordance with the bearing manufacturer.

6.2.1 Motor commutation

The phase currents during 20ms of the motor operation are shown in figure 6.27, together with its reference value of 1A. It can be noted that the behavior is as expected. When the current is lower than the current reference magnitude, the upper switch in the active positive phase is turned on, applying the DC-grid voltage V_s across the two active phases, as explained in Section 6.1.2. The current is now increasing and when the current measurement is updated, the current has reached above its reference and the upper switch is turned off and the lower switch is turned on supplying the motor with 0V. The current is now decreasing slowly down until it falls below its reference value and the procedure repeats itself. The average current during one switching cycle is evidently higher than the reference current. However, it is of less importance since at least one outer control loop, eg. speed control or airflow control, is used in an pump/fan application which will provide the correct operating point. An alternative would be to switch both inverter legs on and off supplying the active motor phases with $+V_s$ when the current are to be increased and $-V_s$ when the current are to be decreased. This will result in a current ripple evenly distributed on each sides of the current reference giving a more correct current value. However, the cost will be an increased amount of switching instants increasing the switching losses in the inverter.

It should also be noted that the actual switching frequency is fairly low, in this case approximately 4.9kHz. It can be increased by simply increasing the update frequency of the current measurement. However, due to limitations in the laboratory setup this setting will be used. Section 6.3.8 will give a simulation example on how the updating frequency is affecting the efficiency of the drive system.

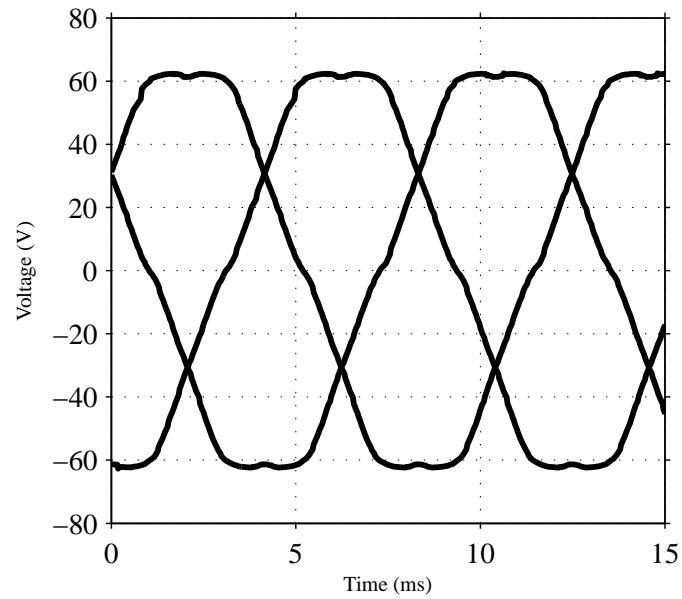


Fig. 6.4 Induced voltage in the stator windings at 80Hz.

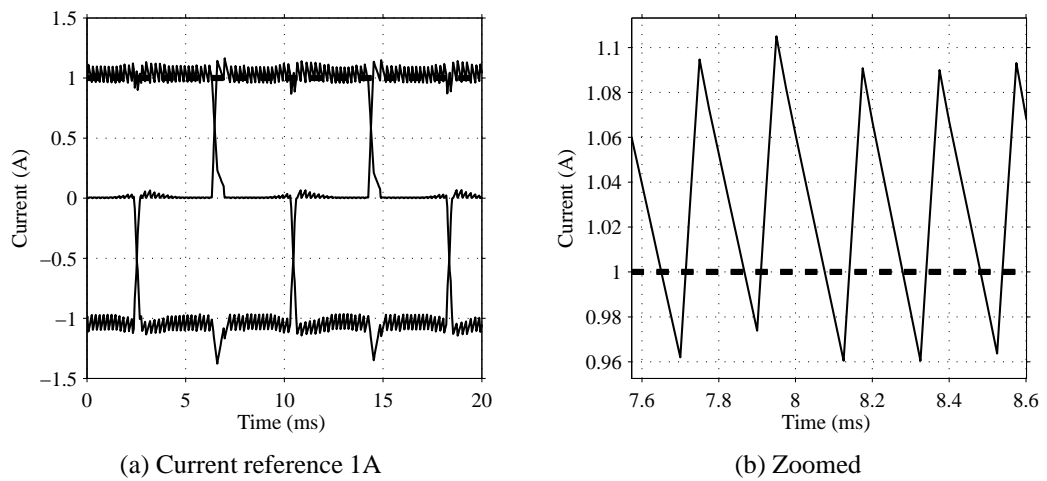


Fig. 6.5 Phase currents of the BLDC motor having a current reference of 1A.

6.2.2 Calculated quantities

Figure 6.6 shows the efficiency of the motor. It can be noted that the efficiency of the motor drops at higher load. This can partially be explained by observing the iron and stator losses shown in figure 6.7. Since the motor is designed with relatively small amount of stator iron due to the relatively low magnetic flux density provided by ceramic magnets, the iron losses are relatively low and the number of stator turns are relatively high. Hence, at low load/speed when the current is low the efficiency is high. As the speed/load increases the stator losses becomes dominant which in turn reduces the efficiency. Another reason for the drop in efficiency at higher speed is the reduced controllability of the current. Since the DC voltage is kept constant at 300V, the controllability is reduced when the speed is increased. Figure 6.8 shows the torque as a function of RMS current. It can be noted that the characteristic is close to linear expect for the higher loads where more RMS current is needed to produce slightly higher torque. This will be discussed in more detail in Section 6.3.5.

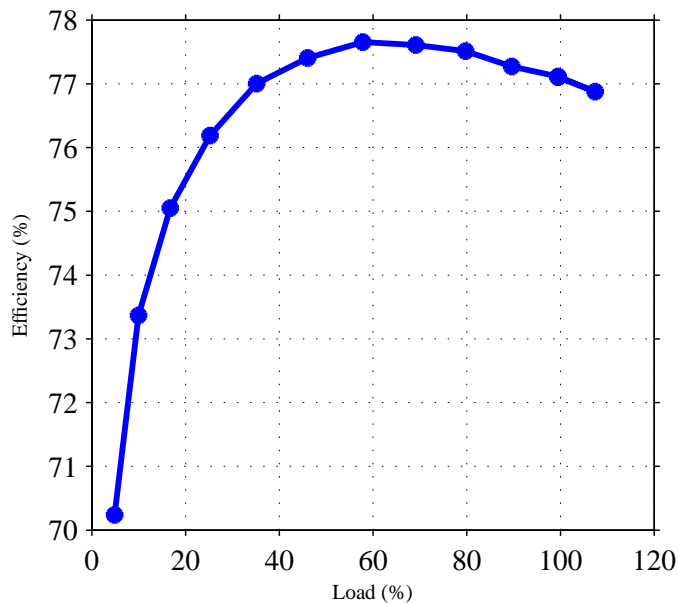


Fig. 6.6 Calculated efficiency of the 375W BLDC motor connected to a linear load where 100% corresponds to its rated operation.

It should also be noted that the efficiency is slightly overestimated due to the postprocessing calculation of the iron losses. As a result, the calculated electromagnetical torque produced by the motor is overestimated. It is not straight forward to take this into account due to the complex nature of the iron losses. One part of the losses arise from the current ripple, especially at light load where the current ripple is high. Hence, it will not be correct to subtract the torque corresponding to the total iron loss component. A new feature is available in Maxwell, taking this into account. However, the cost in simulation time and

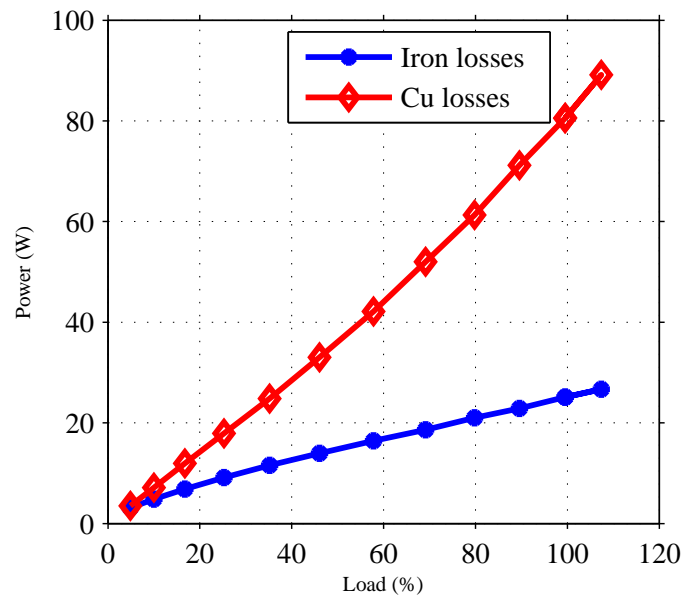


Fig. 6.7 Calculated iron and copper losses of the 375W BLDC motor connected to a linear load where 100% corresponds to its rated operation.

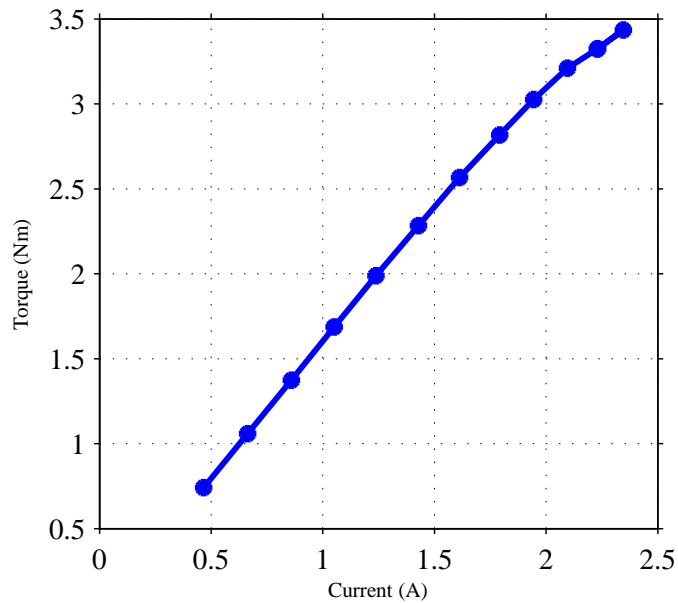


Fig. 6.8 Calculated torque as a function of RMS current of the 375W BLDC motor connected to a linear load.

solver stability is highly affected.

The losses in the converter stage was also calculated as described in Section 6.1.2. Figure 6.9 shows the switching and conductive losses of the inverter stage. The result shows that the switching losses decreases at higher load, despite of an increase in load current. This is due to the fact that the number of switching instants decreases due to the increased back emf in the motor at higher speed.

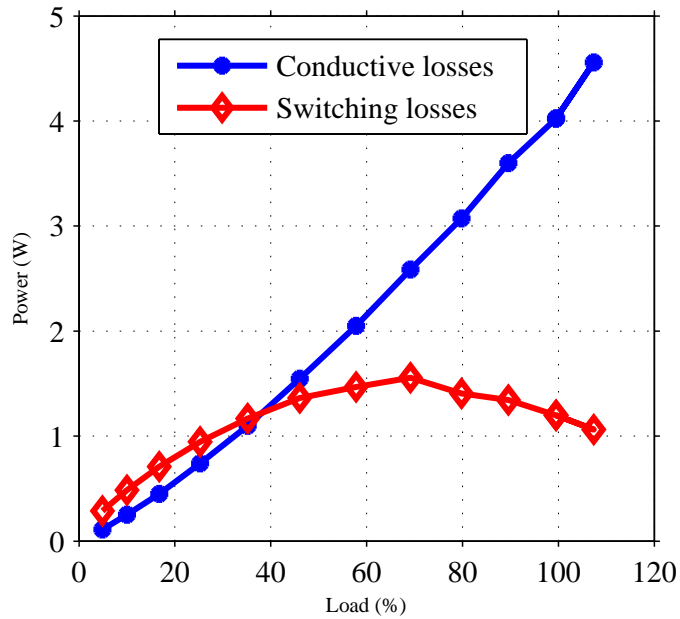


Fig. 6.9 Calculated switching and conductive losses for the BLDC inverter stage when the motor is connected to a linear load.

6.3 Efficiency comparison between different control schemes

This section will describe and analyze different sinusoidal current control schemes tested on the 375W BLDC motor and for a given 4kW PMSM. It will also provide a comparison between the BLDC control and a modified BLDC control.

6.3.1 Advanced angle BLDC control

In order to reduce the problem with phase commutation at higher speeds [50], resulting in current drop and as a result lower torque/current ratio, the classical BLDC control can be modified by changing at which rotor position angle that the phase commutation occurs. This is illustrated in figure 6.10, showing the induced voltage and two different current references. Current reference A shows the original position of the current reference, namely centered around the induced voltage. Current reference B are shifted with a certain angle in order to increase the controllability of the current due to the lower induced voltage at the time of activation. As a result the time derivative of the current will increase resulting in a faster current commutation and hence a lower drop in the current amplitude.

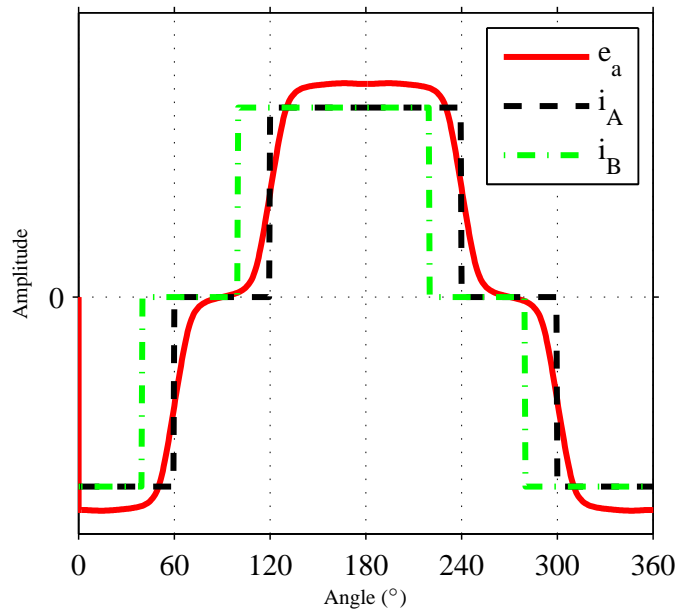


Fig. 6.10 Induced voltage and two different current references one in phase and one shifted relative to the induced voltage.

6.3.2 Field Oriented Control

A commonly used current control strategy is field oriented control (FOC), where the currents are transformed to the dq-system and oriented along the rotor flux component in

order to decouple the control of the torque and flux respectively. Hence, the torque is easily controlled provided knowledge of the motor parameters, including back emf and perform well in a high dynamic performance drives. Carrier based PWM or SVM are common modulator solutions [51], [52]. In order to utilize the DC bus voltage, a SVM strategy or a modified carrier wave strategy should be used, in the same manner as for the IM described in Chapter 5. A schematic figure of the control scheme is shown in figure 6.11. This control scheme needs good knowledge of the motor parameters, coordinate transformation, two PI current controllers (i_d and i_q) and carrier wave comparison. The relatively high complexity compared to the later purposed control schemes also introduce modeling issues. Since the control scheme needs carrier wave comparison or SVM calculations, and has a relatively low torque response, a small time step and a long simulation time is needed in order to reach steady state. As a result, the FEM calculations will cause simulation issues due to the simulation time. However, the control scheme will be implemented on a 4kW PMSM and tested for a single case.

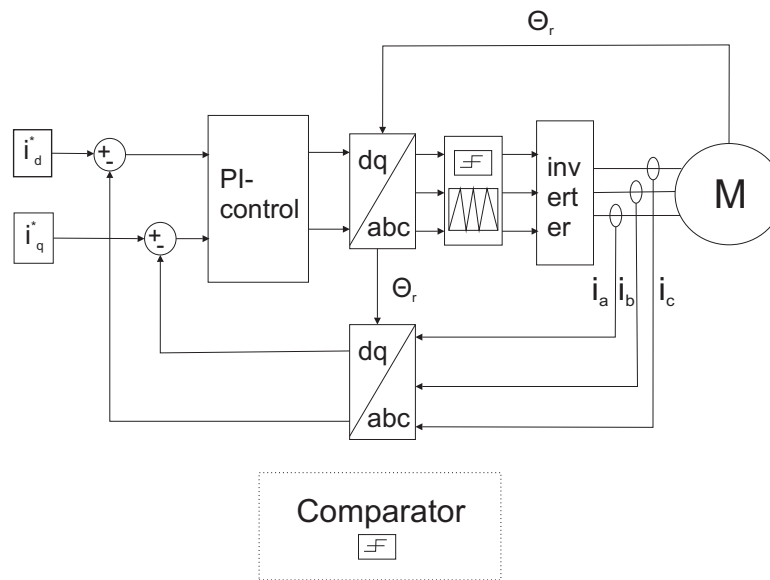


Fig. 6.11 Control system

6.3.3 Basic hysteresis control

It is interesting to investigate a simple control strategy that can be of interest for small motor drives where the cost and complexity of the controller has a big influence of the choice of controller. The simplest case is to control the current in each phase by comparing the measured current with the sinusoidal current reference and change the state of the transistors in each inverter leg individually, without taking the other phase legs into count. The control strategy can be summarized as follows

Case A. If $i_x^*(t_1) > i_x(t_1)$

Case B. If $i_x^*(t_1) < i_x(t_1)$

where $i_x^*(t_1)$ and $i_x(t_1)$ are the current reference and the measured current in phase x respectively at the time instant t_1 . If case A is fulfilled the upper transistors will be turned on and the lower turned off and for case B the opposite will occur. The current references will be generated by using the rotor position angle. Figure 6.12 shows a schematic diagram of the control scheme.

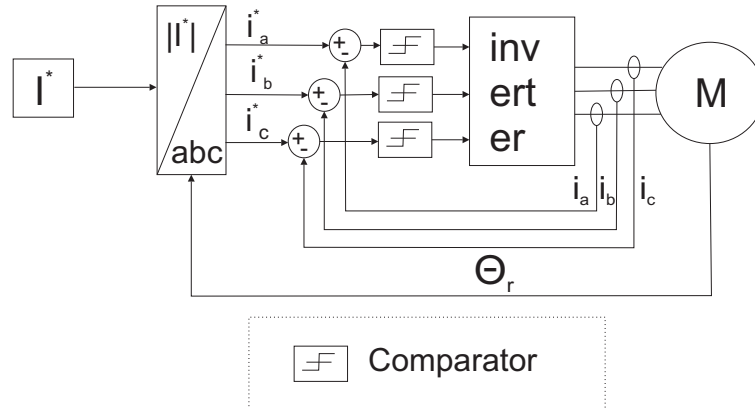


Fig. 6.12 Control system

The switching frequency will be dependent on the updating frequency of the current measurement and the hysteresis band of the current controller. The updating frequency will be set to 20kHz, same as for the BLDC current control. Furthermore, no hysteresis will be implemented due to the relatively low updating frequency of 20kHz which anyway will result in large current ripple at low speeds.

One major drawback with this simple control is of course the independent control of each phase. Furthermore, there is no strategy to generate zero-voltage vectors. This will be an efficiency problem especially at low speeds, low induced voltage, where high frequency switching will occur resulting in high losses in the inverter and motor [53].

6.3.4 Direct Torque/Current Control

Recent years, Direct torque control (DTC) have gain in popularity [54]. DTC was first developed for the IM [55], [56], but has also been implemented in PMSM [57]. The basic principle of DTC is that the torque and stator flux is estimated and compared with its reference, and at each time update a suitable space vector is activated, or remains activated, in order to as quickly as possible reach the reference value. The main difference between different DTC schemes are how to choose an appropriate voltage vector for each time update [54].

The basic control scheme is shown in figure 6.13.

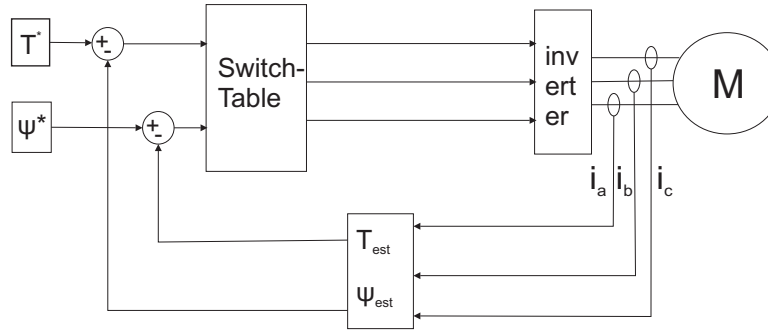


Fig. 6.13 Control system

The advantages compared to the FOC are fast torque response, possible elimination of PI controllers robustness to parameter changes in the motor and reduced switching losses in the inverter stage [54]. The main drawbacks are increased torque and flux ripple. Furthermore, the torque and flux needs to be estimated with a high frequency which in turn increases the demand of the processor.

The classic DTC will not be implemented in this thesis, but its simplicity and the possibility to have full control of the activation of the space vectors is still attractive from an energy efficiency point of view due to the possibility to reduce switching losses in the converter. Hence, instead of DTC, direct current control (DCC) will be implemented where the magnitude and angle of the current vector is controlled at each update of the current controller. Similar control schemes has been purposed in the literature, [58], [53]. The difference is, same as for the DTC, how to chose an appropriate voltage vector at each update of the current controller.

The DCC will be based on controlling the $i_{\alpha\beta}$ vector. Instead of controlling each inverter leg individually, the inverter is now controlled by choosing appropriate space vectors SV0-SV7, at each update of the current measurement, in order to obtain the desired current vector. As a result, it will be possible to reduce the number of switching transitions, mainly due to active choice of the zero space vectors, SV0 and SV7. Only the currents and the position of the motor needs to be known which simplifies the control compared to FOC.

The different possible scenarios for each current time sample are as follows, refer to figure 6.14 for the notations:

Case A. If $\|I_{\alpha\beta}\| < \|I_{\alpha\beta}^*\|$ and $\Theta_{i_{\alpha\beta}^*} > \Theta_{i_{\alpha\beta}}$

Case B. If $\|I_{\alpha\beta}\| < \|I_{\alpha\beta}^*\|$ and $\Theta_{i_{\alpha\beta}^*} < \Theta_{i_{\alpha\beta}}$

Case C. If $\|I_{\alpha\beta}\| > \|I_{\alpha\beta}^*\|$ and $\Theta_{i_{\alpha\beta}^*} - \Theta_{i_{\alpha\beta}} < \varphi_{ih}$

Case D. If $\|I_{\alpha\beta}\| > \|I_{\alpha\beta}^*\|$ and $\Theta_{i_{\alpha\beta}^*} - \Theta_{i_{\alpha\beta}} > \varphi_{ih}$.

where $I_{\alpha\beta}$ and $I_{\alpha\beta}^*$ are the calculated magnitude of the measured and reference current respectively, $\Theta_{i_{\alpha\beta}}$ and $\Theta_{i_{\alpha\beta}^*}$ are the angles of the measured and reference current respectively. It should be noted that no hysteresis is present in this case due to the relatively low updating frequency of 20kHz. For case C and D, φ_{ih} is introduced and are yet to be determined. The main principle is illustrated in figure 6.14, the current magnitude is lower and lagging the current reference (Case A). In this case, activation of the leading space vector SV2 will result in an increase of current magnitude and angle. If the current vector was leading the reference (Case B) SV1 would have been activated instead.

For case C, when the current magnitude is larger and not lagging the reference with more than φ_{ih} , SV0 or SV7 will be activated. The angle φ_{ih} is introduced since the difference between the current angle and its reference has a small rate of change during the zero vector activation. Hence similar control as for the current magnitude will only lead to an increased number of switchings without improving the motor control. The value of φ_{ih} are yet to be determined.

For case D, when the current magnitude is larger and lagging the current reference with more than φ_{ih} , the space vector that has the least influence on the current magnitude and most affect on the angle is activated, (ideally leading the current vector by 90°).

It should be pointed out that when the current vector comes closer to SV2, SV3 can be an option for increasing the magnitude and angle. In order to investigate the proper activation, the difference can be evaluated using the motor equations for a PMSM.

$$v_{\alpha\beta} = i_{\alpha\beta}R_s + \frac{di_{\alpha\beta}}{dt}L_s + e_{\alpha\beta} \quad (6.2)$$

where R_s is the stator resistance, L_s the motor inductance and $e_{\alpha\beta}$ is the induced voltage in the stator windings. The produced electromagnetical torque T_e can be expressed as

$$T_e = \frac{2n_p}{3}\Psi_m I_{\alpha\beta} \sin(\delta) \quad (6.3)$$

where Ψ_m and $I_{\alpha\beta}$ are the peak flux produced by the permanent magnets and peak current respectively and δ is the angle difference between the stator and rotor flux. From 6.3 it can be noted that the torque ripple will be directly proportional to the ripple of the current magnitude whereas the torque ripple caused by the angle ripple, Θ_{rip} , will vary with $\cos(\Theta_{rip})$.

The voltage vector $v_{\alpha\beta}$ is defined by the different possible states and can be assumed to have a fixed amplitude during a sample period. It is further assumed that the current reference and measured current are approximately equal, resulting in identical phase positions of $e_{\alpha\beta}$ and $i_{\alpha\beta}$. The impact on the current vector from a given voltage vector can then be evaluated by calculating the current derivative as a function of position of the

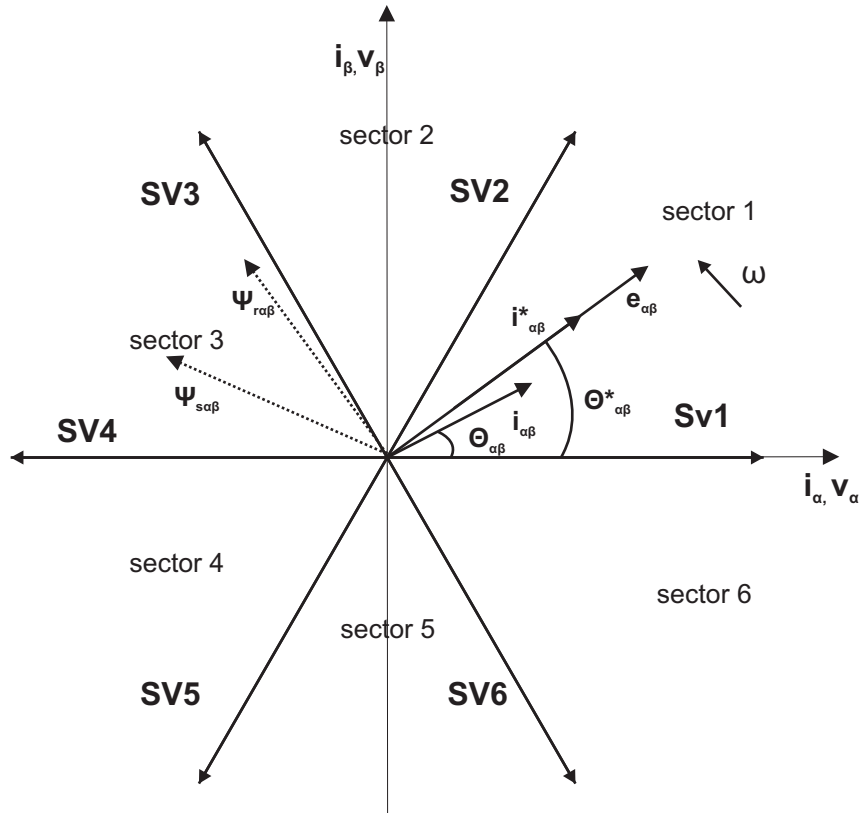


Fig. 6.14 Possible Space vectors for the different switching states together with the $\alpha\beta$ current reference and actual current at a time instant. SV0 and SV7 have zero magnitude and are left out in the figure.

current vector using (6.2). The parameters in the example are defined as, and are valid for the 4kW PMSM that will be analyzed later in this chapter,

$$R_s=1\Omega$$

$$L_s=34\text{mH}$$

$$V_s=540\text{V}$$

$$E=[0, 100, 200]\text{V (peak values)}$$

$$I=[1,10]\text{A (peak values).}$$

Impact on the current magnitude

Figure 6.15 shows the predicted difference in current magnitude during one sample interval of $50\mu\text{s}$, as a function of the relative position between the active voltage vector and the current vector for two current levels. The largest increase is evidently when the current vector is aligned with the voltage vector. The zero crossing of the current difference depends on both the induced voltage and load current and decreases for increased induced voltage and increased current magnitude. From this analysis it can be concluded that the angle difference between the voltage vectors and current vector should not exceed 70° if the current magnitude are to be increased.

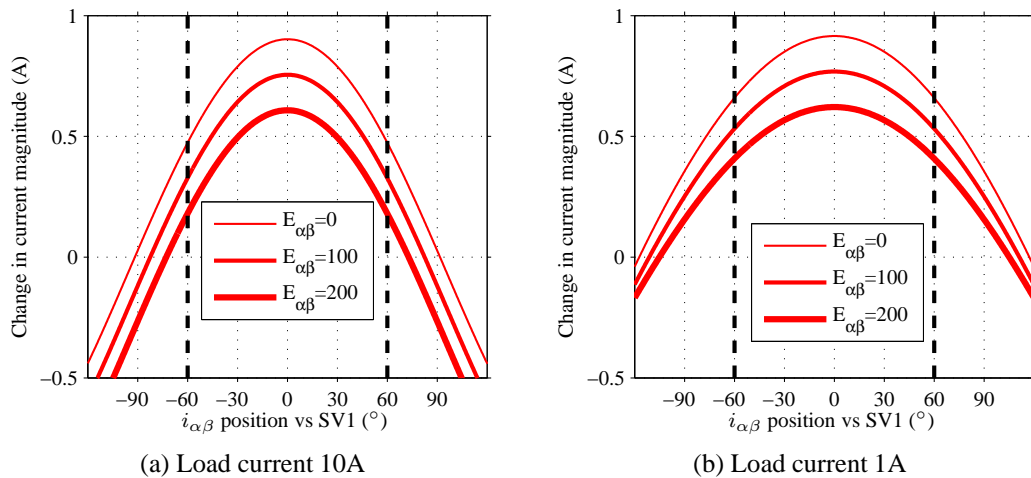


Fig. 6.15 Predicted current amplitude difference during one sample interval of $50\mu\text{s}$ for different positions of the current vector relative to the active voltage vector. The calculations are made for a fix current and for different magnitudes of the induced voltages.

Impact on the current angle position

The same calculations are made for the expected difference in current angle, shown in figure 6.16. It can be noted that the impact of the induced voltage is small whereas the current magnitude has a large impact on the angle derivative. It should be noted that the impact of a 10° angle difference will result in approximately 1.5% torque ripple according to (6.3).

$$\frac{dT_e}{d\delta} \sim \cos(\delta) = \cos(10^\circ) = 0.985 \quad (6.4)$$

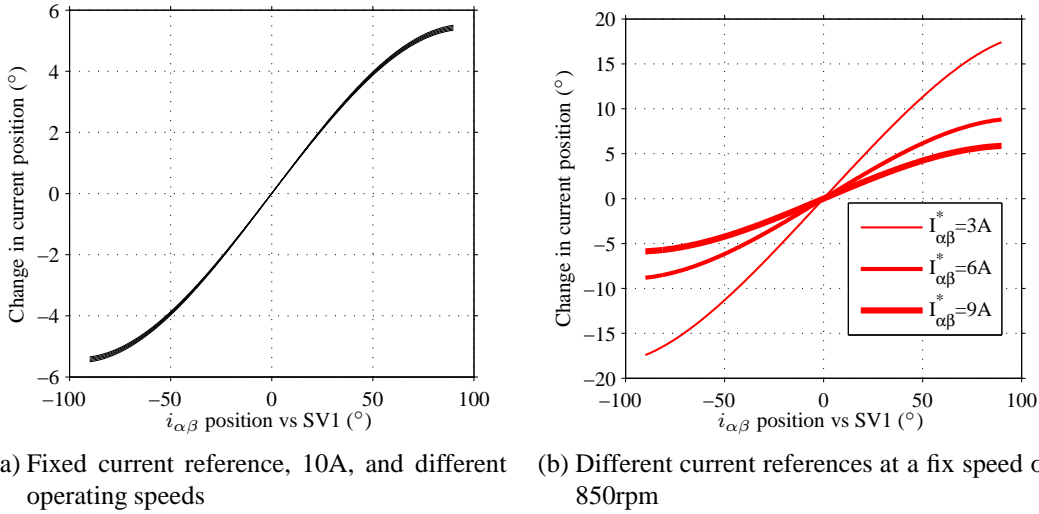


Fig. 6.16 Predicted $i_{\alpha\beta}$ position difference during one sample interval of $50\mu s$ for different positions of the current vector relative to the active voltage vector.

Sector activation

When the current and voltage vector are close, the predicted difference of the $i_{\alpha\beta}$ position is small, as shown in figure 6.16, which motivates activation of the following voltage vector. This is illustrated in figure 6.17, where the current reference are close to SV2, and activation of in this case SV3 might be a better choice than the activation of SV2.

Hence, it might not be a good choice to activate the first sector (SV1-SV2) for $0 < \Theta_{i_{\alpha\beta}^*} < 60^\circ$, and the sector activation will be defined as:

If $0^\circ - \varphi_{sv} < \Theta_{i_{\alpha\beta}^*} < 60^\circ - \varphi_{sv}$ activate sector 1

If $60^\circ - \varphi_{sv} < \Theta_{i_{\alpha\beta}^*} < 120^\circ - \varphi_{sv}$ activate sector 2

If $300^\circ - \varphi_{sv} < \Theta_{i_{\alpha\beta}^*} < 360^\circ - \varphi_{sv}$ activate sector 6

The value of φ_{sv} are yet to be determined but according to the analysis above, it should not exceed 10° for that particular motor since a larger value will lead to a decrease in the current vector at high load, (high speed and current). Hence the choice is limited to the interval $0^\circ - 10^\circ$ and will be evaluated for the motors tested.

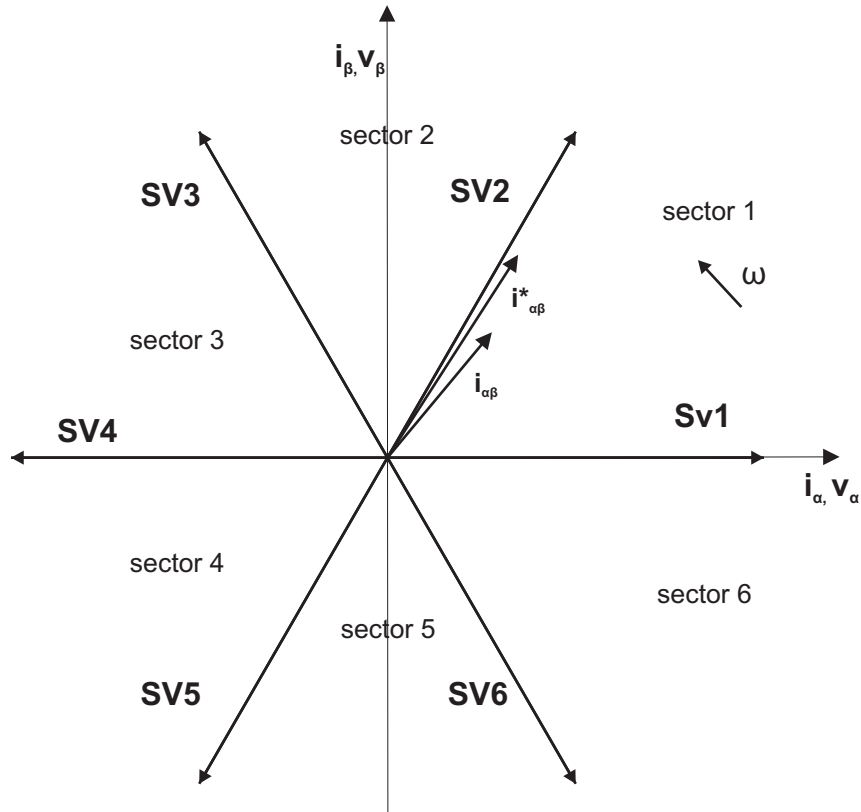


Fig. 6.17 Space vectors, $\alpha\beta$ current reference and actual current when the current vector is close to a SV2.

Zero vector selection

If the current magnitude is larger than its reference, SV0 or SV7 can be chosen. Other voltage vectors, leading or lagging the current reference with more than 90° can be activated in order to reduce the current magnitude. However, this will result in an increased switching frequency and higher stresses on the motor.

The criteria for which zero vector to activate still needs to be determined which will be the main focus when evaluating the control strategies. Different criteria are possible having different computational complexity. The vector resulting in the minimum numbers

of switchings can be chosen. Another criteria can be to leave the switch, having the highest current on and choose the appropriate zero vector. Both these cases are of course sub optimal choices but fairly easy to compute. A more complex strategy is to choose the zero vector that provides the lowest switching losses by estimating the switching loss at the time of the zero vector activation. This case can easily be implemented in the model but for real time operation of the motor the extra calculations might cause problems.

An additional aspect to take into account is the difference in conductive losses between SV0 and SV7 during the following sample period. Ideally, the zero vector that has the lowest switching losses and the lowest conductive losses during the next conductive period should be activated. This complicates the calculation even further and will be left out in this study.

Different control strategies

In total, four different sinusoidal current control schemes will be implemented and evaluated for the different motors, and will be referred to as:

ICP: individual control of the phase currents

SVI: space vector control of the current vector choosing the zero vector that leaves the switch with the highest current magnitude at its on-state during the zero vector activation

SVMSW: same as SVI but the zero vector that needs the lowest number of switches will be activated

SVML: same as SVI but the zero vector that results in the lowest switching losses will be activated, where the switching loss component for the two zero vectors are estimated at the time of activation.

Furthermore, the advanced angle BLDC control will be implemented on the 375W motor and FOC will be implemented on the 4kW PMSM for comparison.

6.3.5 PMSM vs BLDC control

It was stated in Section 2.2 that the theoretical current waveform should have the same harmonic content as the back emf in order to minimize the stator losses for a given output power. However, it was not clear from the theoretical analysis how the iron losses would be affected. Since, the a BLDC motor never has the ideal induced voltage that the classical BLDC current control is based on an alternative control can be to operate it as a PMSM.

The BLDC motor is now simulated with both the original BLDC current waveform and the different control schemes presented in section 6.3.

The motor is connected to a linear load, $T=b\omega$, where 100% load corresponds to the rated operation of the motor.

The different SV control schemes were evaluated in order to fine tune the controller and to determine φ_{sv} and φ_{ih} . After the evaluation $\varphi_{sv}=0^\circ$ where chosen, and was kept constant for convenience during the whole operating cycle. The worst case scenario was found to be an angle error of 10° , in general $\pm 5^\circ$. It was also observed that the error in angle was larger on the lagging side. As a result, an offset in the current angle was implemented for 2.5° on the leading side resulting in a later activation of the lagging voltage vector. The control of the current angle became necessary as expected, especially at lighter load and φ_{ih} was set to 5° . The modified control scheme will be implemented on all SVM schemes tested. It will further be used for the 4kW PMSM presented in Section 6.3.7 where φ_{sv} and φ_{ih} are open for adjustment, and a more detailed analysis of the purposed control scheme will be performed.

Figure 6.18 shows the efficiency of the different sinusoidal control schemes. As expected the highest efficiency is obtained when the inverter is controlled with SVML due to the decrease in switching losses, as can be found in figure 6.19. It is also clear that the SVML and SVMI are almost identical, showing that the lowest switching loss is obtained when the switch with the highest current is left on during the zero vector activation.

It is also interesting to evaluate the loss components in the motor which can be expected to differ due to the change in harmonic content in the current. Figure 6.20 shows the efficiency of the motor and it can be noted that the difference is significant, especially at light load where the efficiency for the ICP control drops. This can be explained by observing the iron losses presented in figure 6.21. It can be noted that the difference at light load is substantial, eg, approximately 56% lower for the SVML case compared to the ICP at 20% load operation. The difference between SVML and SVMI continues to be negligible which simplifies the control due to the increased complexity for when the SVML is used. The reason for the difference in iron losses is the different harmonic content in the current as can be seen in figure 6.22, showing the harmonic content in the current for ICP and SVML at 0.75A reference current.

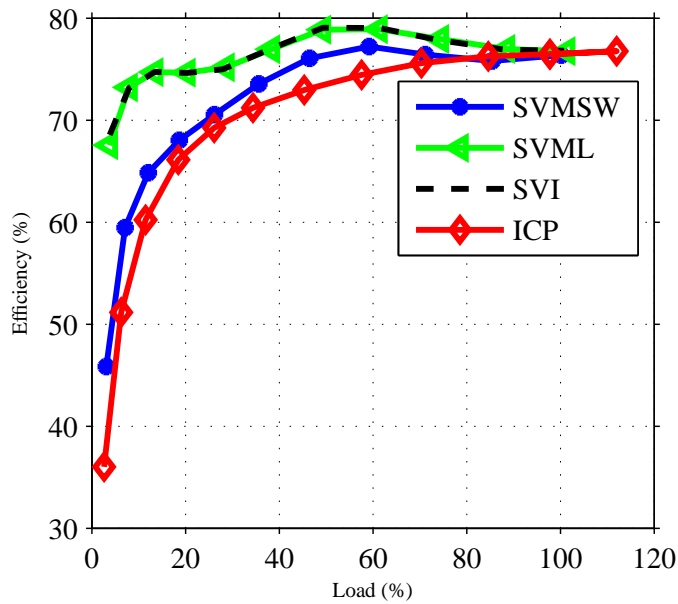


Fig. 6.18 Calculated efficiency, including the losses in the inverter stage, for the different sinusoidal current control schemes feeding the 375W BLDC motor. The motor is connected to a speed dependent load, $T=b\omega$.

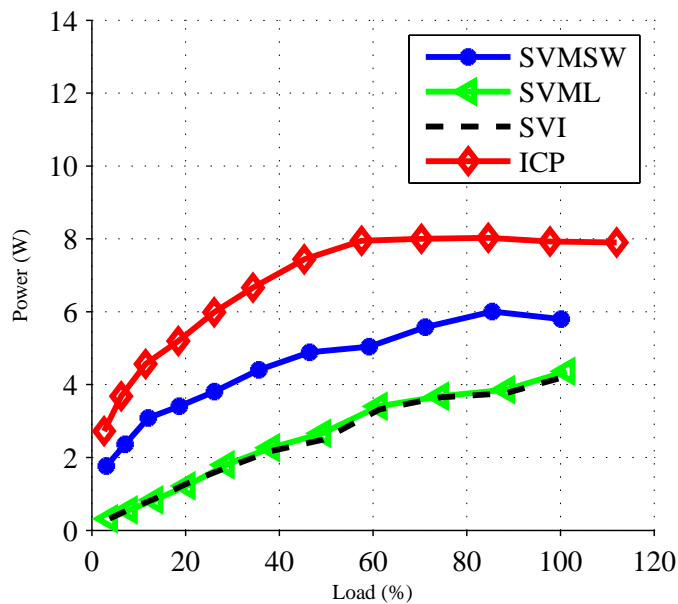


Fig. 6.19 Calculated switching losses for the different control schemes of the 375W BLDC motor. The motor is connected to a speed dependent load, $T=b\omega$.

6.3. Efficiency comparison between different control schemes

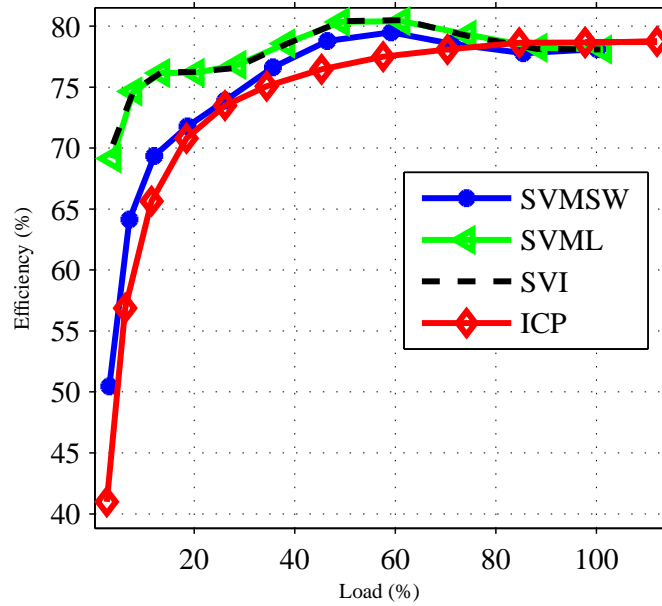


Fig. 6.20 Calculated motor efficiency for the different sinusoidal control schemes of the 375W BLDC motor. The motor is connected to a speed dependent load, $T=b\omega$.

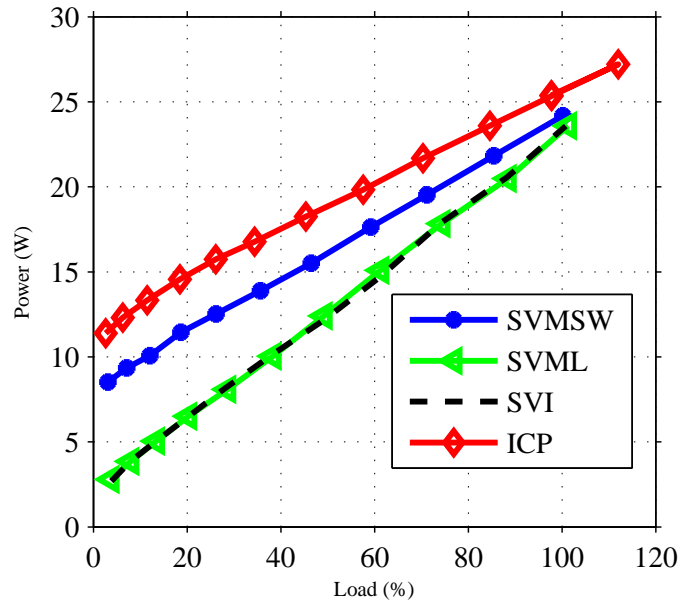


Fig. 6.21 Calculated core losses for the different sinusoidal control schemes of the 375W BLDC motor. The motor is connected to a speed dependent load, $T=b\omega$.

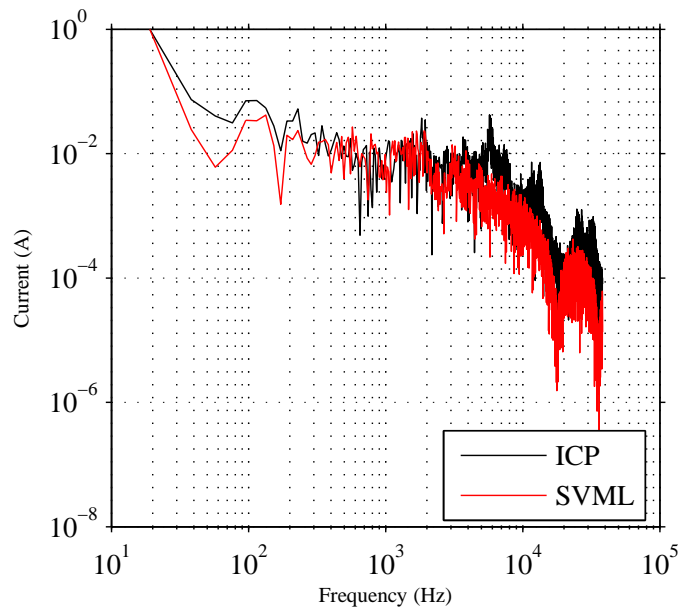


Fig. 6.22 Calculated frequency content of the current for ICP and SVMML at a reference current of 0.75A The motor is connected to a speed dependent load, $T=b\omega$.

6.3. Efficiency comparison between different control schemes

Figure 6.23 shows the efficiency of the motor when operated as a BLDC motor together with the ICP and SVM control. It can be noted that the efficiency of the motor is higher when operated as a BLDC motor at light load. When the load increases the efficiency of SVM and ICP control increases reaching 2% higher at rated load for the ICP case. The main reason for the higher efficiency at lighter load arise from the fact that the iron losses are much lower when operated as a BLDC motor. This can be seen in figure 6.24 which shows the iron losses for the same load situation.

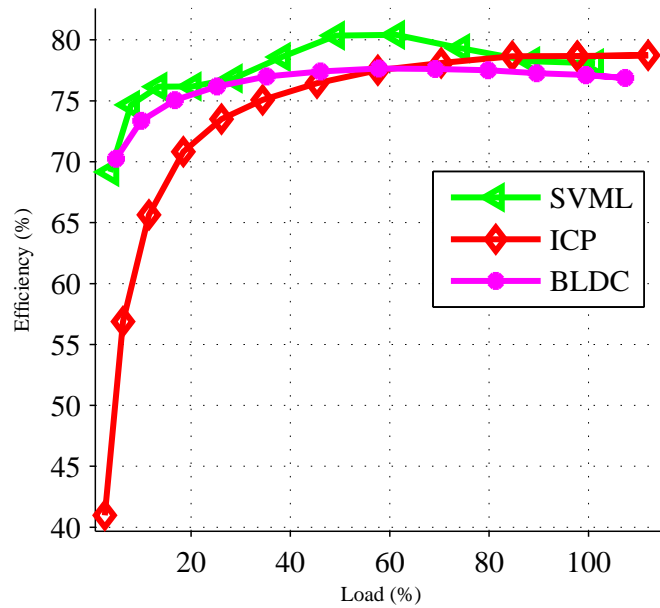


Fig. 6.23 Calculated efficiency of the 375W BLDC motor, without including the losses in the inverter stage, when operated with BLDC current waveforms and sinusoidal current waveforms. The motor is connected to a speed dependent load, $T=b\omega$.

When the speed increases, the controllability of the current is reduced since the induced voltage are increased whereas the DC link voltage are kept constant, as was pointed out in Section 6.2.2. Hence, the ability of the controller to produce the desired current waveform at rated operation is limited in the BLDC case. An example of the current waveform can be seen in figure 6.27 which shows one phase currents for two different operating points. In the low speed case the current follows the reference as expected. In the other case the motor is operated at rated operation and it is clear that the current now are deviating more from its reference value, especially during the phase commutations. This is the main reason for the drop in efficiency, since the RMS current needs to be increased in order to obtain the desired torque. This will not be the case for the sinusoidal commutation due to the continuous current flow in the windings. This result can be confirmed by increasing the number of turns in the stator winding. Figure 6.25 shows the efficiency of the original BLDC design operated as a BLDC motor and when the number of turns are

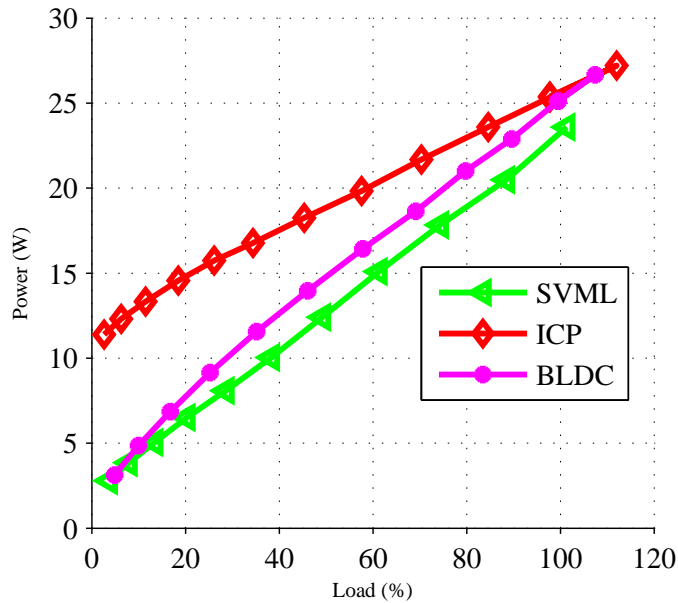


Fig. 6.24 Calculated iron losses of the 375W BLDC motor when operated with BLDC current waveforms and ICP and SVML control. The motor is connected to a speed dependent load, $T=b\omega$.

increased with 10%. Ideally this should not affect the efficiency of the motor. Keeping the NI and the conducive copper area constant ideally results in the same resistive and iron losses. However, since the back emf now is approximately 10% higher the controllability of the phase currents has decreased compared with the original motor design resulting in higher resistive losses close to rated speed. It can also be noted that the efficiency at lighter load is increased slightly due to the increased number of turns. This can be explained by the iron losses that has decreased slightly due to the decrease in the current ripple. The difference in motor efficiency between the BLDC and the sinusoidal control schemes is now expected to increase which is the case as can be seen in figure 6.26, showing the ICP and BLDC case, where the difference is 3.5% compared to 2% for the original case.

It should be noted that it is not straight forward to declare which control strategy that is optimal from an energy efficiency point of view. In this particular case it is evident that the motor should be operated with SVML in the whole operating region, or BLDC at light load and ICP at high load. This is an important result that will be given special attention in Chapter 7.

An interesting question now arise, can a PMSM improve its efficiency by changing the current control at light load to a BLDC control in order to reduce the iron losses? This will be investigated further in the next section, 6.3.7.

It is also important to take into account the losses in the inverter stage. Figure 6.29 shows the switching and conducive losses when the motor is operated as a BLDC, ICP and SVML. It can be noted that both the switching and conducive losses are higher in the

6.3. Efficiency comparison between different control schemes

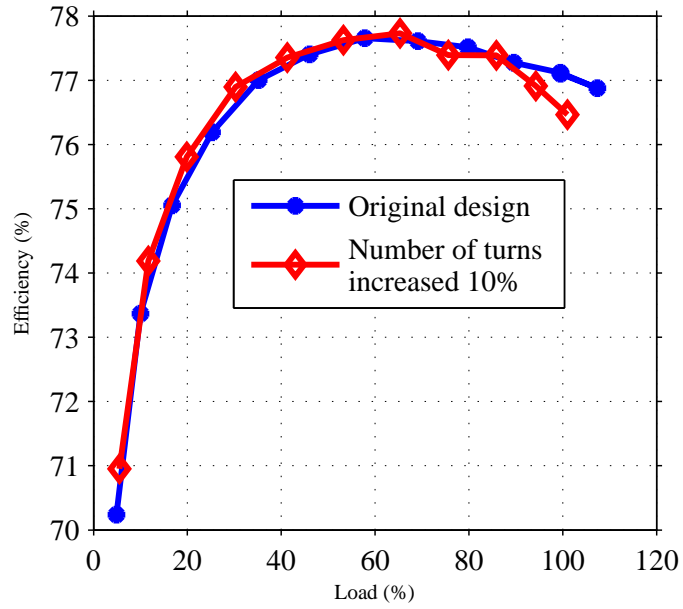


Fig. 6.25 Calculated motor efficiency of the 375W BLDC motor when operated with BLDC current waveforms, having 134 turns and 148 turns in the stator windings.

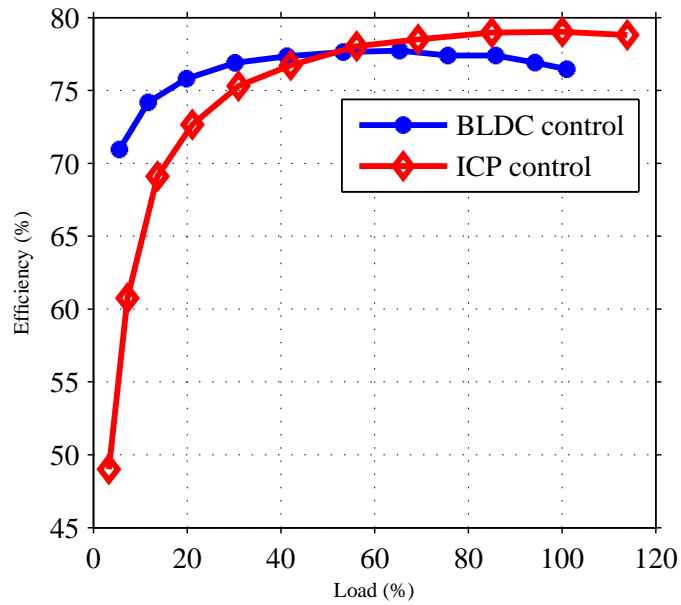


Fig. 6.26 Calculated motor efficiency of the 375W BLDC motor with 148 turns in the stator winding, when operated with BLDC and ICP control.

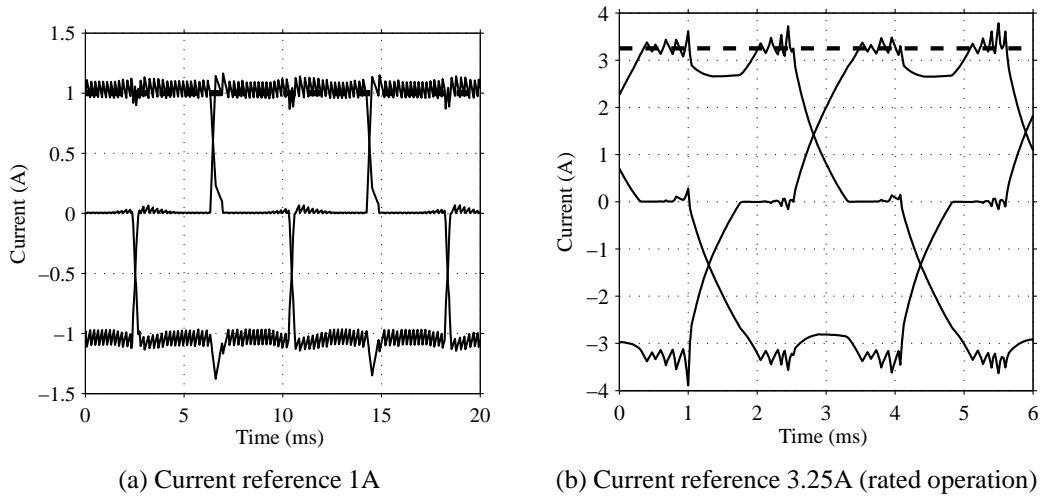


Fig. 6.27 Example of phase currents of the BLDC motor operated at two different speeds, when connected to a linear load $T=b\omega$.

PMSM case.

The total efficiency, including the losses in the inverter stage are shown in figure 6.28, for the original motor having 134 turns in the stator winding, showing that the difference is reduced slightly due to the increased losses in the inverter stage.

6.3. Efficiency comparison between different control schemes

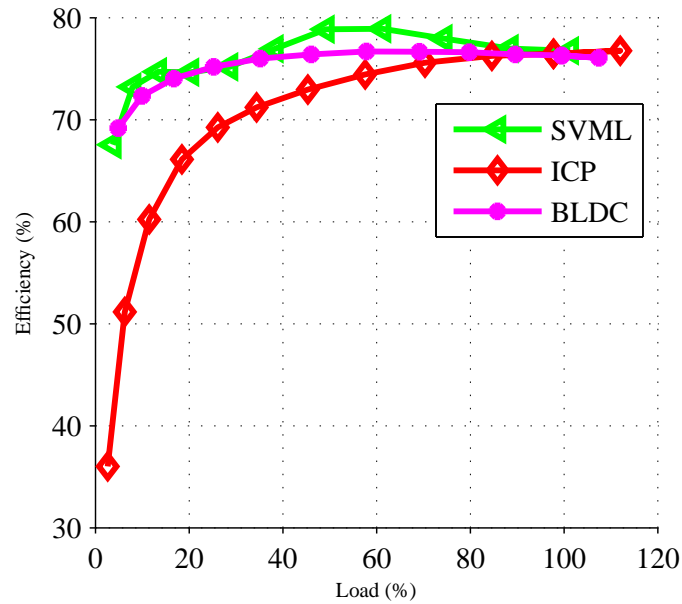
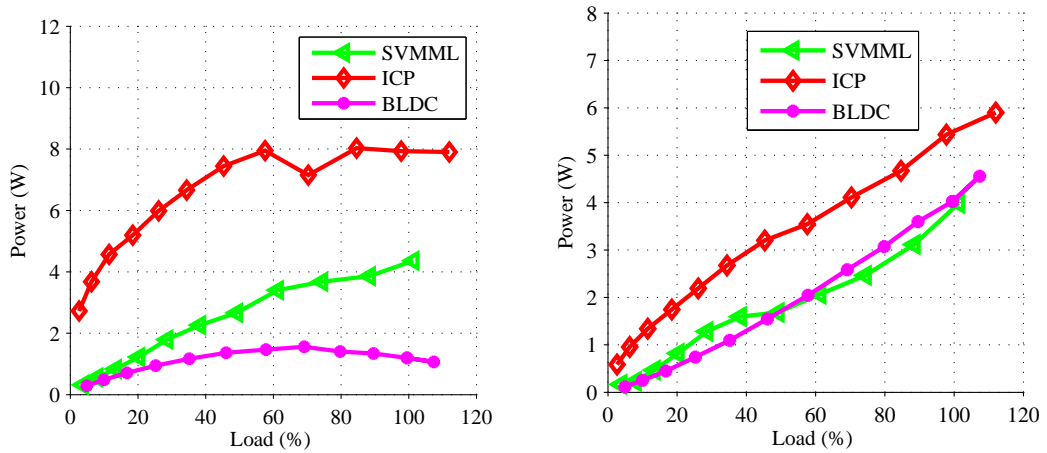


Fig. 6.28 Calculated efficiency including the losses in the inverter stage for the 375W BLDC motor when operated with BLDC current waveforms and sinusoidal current waveforms. The motor is connected to a speed dependent load, $T=b\omega$.



(a) Calculated switching losses in the inverter stage (b) Calculated conductive losses in the inverter stage

Fig. 6.29 Loss components in the inverter using different control schemes when operating the BLDC motor connected to a linear load providing 375W at rated operation.

6.3.6 Advanced angle BLDC control

This section will present how the advanced angle BLDC control, AABLDC, affects the efficiency at rated operation when implemented in the 375W BLDC motor drive. Table 6.1 presents the efficiency of the BLDC motor and the motor efficiency including the losses in the inverter stage for different advanced angles, ICP and SVML control at rated operation. It can be noted that the motor efficiency is increased for angles up to 15°. For larger angles the efficiency decreases. It can also be noted that the sinusoidal current control schemes, ICP and SVML, still results in the highest motor efficiency. However, when the inverter losses are included the overall best efficiency is found to be the same for the AABLDC and SVML control.

Table 6.1 Motor efficiency and motor efficiency including the inverter stage

Control	Motor efficiency (%)	Motor and inverter efficiency (%)	Load (%)
BLDC	77.1	76.3	100
AABLDC 5°	77.2	76.4	100
AABLDC10°	78.1	77.2	100
AABLDC 15°	78.1	77.3	100
ICP	79.1	76.8	100
SVML	79.0	77.2	100

6.3.7 4kW PMSM

Similar tests were made for a 4kW outer rotor PMSM motor used in fan applications. The motor was in this case connected to a quadratic load, loading the motor with 4kW at 1455rpm. A 2D drawing is shown in figure 6.30, having a length of 56mm. The DC bus voltage are assumed to be constant 550V and the phase resistance was calculated to 1.02Ω, at 50°. The converter losses are calculated in the same way as for the 375W BLDC motor, but replacing the IGBT module to a larger current and voltage rating, FS25R12KE3 G.

The BLDC and ICP control scheme can be implemented without any modifications due to its simple operation and independence on motor parameters. The SV-techniques presented in Section 6.3.4 can also be implemented directly, but an investigation of the behavior for different choices of φ_{sv} will be made. Furthermore, the current predictive method presented in Section 6.3.4 will be compared with the simulation result. Figure 6.31 shows the trajectory of the $i_{\alpha\beta}$ vector during one period of operation where the current reference is 10A and the speed 1468rpm, for two values of φ_{sv} , 0° and 15°. It can be noted that the largest deviation occurs at the location of the voltage vectors, and for the case where $\varphi_{sv}=15^\circ$ directly after the change of sectors. This is in accordance with the prediction since the voltage vector, leading the current vector by 75° will not increase the current vector magnitude at higher load, rather decrease it. Hence, by decreasing φ_{sv} , this problem will be reduced. The reason for the introduction of φ_{sv} was to reduce the error in the angle but since the angle is controlled this will not be an issue and φ_{sv} can be set to zero.

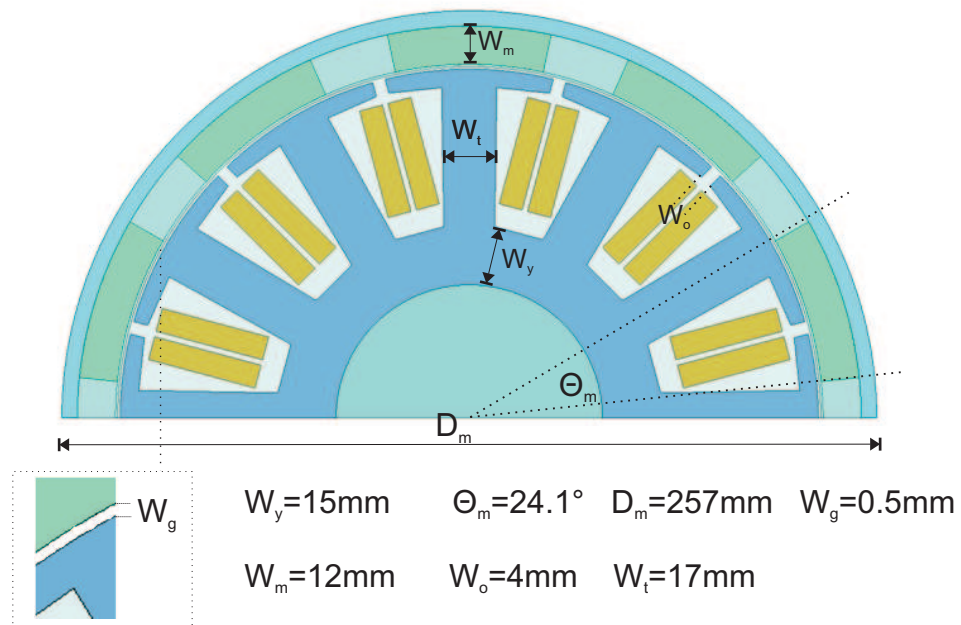


Fig. 6.30 Cross section of the 4kW PMSM, having a length of 56mm

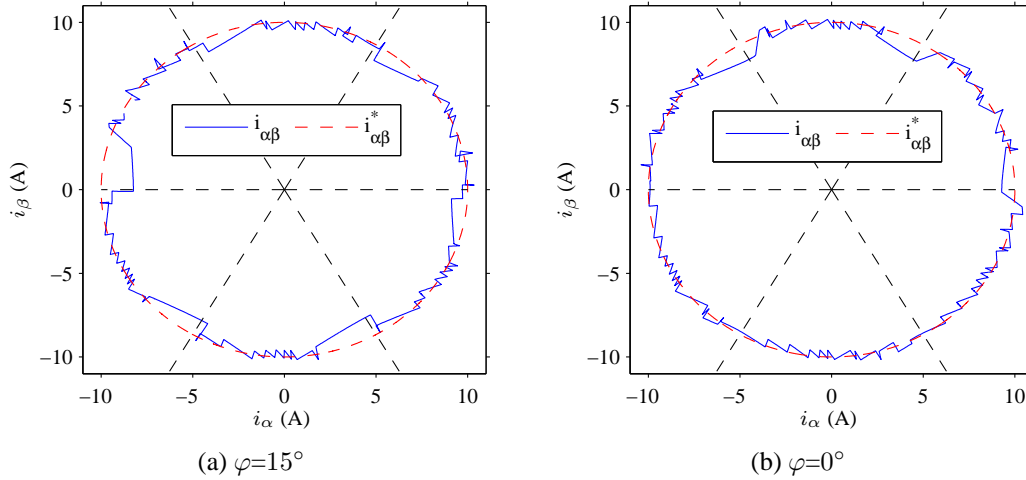


Fig. 6.31 Simulated current trajectory of the $i_{\alpha\beta}$ vector for the 4kW PMSM loaded with a quadratic load, $T=b\omega^2$. The reference current amplitude, 10A, and speed, 1468rpm, are fixed for the two cases of φ_{sv} . The dashed lines indicates the position of the different voltage space vectors.

From the simulation, the current derivative during one sample period was found to be 0.4-0.6A, which can be compared to the estimated value, 0.6A. The angle difference during one sample period was found to be maximum 4° which also was in accordance with the prediction.

The efficiency of the motor, controlled with the BLDC, IPC and SVML current waveforms are shown in figure 6.32. The result becomes similar as for the 375W BLDC motor, namely that the iron losses are much lower for the BLDC case at light load compared to IPC, as can be seen in figure 6.33, resulting in a higher efficiency whereas the efficiency levels becomes similar at higher load. It can be noted that the SVML control scheme results in the highest efficiency. It should also be noted that the BLDC current control never reaches the rated operation. This is due to the fact that the induced voltage becomes to high in order to produce the desired current. It is of course important to consider the negative effects that the BLDC current causes in the motor. These are not analyzed in detail but it can be expected that the torque ripple and audible noise increases when the motor is operated in BLDC mode.

Figure 6.34 shows the losses in the inverter for the different control strategies, showing a large improvement when changing from ICP to the other control schemes.

Finally, figure 6.35 shows the efficiency of the motor including the losses in the inverter case.

6.3. Efficiency comparison between different control schemes

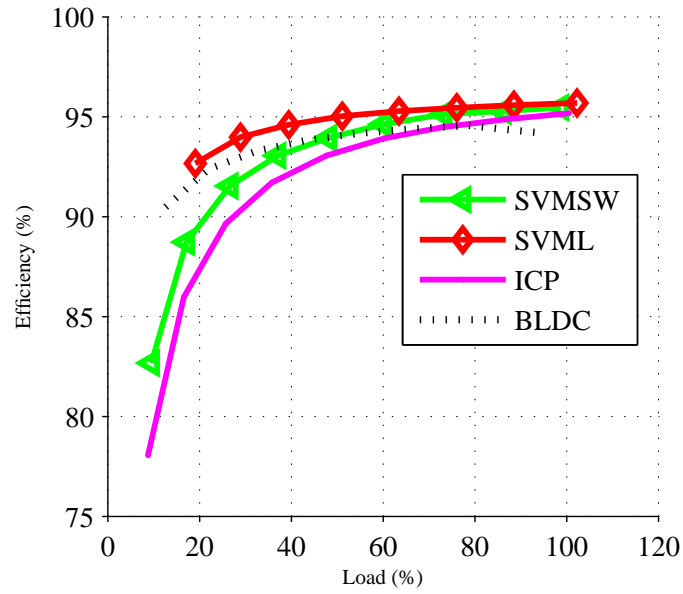


Fig. 6.32 Calculated efficiency of the 4kW PMSM when operated with BLDC current waveforms and sinusoidal current waveforms. The motor is connected to a speed dependent load, $T=b\omega^2$.

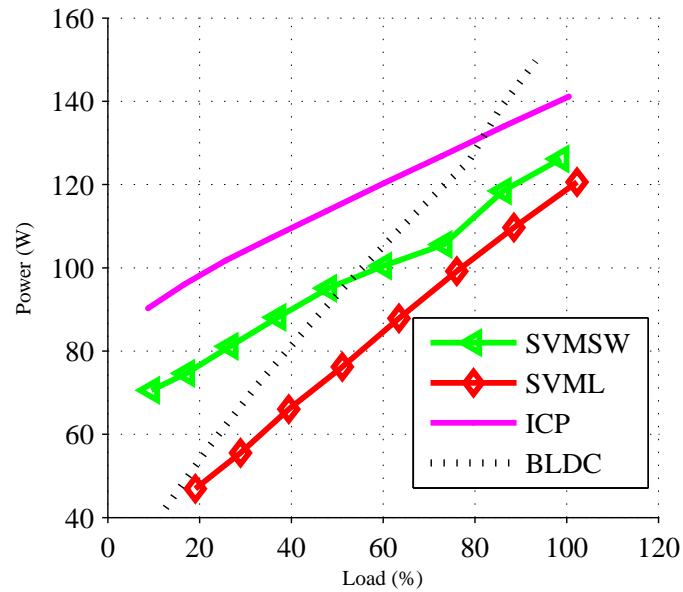


Fig. 6.33 Calculated iron losses of the 4kW PMSM when operated with BLDC current waveforms and sinusoidal current waveforms. The motor is connected to a speed dependent load, $T=b\omega^2$.

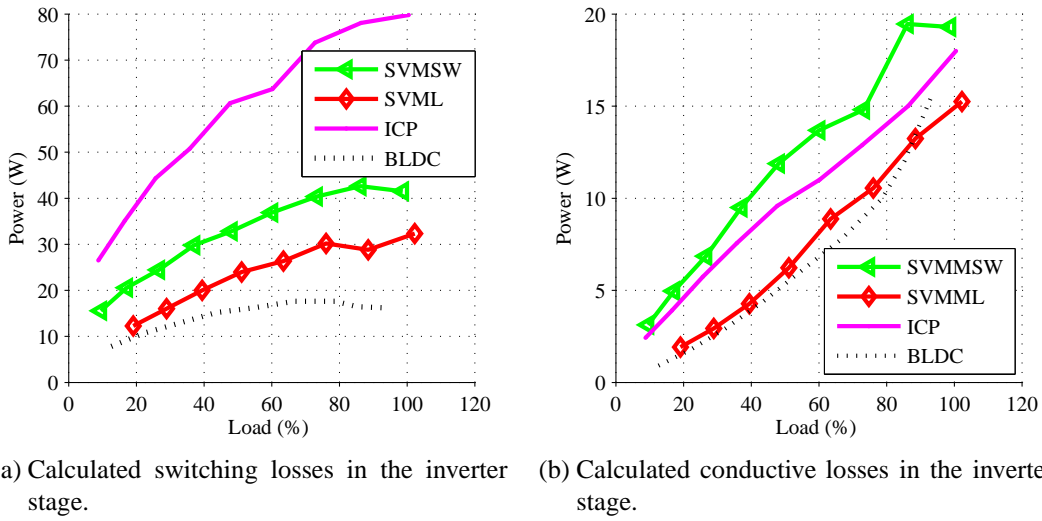


Fig. 6.34 Calculated losses in the inverter stage of the 4kW PMSM when operated with BLDC current waveforms and sinusoidal current waveforms. The motor is connected to a speed dependent load, $T=b\omega^2$.

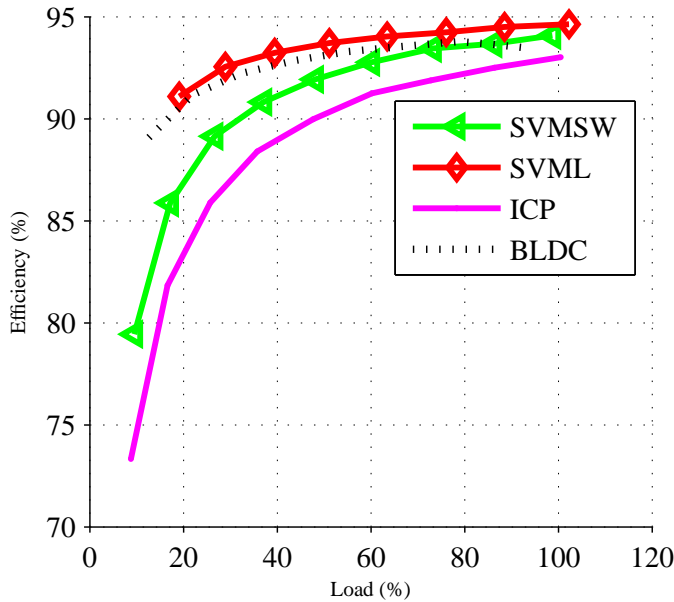


Fig. 6.35 Calculated efficiency including the losses in the inverter stage for the 4kW PMSM motor when operated with BLDC, ICP and SVMML waveforms. The motor is connected to a speed dependent load, $T=b\omega^2$.

FOC vs DCC

Simulations were performed for a FOC of the 4kW PMSM for comparison. The switching frequency was set to 10kHz, and calculation of the efficiency were calculated for the same quadratic load as before. Figure 6.36 shows the efficiency of the motor and for the motor including the inverter losses when the motor was controlled with SVMML and FOC. It can be noted that the efficiency of the motor is higher for the SVMML control. When the losses in the inverter stage are included the difference becomes even larger as expected.

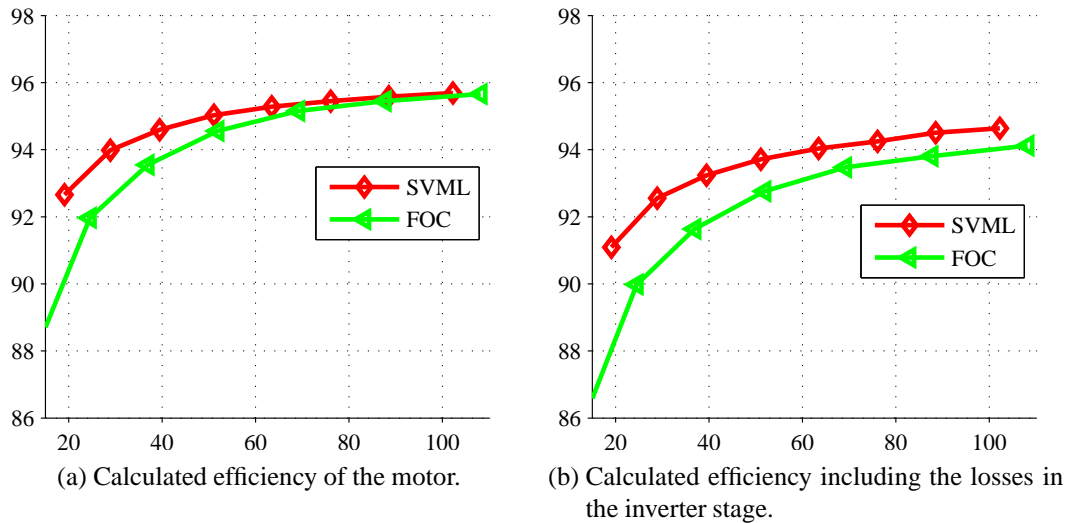


Fig. 6.36 Calculated efficiency of the motor and when the losses in the inverter stage are included for a FOC and SVMML control. The motor is connected to a speed dependent load, $T=b\omega^2$.

6.3.8 Influence of switching frequency

The 375W BLDC motor motor has now been operated with an updating frequency of the current controller at 28.6kHz and 40kHz. It was stated that the contribution of the iron losses due to the current ripple was significant at lower speeds due to the relatively high current ripple. It was found that iron losses decreased slightly, especially for the IPC control eg. 6% for the 20% load. It should be pointed out that an increase in switching frequency also introduces higher frequency content in the current which in turn results in higher eddy current losses in the stator iron. However, in the range of 20-40kHz, the fact that the current ripple has decreased in magnitude dominates the increase in frequency content. The increase in updating frequency also increases the switching losses in the converter resulting in an overall lower efficiency for the higher switching frequencies, especially for the PMSM case since the switching losses contributes more to the overall efficiency. Hence, from an efficiency point of view 20kHz can be regarded as a good choice.

6.4 Comparison between 2D and 3D modeling

A 3D model of the BLDC motor was made in order to quantify some of the different simplifications described in Section 3.2.2. The simulation time for a transient 3D model becomes extremely long, which makes it impossible to use for all the different configurations that are being tested. However, it is interesting, if possible, to quantify the different approximations made.

1. 2D to 3D. The first step is just to change from 2D to 3D and comparing the difference. Three different 3D models, one assuming a solid stator core and two with a laminated core having a stacking factor of 0.95 and 0.8 respectively. Figure 6.37 shows the induced voltage in the windings for 1000rpm. It can be noted that the 2D model has a higher induced voltage than the 3D case. This is due to the fact that the end effects are not accounted for in the 2D case, neglecting the leakage flux from the magnets. It can be expected that this effect will be significant for this motor due to the relatively thick magnets (10mm). The difference between a the solid and laminated case are almost negligible for the 0.95 factor but are reduced slightly for the 0.8 stacking factor. This is due to the nonlinearities in the iron core, since the increase in magnetic flux density, will not compensate for the reduced amount of iron material.

2. Longer rotor. The rotor is now increased with 5mm, equally distributed on each side of the stator, in accordance with the actual motor. It can be expected that the magnetic flux density will increase slightly. Furthermore, the end effects of the magnets are expected to decrease. The increase in induced voltage is approximately 10% V, (70.8V to 77.94V).

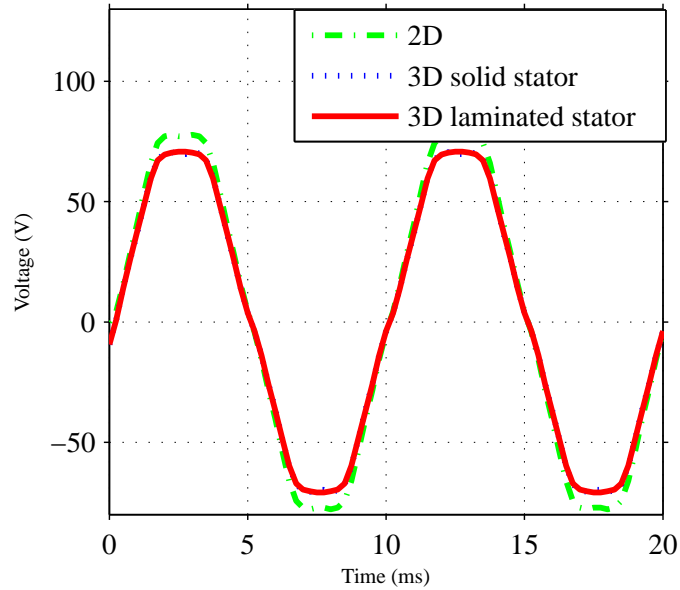


Fig. 6.37 Calculated induced voltage in the 375W BLDC motor for solid and laminated stator in 3D compared to the 2D calculations.

Figure 6.38 shows a comparison between the 2D case and the 3D case with longer rotor. It can be noted that the difference now is almost negligible. Since the rotor magnets are longer than the stator core, the 2D simplifications becomes more accurate since end effects becomes less important.

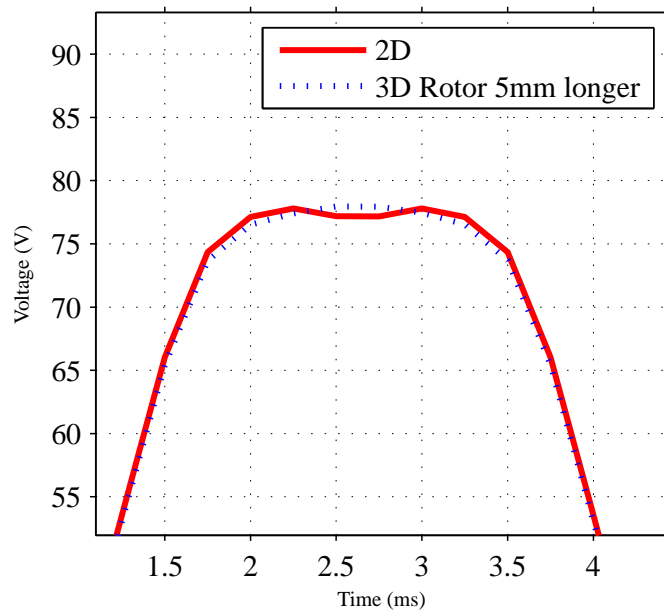


Fig. 6.38 Calculated induced voltage in the 375W BLDC motor for the 2D case and 3D case with a 5mm longer rotor.

Chapter 7

Efficiency difference between different PMSM and BLDC motor designs

This chapter will describe different design aspects of permanent magnet motors. The 375W BLDC motor modeled in Chapter 6 will serve as a starting point for the discussion. Focus will be placed on energy efficiency. Aspects such as choice of material, dimensions, motor type (PMSM/BLDC) will be considered.

7.1 Basic design considerations

Today's modern software makes it a relatively easy task to design a motor and to easily make parametric sweep of design parameters in order to find optimal designs based on the criteria defined by the user. The number of variations can of course be infinite without proper boundary conditions. Figure 7.1 shows a slice of a cross section of a permanent magnet motor, showing one magnet and one stator tooth, where all the inner dimensions are open for adjustments, and the outer dimensions are left fixed. In order to maximize the efficiency, the iron and the resistive losses needs to be balanced in a good way.

The output power

$$P_s \sim B_{to} A_{to} N_r I_s \quad (7.1)$$

where B_{to} is the peak flux density in the stator tooth, A_{to} is area of the flux path in the stator tooth, N_r is the number of turns in the stator windings and I_s is the magnitude of the stator current.

Hence, in order to reduce the stator losses for a constant operating point, the stator tooth can be made thicker, provided that the flux density can be kept constant by increasing the magnet thickness, reducing the number of turns in the stator winding. This will in turn result in a higher iron loss component. The copper losses can of course also be reduced by increasing the cross section area of the copper wires by making the slot area

larger. As long as the iron is operated in its linear region it is possible to reduce the amount of iron to increase the slot area, without affecting the operating point of the motor. Again this will increase the iron loss component due to higher flux densities in the motor. Hence, it is not straight forward to make an optimal design but by sweeping the different parameters presented, using a suitable software, an optimization can easily be performed for a given operating condition.

When an optimal design is found, the boundary condition needs to be changed in order to increase the efficiency further. If the outer dimensions are left fixed a change of the iron material used in the stator core can be a good choice. If the iron is changed the tradeoff between the stator and iron losses will be different and a different motor design will result in optimum efficiency for a given operating point. There is also a limit on how thick the magnet can be made in order to increase the flux in the motor which can reduce the flexibility in the motor design process for a given magnet material.

An alternative to replacing the magnet material to a stronger magnet, can be to change the inner rotor design to an outer rotor design which will be described in the oncoming section.

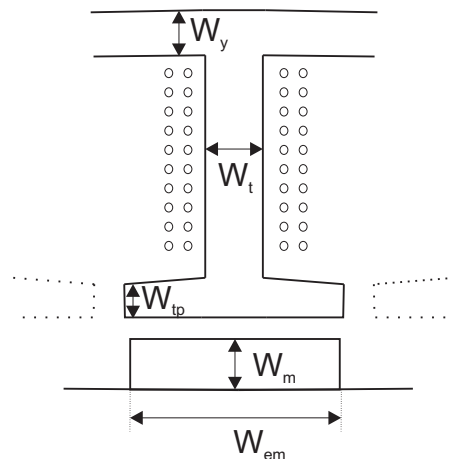


Fig. 7.1 Cross section slice of an inner rotor motor.

7.2 Modifications of the original 375W BLDC

The original design of the BLDC motor was described in Chapter 6. It was shown that the motor had relatively high stator losses at rated operation, namely 78% of the electrical motor losses. As a result, it is possible to modify the design in order to improve the efficiency at rated operation by changing the balance between resistive and stator losses. In order to do this, the magnetic flux in the stator needs to be increased. However, the flux level in the original is close to its maximum, for the given magnetic material. Hence, two

cases are considered, replacing the magnets with NdFe35 and changing the design to an outer rotor motor keeping the same magnet material.

For the first case it is evident that the flux level in the motor can be increased due to stronger magnets. The flux level in the stator core is also increased for the outer rotor case, since more magnet material can be used, (thicker magnets for the original motor will not increase the flux density in the air gap).

7.2.1 Replacement of magnet material

The magnet material of the original design was now replaced with NdFe35. Keeping the same outer dimensions the rating was found to increase with approximately 100%. In order to obtain the same motor rating of 375W at 1000rpm the motor was scaled and identical ratings was obtained at 80% of the original size. The iron grade was the same as for the original design, M800 65A. The analytical Maxwell tool RMXprt where used for the design where 30 000 motor designs were tested by sweeping the different design parameters. The motor design giving the highest efficiency at rated operation was chosen for the comparison. Table 7.1 presents the difference between the two 375W motors at rated operation and the difference in material consumption. It can be noted that the efficiency of the motor having NdFe35 magnets is lower at rated operation. This is due to the fact that the size is reduced. It should further be pointed out that the resistive and iron losses now are approximately equal at rated operation. As a result, it is possible to change the iron grade in order to improve the efficiency of the NdFe35 motor whereas less is gained by replacing the iron grade for the original design.

Table 7.1 Difference in material consumption and motor efficiency

Motor	Magnet	Iron	Copper	Efficiency
Original	337g	1960g	1070g	77.1%
NdFe	73g	1260g	512g	75.6%

7.2.2 Inner vs outer rotor motor

This section will present a comparison between the 375W BLDC motor and a corresponding outer rotor motor. It is fairly difficult to do an adequate comparison due to the number of factors involved. A number of boundary conditions will be defined and form the base for the comparison. If the outer rotor motor is designed, keeping the same outer dimensions as for the inner rotor motor, (length and diameter), it is possible to increase the rating with 50-80%. However, it is assumed that the enclosure of the motor needs a distance to the moving outer rotor, decreasing the diameter with 20mm, this is of course not always needed. The improvement of iron losses was fairly limited in the original design as mentioned in section 7.2. This has now changed since more magnet material can

be used to increase the flux. As a result the flexibility in copper vs. iron losses increases which might speak for an improvement of the iron grade. The following two cases are tested and compared to the original motor:

1. Outer rotor motor reducing the outer diameter with 20mm. The airgap, slot opening and motor length is kept fixed, and equal to the original design. The material used is also fixed and same as for the original case. The design is developed in the Maxwell tool RMexp by evaluating a parametric sweep of the dimensions inside the motor, presented in section 7.1 and number of stator turns. More than 30 000 variations are tested and the most promising motor is selected for FEM evaluation.
2. The iron grade is changed to M400-50A and the the same analytical analyze is made, sweeping over 30 000 combinations.

The efficiency is observed at rated operation. The maximum efficiency is obtained for slightly different motor design parameters due to the fact that the trade off between decreased copper and iron losses are different.

Figure 7.2 shows the estimated efficiency at rated operation for different magnet thickness, having a magnet embrace of 85%, where the highest efficiency of each magnet thickness configuration is presented. The figure also includes the result when the iron grade is improved. It can be noted that thicker magnets can be used in order to increase the efficiency when the M400 grade is used.

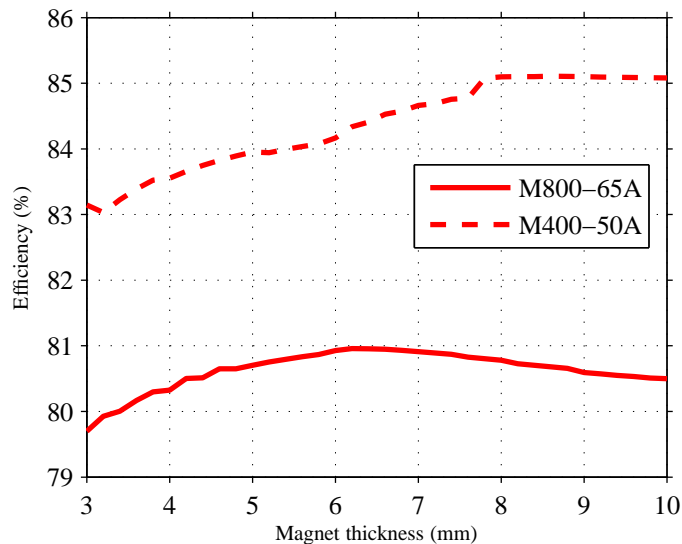


Fig. 7.2 Calculated efficiency at rated operation of the two different 375W outer rotor BLDC motors for different magnet thickness at rated operation.

Figure 7.3 shows the efficiency together with the iron and resistive losses in the stator windings for different motor designs, around the maximum efficiency. It can be noted that

the efficiency approximately peaks when the two loss components has the same magnitude. Further observation also indicates a relatively flat efficiency optimum, meaning that a reduction in copper losses results in a similar increase in iron losses around the optimum efficiency point. The case with improved iron grade gives similar result. Hence, it is not straight forward which design to choose.

Three designs of case 1 are chosen in order to demonstrate the difference in efficiency over the whole operating range. Design 1 is picked at the absolute peak of the efficiency curve shown in figure 7.3. Design 2 is picked on side of the optimum having lower iron losses but higher copper losses. Finally, design 3 is picked on the other side of the efficiency optimum, having higher iron losses and lower copper losses. Furthermore, one design, referred to as design 4, of case 2 is chosen for comparison with the original design, and is picked at the absolute efficiency optimum from the analytical analysis.

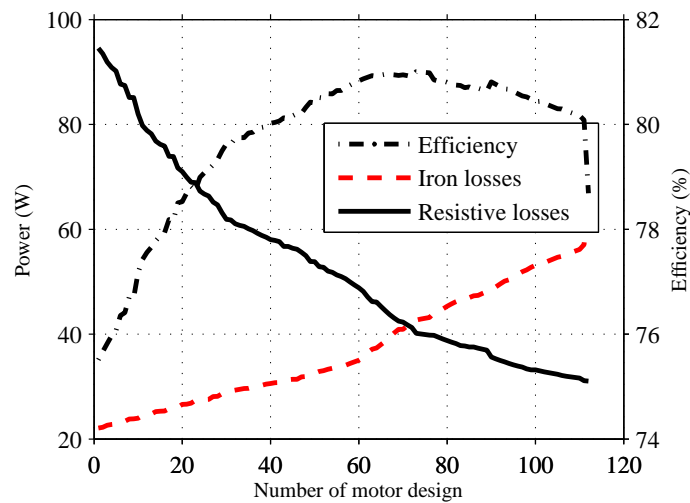


Fig. 7.3 Calculated efficiency, iron and resistive losses at rated operation of the 375W outer rotor BLDC motor for different design parameters, sorted by the iron losses.

The different motor designs are then modeled using FEM calculations coupled with the circuit simulation of the frequency converter. The control scheme is identical to the one described in Chapter 6. Figure 7.4 shows the efficiency for the five cases. It can be noted that design 1-3, having M800-iron grade have almost identical efficiency of 84.7% at rated operation, which is in accordance with the analytical design. When the load decreases, the design having the lower iron losses, design 2, at rated operation becomes more efficient.

The difference between design 2 and 3 becomes more clear if the load profile changes. Figure 7.5 shows the efficiency where 100% load corresponds to rated speed and 50% of rated operation power, namely 187.5W. It is now clear that the motor with the higher iron loss component, design 3, has the lowest efficiency.

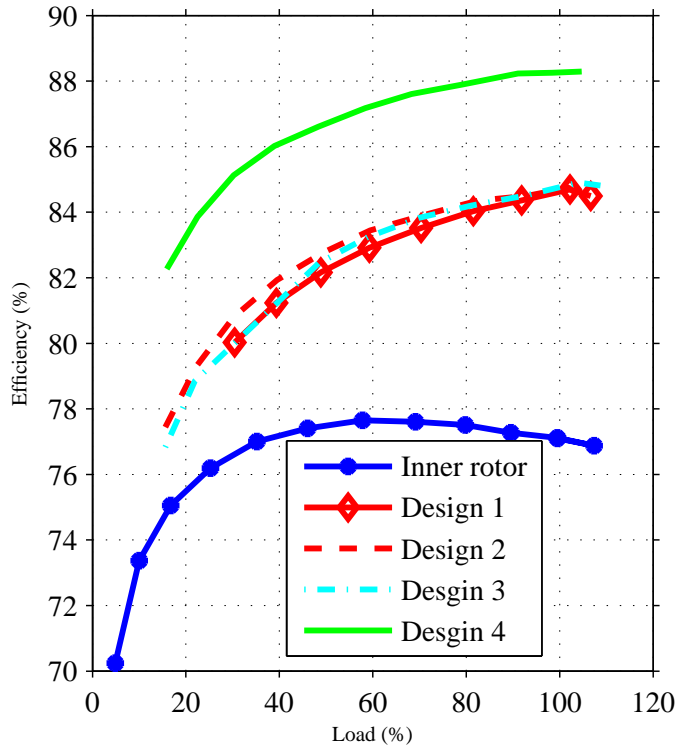


Fig. 7.4 Calculated efficiency, for the four new outer rotor designs compared with the original, inner rotor motor. The motors are connected to identical loads, $T = b\omega$, providing 375W at 1000rpm.

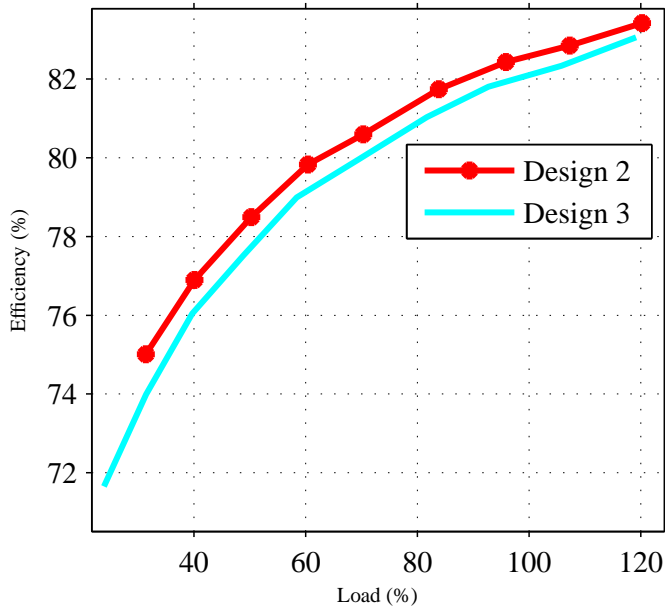


Fig. 7.5 Calculated efficiency, for design 2 and 3. The motors are connected to identical loads, $T = b\omega$, providing 50% of rated operation (187.5W) at 375W at 1000rpm.

7.3 Design of a 1.2kW 1000rpm PMSM and BLDC

This section will describe the design procedure for a 1.2kW 1000rpm PMSM and BLDC motor. The prototypes developed will be built. The main goal is to verify the simulation tool which are not possible for the commercially available motors tested due to the lack of detailed construction information of the motors. A second goal is to compare the PMSM and BLDC design, both theoretically using Maxwell/Simplorer simulations but also with measurements. It should be pointed out that it is difficult to make a fair comparison between the motor types. However, provided fixed boundary conditions, eg. fixed outer dimensions the comparison becomes easier and can provide an indication on which topology that are best suited for a pump/fan application.

7.3.1 Initial, analytical design settings

As a first step, the Maxwell tool RMexp is used in order to obtain a good initial guess of the motor design. The following design parameters are determined in order to reduce the number of variations

1. The iron grade is chosen to M400-50A with consultants with the steel manufacturer. According to the manufacturer, thinner laminations are only recommended for applications operated with 200-400Hz or higher.
2. The magnet material was chosen to NdFe30.
3. Number of pole pairs was set to 6.
4. Airgap 0.5mm in consultant with the motor manufacturer.
5. Slot fill factor (Copper area/Slot area) 40%, in consultant with the manufacturer.
6. Slot opening 2.4mm due to manufacturing issues.
7. 300V DC bus voltage.
8. Maximum current density in the stator windings $5A/mm^2$.
9. Zero skewing of the stator or the rotor magnets due to model complexity.
10. The mechanical losses in the bearings are expressed as, $P_{fric} = b_f w_r^2$, where b_f is calculated to give 6W losses at 1000rpm.

The result from the analytical testings are left out from this thesis. Thousands of different combinations of the different dimensions where tested and the most promising designs where chosen for further detailed analysis using FEM modeling.

Figure 7.6 shows a 2D drawing of the two motor designs, having a motor length of 53mm. The stator cores are identical for the two cases. It should be pointed out that this is a sub optimal choice from a efficiency point of view. However, the relative improvement that could be made by changing the design was found to be extremely small and equal stators where chosen for convenience. The magnet thickness and embrace were tested with FEM calculations, as was the effect of the stator turns.

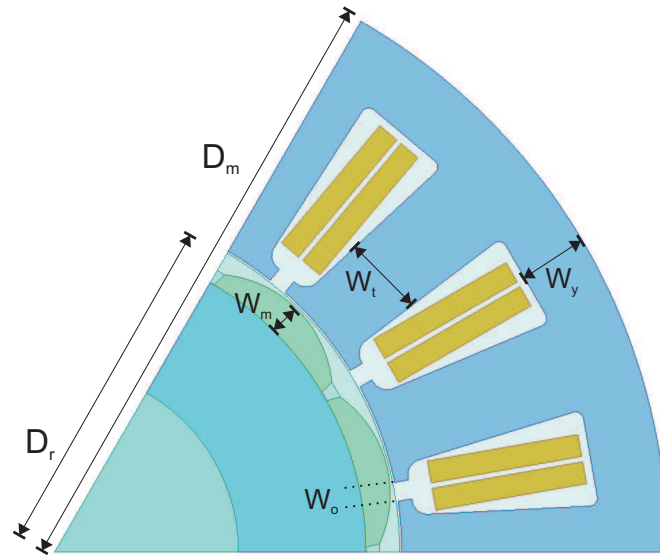
7.3.2 Influence of the number of stator turns

A more detailed analysis has been performed on the BLDC motor and its number of turns. Figure 7.7 shows the efficiency of the motor for two different load situations, 100% and 50% of rated operation, when the motor is operated with BLDC currents and with the ICP control scheme. It can be noted that the efficiency increases as the number of turns increases. However, when the number of turns is increased above 48 turns the BLDC motor is no longer able to produce the desired torque whereas the ICP control keeps increasing in efficiency. It can also be noted that the efficiency is increased at 50% of rated operation. As a result, from this analysis it can be advisable to maximize the number of turns if PMSM control are allowed. The motors that where manufactured had 40 turns in the stator winding since no detailed analysis had been made on the topic at the time of manufacturing. Hence, in retrospect the number of stator turns should have been increased to at least 48.

7.3.3 Simulation result PMSM vs BLDC

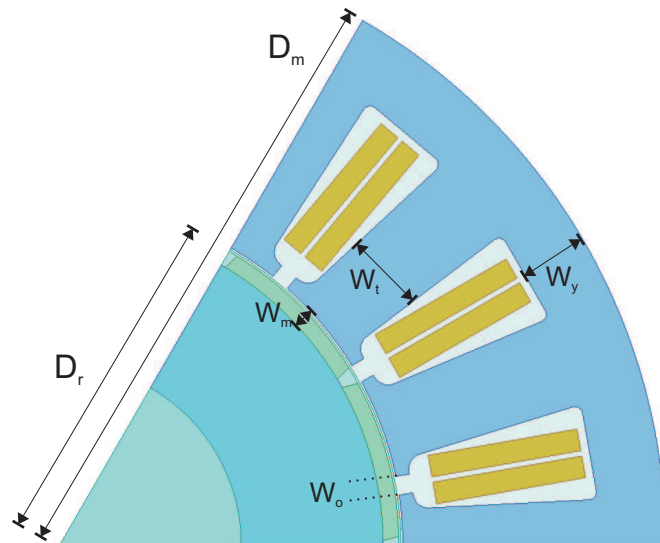
This section will present the simulation result from the proposed BLDC and PMSM motor design, having 40 turns in the stator winding. The PMSM will be operated with ICP and SVMML described in Chapter 6. The BLDC control will also be identical to that described in Chapter 6. The IGBT module used for the loss calculation is the same as for the 375W BLDC motor, FS10R06VE3.

Figure 7.8 shows the efficiency of the two motors for the different control strategies. It can be noted that the difference is almost negligible for the BLDC motor and the PMSM motor provided the more complex control strategy SVMML. The iron and winding losses can be seen in figure 7.9. It can be noted that the the PMSM with ICP control has lager amount of iron losses compared to the SVMML and BLDC motor. Furthermore, the copper losses in the stator windings are found to be higher for the PMSM compared to the BLDC motor whereas the opposite holds true for the iron losses. When the losses in the inverter stage are included the BLDC motor has the highest efficiency as shown in figure 7.10.



$W_y = 8\text{mm}$ $D_r = 43.6\text{mm}$ $D_m = 77\text{mm}$
 $W_g = 0.5\text{mm}$ $W_m = 4\text{mm}$ $W_t = 9.3\text{mm}$
 $W_o = 2.4\text{mm}$ magnet embrace 90%

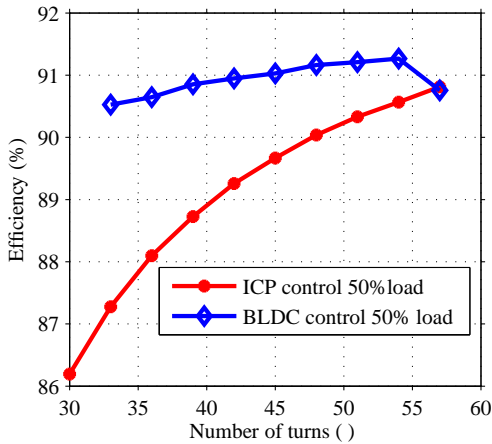
(a) PMSM design



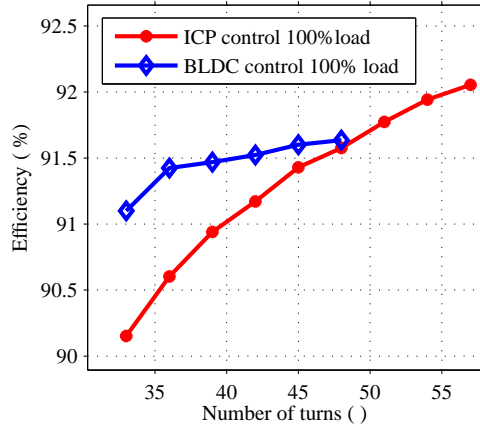
$W_y = 8\text{mm}$ $D_r = 43.6\text{mm}$ $D_m = 77\text{mm}$
 $W_g = 0.5\text{mm}$ $W_m = 4\text{mm}$ $W_t = 9.3\text{mm}$
 $W_o = 2.4\text{mm}$ magnet embrace 90%

(b) BLDC design

Fig. 7.6 Design of a 1.2kW BLDC and PMSM motor. The rotors are identical, having a core length of 53mm.



(a) Motor efficiency of the BLDC motor at 50% of rated operation



(b) Motor efficiency of the BLDC motor at 100% of rated operation

Fig. 7.7 Efficiency of the 1.2kW BLDC motor with different number of turns, connected to a quadratic load characteristic providing 1.2kW at 1000rpm. The motor is controlled with BLDC and ICP current control.

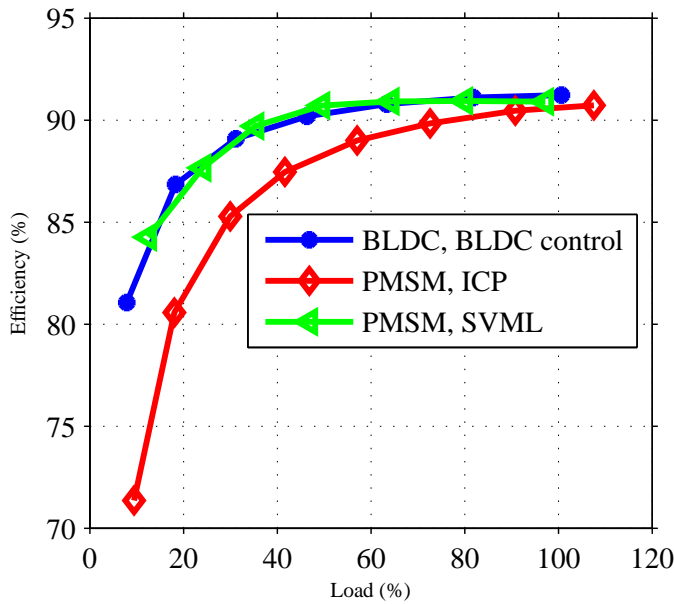


Fig. 7.8 Calculated efficiency, for the BLDC and PMSM motor, excluding the inverter losses, for BLDC control of the BLDC motor and ICP and SVMML control of the PMSM motor. The motors are connected to identical loads, $T = b\omega^2$, providing of 1200W at 1000rpm.

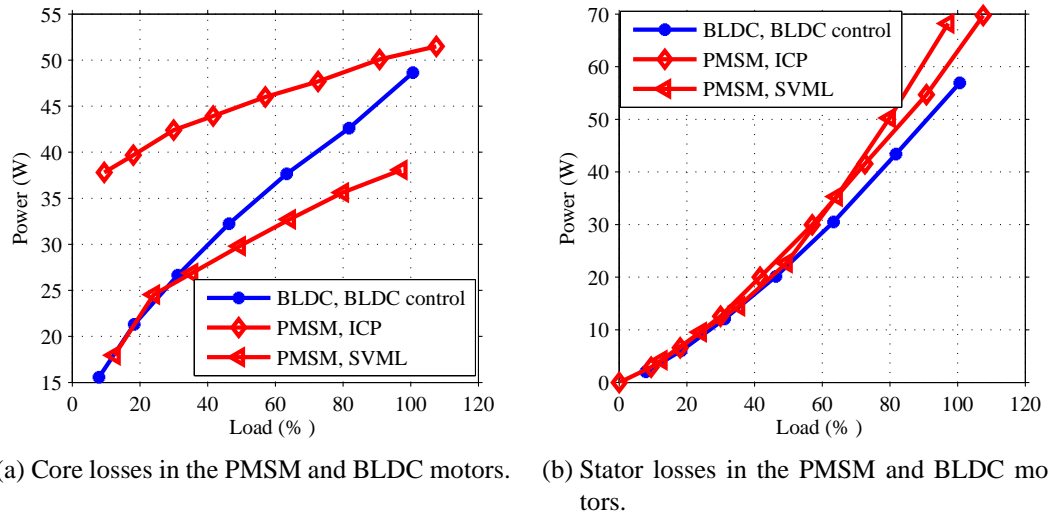


Fig. 7.9 Iron and stator loss components in the BLDC motor operated with BLDC control and ICP and SVML control of the PMSM motor. The motors are connected to identical loads, $T = b\omega^2$, providing of 1200W at 1000rpm.

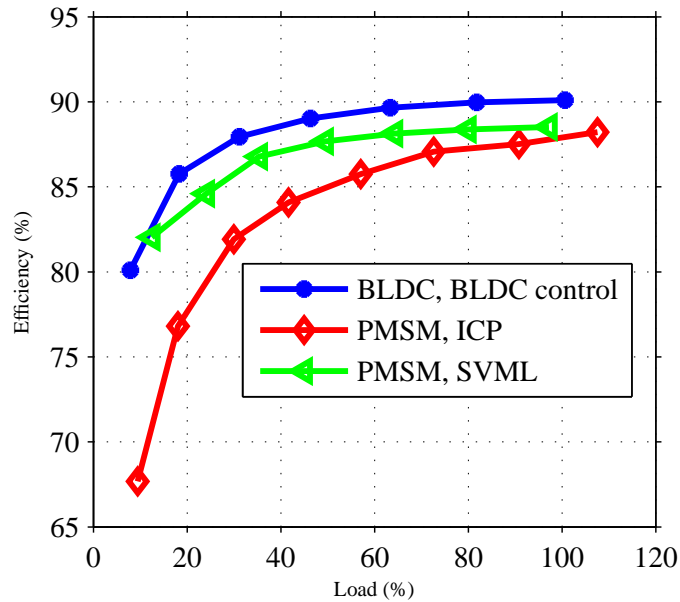


Fig. 7.10 Calculated efficiency, for the BLDC and PMSM motor, including the inverter losses, for BLDC control of the BLDC motor and ICP and SVML control of the PMSM motor. The motors are connected to identical loads, $T = b\omega^2$, providing of 1200W at 1000rpm.

Chapter 8

Experimental investigation of different PWM control schemes for IM

This chapter will describe the measurement setup and the performed measurements on a 4kW IM drive system. In addition, a description of the frequency converter layout will be provided.

8.1 Measurement setup

In order to measure the losses in the converter accurately, the temperature was measured on the heat sink of the different components. In order to relate this temperature to a known power dissipation, a DC power supply was connected, short circuited by each component, while the voltage over it and current through it was measured. The temperature was then measured at different known power dissipation and in this way a power loss calibration was obtained.

The input power to the converter, P_{dc} and the input power to the motor P_{IM} has been measured with two different power analyzers, the speed, n , with a tachometer and the shaft torque, T_L was measured with a torque transducer. Table 8.1 lists the measurement equipment and the measured quantities. A schematic over the measurement setup can be seen in figure 8.1 and figure 8.2 shows a part of the laboration setup.

8.1.1 Converter leg

A circuit diagram of one leg of the converter can be seen in figure 8.3 and figure 8.4 shows a photo of one leg. The freewheeling diodes F1 and F2 are SiC Schottky. This type of diodes were chosen due to its fast switching characteristics and the low recovery according to the manufacturer. The transistors T1 and T2 are MOSFET transistors. The diodes D1 and D2, are Schottky diodes, and connected in series with the MOSFET due to the parasitic diode in the MOSFET which unfortunately was a problem with this type of

Table 8.1 Measurement instruments

Type	Measured quantities
Norma 61D2 3-phase power analyzer	$I_{a,b,c}, U_{a,b,c}, \cos(\varphi) P_{a,b,c}$
Yokogawa WT 1600 power analyzer	I_{dc}, U_{dc}, P_{dc}
Lecroy digital Oscilloscope 9304 CM	$I_{abc}, U_{abc}, I_{dc}, U_{dc}$
Lecroy Differential voltage probe AP032	U_{abc}, U_{dc}
Lecroy Current probe AP015	I_{abc}, I_{dc}
PEM Rogowsky coil CWT03	$I_{T,D}, I_F$
Torque transducer T30 Fn	T_{IM}
Raynger ST 60 ProPlus IR thermometer	Temperature

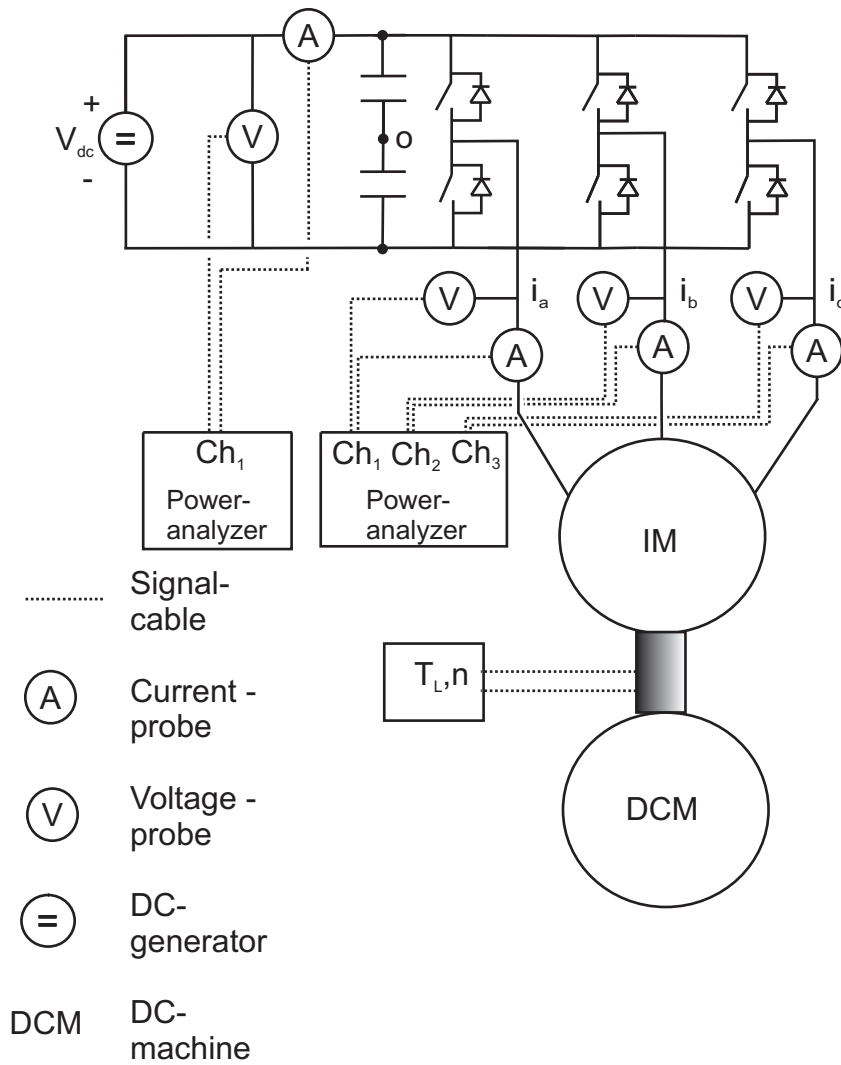


Fig. 8.1 Measurement setup

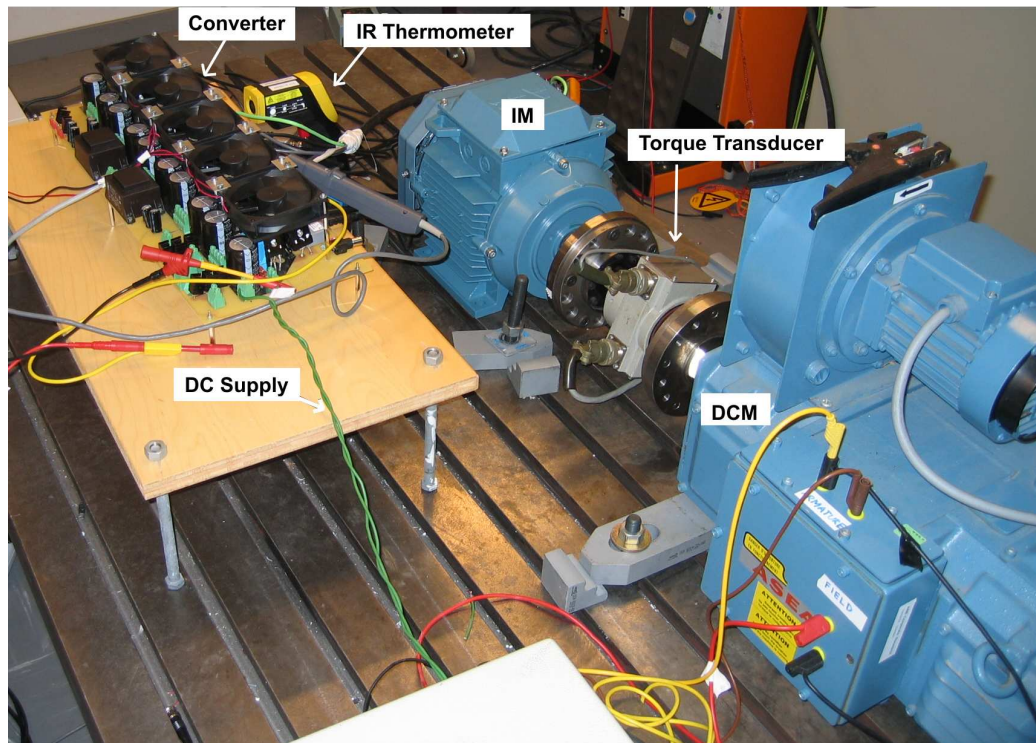


Fig. 8.2 Laboration setup

MOSFET. MOSFET transistors were chosen due to its superior switching speed compared to its counterparts. The extra inductance, L_{extra} , was added due to some initial problem during the switching transitions causing the transistors to break down. Figure 8.5 shows the original gate voltage with a 70V DC link voltage and a load connected between the midpoint and the negative DC bus. The figure shows the turn off and turn on of T2 and T1 respectively. When the gate voltage applied to T1 increases, an oscillation in the gate voltage applied to T2 appears, caused T2 to turn on. As a result T1 and T2 created a short circuit of the DC voltage causing a high current through the components which in turn resulted in breakdown of the transistors. The oscillations was partly tracked down to D1 and D2, (the reason is yet unknown and will be dealt with in future work). Hence a ferrite bead, L_{extra} , was mounted on one leg on each diode. Table 8.2 lists the different components in the converter where T_j is the junction temperature, I_D the current through the device, V_{GS} the gate voltage, R_{dson} the on-state resistance of the transistor and V_R is the on-state voltage drop of the diodes.

8.1.2 Gate driver

The original gate driver provided a gate voltage of 0-15V. In order to obtain an extra safe margin on the gate voltage on the transistor that was turned off, a capacitor, with a parallel zener diode was connected in series with the gate resistance. The capacitor is charged to

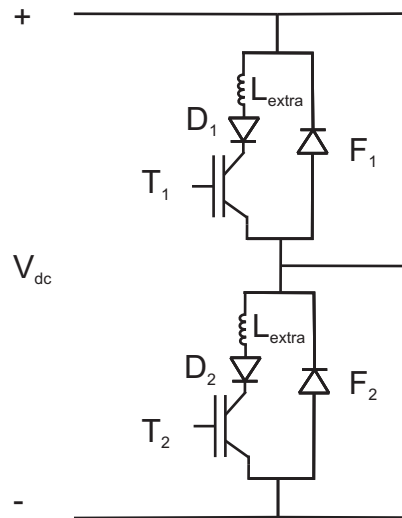


Fig. 8.3 Circuit diagram of one leg in the converter.

Table 8.2 Components

Comp.	Type	V_{max}	I_{max}	Condition	Value
T1-T6	MOSFET	600V	60A	$I_D=44A, V_{GS}=10V, T_J=25^\circ$ $I_D=44A, V_{GS}=10V, T_J=150^\circ$	$R_{dson}=40m\Omega$ $R_{dson}=110m\Omega$
D1-D6	Schottky	8V	80A	$I_D=40A, T_J=25^\circ$ $I_D=40A, T_J=125^\circ$	$V_f=0.34V$ $V_f=0.23V$
F1-F6	Schottky, SiC	600V	12A	$I_D=12A, T_J=25^\circ$ $I_D=40A, T_J=150^\circ$	$V_f=1.5V$ $V_f=1.7V$

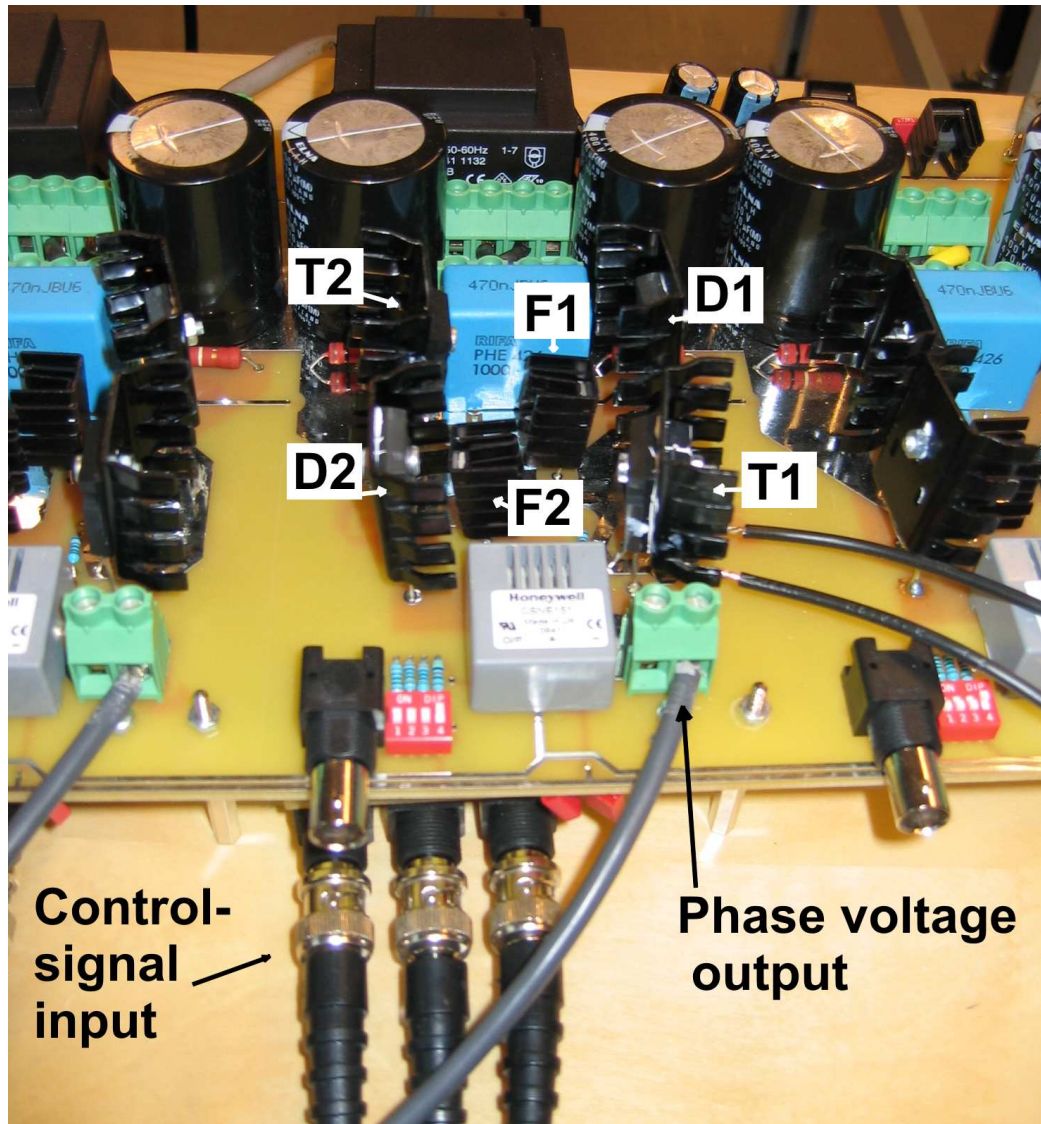


Fig. 8.4 One leg of the converter.

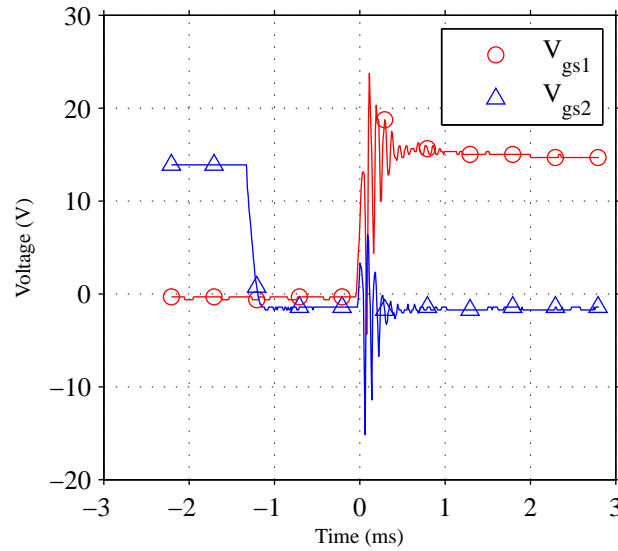


Fig. 8.5 Gate voltage of the upper and lower MOSFET.

the breakdown voltage of the zener diode and results in a corresponding negative voltage on the gate at turn off. The DC-level on the gate driver was increased from 15V to 18V and the zener diode was chosen to 4.4V resulting in a +14.6V and -4.4V gate voltage. The capacitor was chosen to $2\mu\text{F}$ in order to keep a negative voltage on the gate during 20ms which is sufficient for all operating condition during the tests (60° switch stop at 15Hz corresponds to 12ms). It can be noted that the capacitor slows down the gate driver but optimal gate drive design is not the objective of the study presented in this chapter.

Finally, the gate resistance was selected to 4Ω . Figure 8.6 shows the circuit diagram of a part of the the gate driver where G_{d+} and G_{d-} are connected to a totem-pole amplifier arrangement driven by a high and low side gate driver, IR2113. Figure 8.7 shows the gate voltage after the modifications, where the oscillations now are negligible.

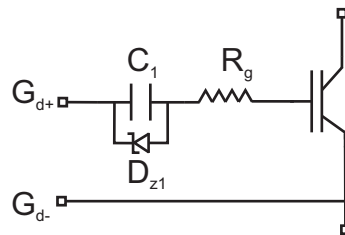


Fig. 8.6 Part of the gate drive circuit after modification.

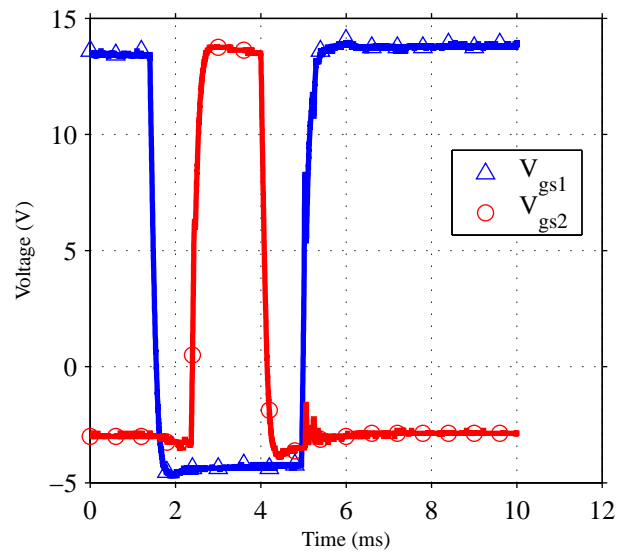


Fig. 8.7 Gate voltage of the upper and lower MOSFET after modification of the gate circuit.

8.2 On-state measurement

The on-state measurements were performed in order to investigate the on-state losses in the converter. Each component was connected to a DC power supply, able to deliver a sufficiently high current. The current and the voltage drop across each component was measured. Furthermore, since the voltage drop is temperature dependent, it was desirable to perform the measurement in the same temperature range as for normal operation. Hence, the measurements were performed at approximately 45°C.

Figures 8.8 and 8.9 show the voltage drop across the transistor and the diode respectively, as a function of current, in the range 0-20A. The data sheet of the transistor states an on-state resistance, R_{dson} , of 45mΩ at 25°C, 44A drain current and 10V gate voltage. The results of the measurement results in approximately 50mΩ at 20A. However, the temperature during the measurement was 45° resulting in a slight increase in R_{dson} .

The measured voltage drop across the diode was 0.27V at 20A. This can be related to the data sheet, which states, a maximum voltage drop of 0.34V at 40A and 25°, decreasing to 0.23V at 125°.

The voltage drop over the freewheeling diode was measured in the current range of 0-15A. Figure 8.10 shows the result. The data sheet of the diode states a typical voltage drop of 1.5V at 12A and 25° increasing to 1.7 at 150°.

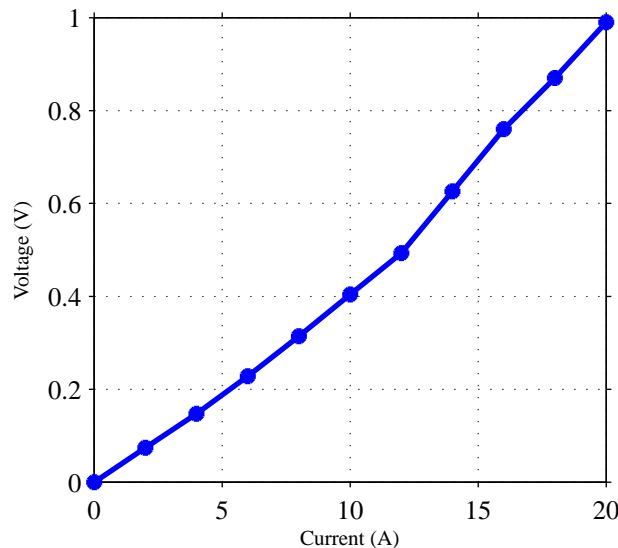


Fig. 8.8 Measured voltage drop across the transistor at 45°C $V_{GS}=14.4V$.

The results from the on-state measurement are used together with the the description presented in Section 3.3 in order to estimate the conductive losses in the converter.

Measurements were also performed with short circuited components in order to investigate the conductive losses in the PCB traces of the converter. However, the influence of these losses was found to be negligible.

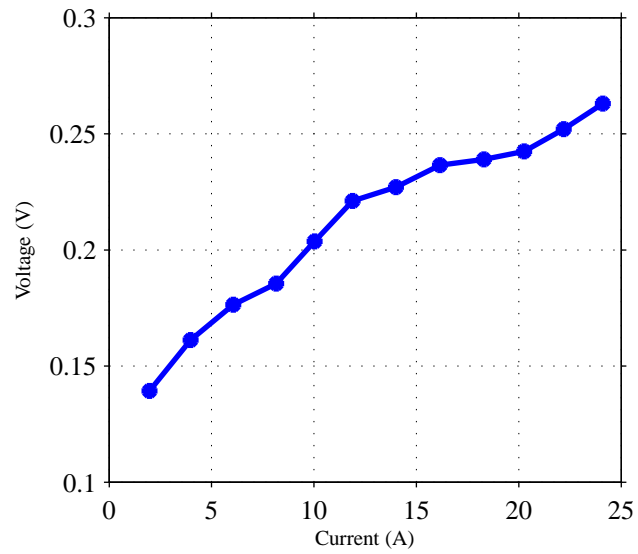


Fig. 8.9 Measured voltage drop across the series diode at 45°C.

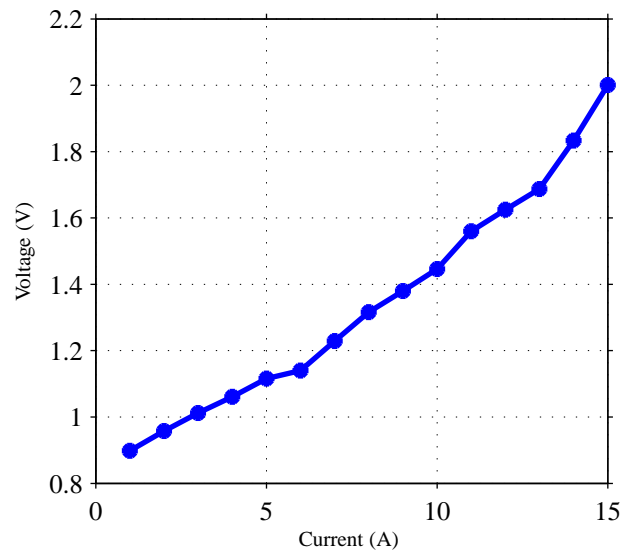


Fig. 8.10 Measured voltage drop and current through the freewheeling diode at 45°C.

8.3 Temperature calibration

The losses in each component were obtained by measuring the temperature on each heat sink and relate this to a known power dissipation in the component. Hence, the same connection as for the measurement of the on-state losses was used. The cooling fan of the converter was operating in its lowest state in order to achieve highest possible temperature difference of the components. Higher temperature difference is of course possible without the fan. However, this increases the heat transfer between the components. The temperature of the heat sink was taken after it had stabilized, 6 minutes, and was then cooled down to the ambient temperature before next measurement. This was done in order to have the identical condition between the calibration and the measurements. It should be noted that the temperature of the different heat-sinks affects each other. As a result, it is not possible to make the calibration on one component while the others have the ambient temperature. Hence, each calibration was performed while keeping the closest component at 45°C. This is of course not 100% accurate but decreases the error. Further errors are conductive heat energy in wires between the components. However, the absolute accuracy is not as important as the relative difference between different converter operation points.

8.4 Measurement of switching transitions

The switching transition measurements were performed in order to obtain the switching losses as a function of load current. A 1mH inductance was connected in series with the load, in order to obtain a constant current during the transitions. Figure 8.11 shows the circuit diagram of the connection. The lower transistor was first at its on-state, enough time for the current to reach its steady state. Then a short turn off and turn on pulse were given, (short enough in order to keep the current constant). The voltage was measured across the load, T2 and D2 together with the current through each component. The resistance was changed in order to obtain different load currents.

Figure 8.12 shows the turn on transition of T2. It can be noted that the current through T2-D2 has an overshoot due to the discharge of T1 and F1. The load current is 7.5A and it takes approximately $1\mu\text{s}$ until it has reached this value. This long duration can be explained by the extra inductance that has been added as described in Section 8.1.1. The inductance will force a current to flow in the T2-D2-DF2 loop as can be seen in figure 8.13.

Figure 8.14 shows the the switching transition when T2 turns off. It can be noted that the voltage has an overshoot before it reaches the DC link voltage. This overshoot results from the stray inductance in the circuit.

Figure 8.16 shows the the switching transition for F1 when T2 turns on. It can be noted that, in contradiction to the data sheet, the current becomes negative for a short period of time before it settles at 0A.

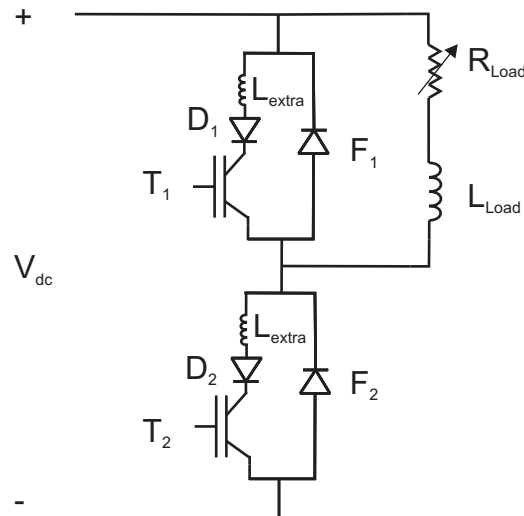


Fig. 8.11 Circuit diagram of one leg in the converter with applied load.

Figure 8.15 shows the the switching transition for F1 when T2 turns off. It can be noted that there is an oscillation of the current through F1 before it reaches the load current. The reason for this is yet unknown.

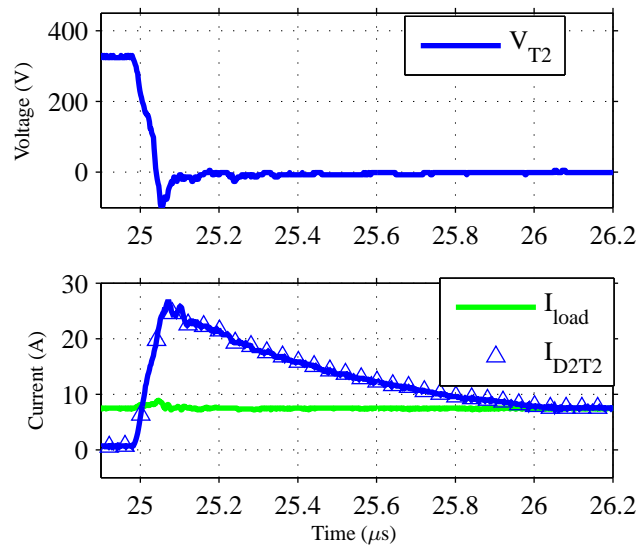


Fig. 8.12 Switching transition for the turn on of T2, for a constant load current of 7.5A.

The result from this section is used together with the the description of switching loss calculation in Section 3.3 in order to estimate the switching losses.

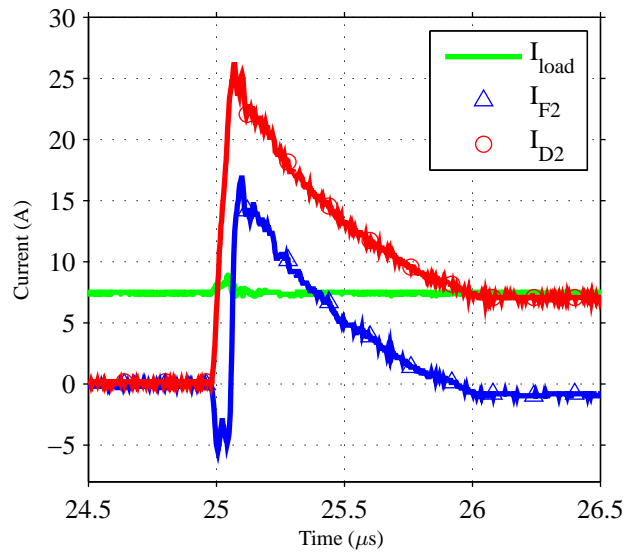


Fig. 8.13 Current through D2 and F2 during turn on of T2 at a load current of 7.5A.

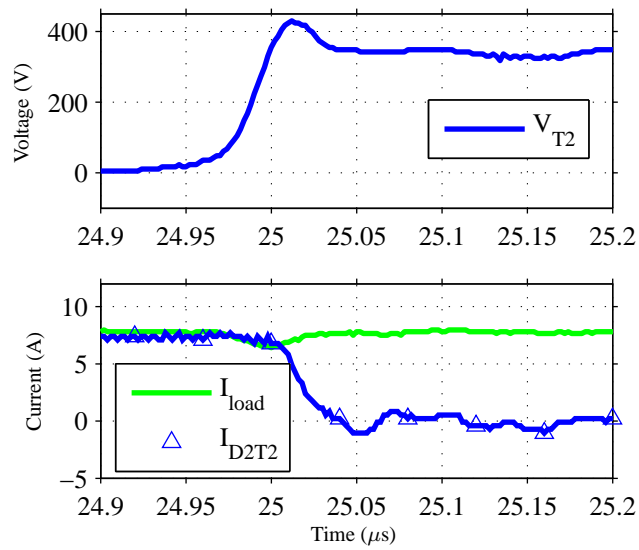


Fig. 8.14 Switching transition for the turn off of T2, for a constant load current of 7.5A.

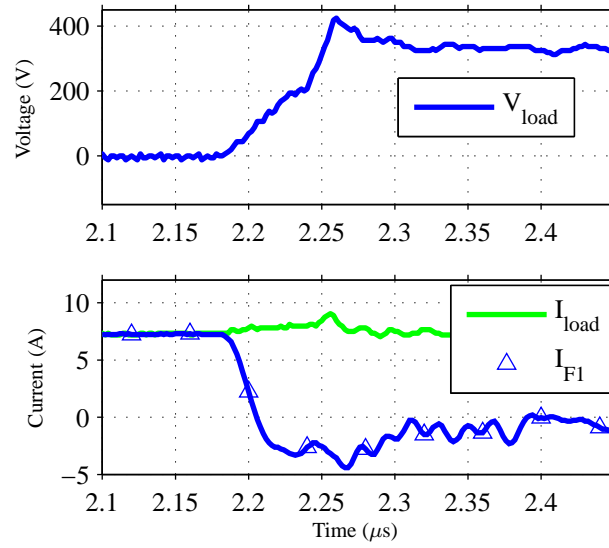


Fig. 8.15 Switching transition for F1 at turn off of T2, for a constant load current of 7.5A.

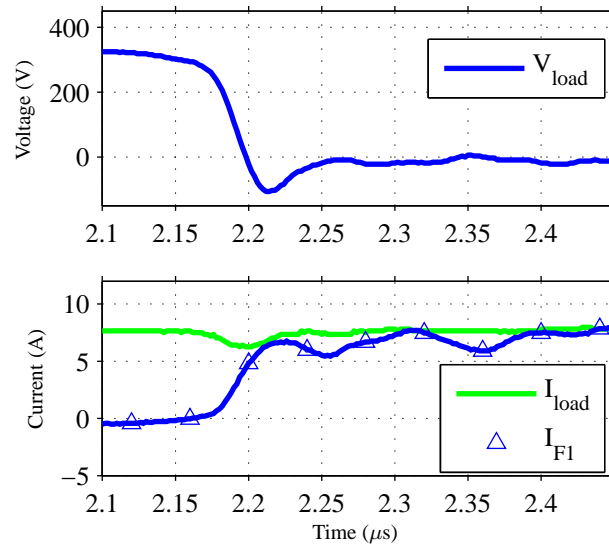


Fig. 8.16 Switching transition for F1 at turn off of T2, for a constant load current of 7.5A.

8.5 Measurements of the frequency converter losses at IM operation

This section will present the results from the measurements of the losses in the converter using different switching techniques. The converter is controlled in an open-loop manner with a constant voltage frequency ratio and a constant DC-link voltage of 330V (330 since the motor is delta connected, giving the rated AC voltage for the motor of 230V at 50Hz). Furthermore, the switching frequency is 20kHz during the tests, if not stated otherwise.

A linear load was chosen, $T_L = b\omega$, giving rated operation at rated voltage/frequency. The cooling fan of the converter was operated in the same state as during the temperature calibration. Each measurement was performed after 6 minutes of operation followed by 15 minutes of forced cooling. This procedure ensured a stable temperature on each component and enough cooling to retain the ambient temperature of the components at the start of each measurement point. The oncoming sections presents obtained results.

8.5.1 SVM

This section will present the result obtained using SVM. The measurements will be compared with calculation of the different loss components presented in Sections 8.2 and 8.4.

Table 8.3 and 8.4 shows the detailed results from the measurement. Note that the power dissipation in the components presented in Table 8.4 is given for one single component.

Table 8.3 Measurement data

T_{Load} (Nm)	n (rpm)	V_{fun} (V)	I (A)	$\cos(\varphi_1)$	P_{IM}	P_{dc}
7.88	437.9	36.6	8.4	0.53	498	600
10.50	584.2	49.3	9.3	0.59	817	933
13.12	730.8	62.3	10.2	0.64	1242	1357
15.75	876.6	74.8	11.2	0.69	1743	1872
18.38	1022	87.3	12.3	0.73	2345	2490
21.00	1167	99.2	13.4	0.76	3023	3182
23.62	1312	111.3	14.5	0.78	3798	3965
26.25	1456	122.8	15.7	0.8	4652	4847

Figures 8.17 show the measured losses in the transistors, T1-T6, together with the different calculated loss components. The calculations were done by using the measured currents and the on-state voltage. P_T , P_{swT} and P_{cT} refers to the measured losses, the calculated switching losses and the conductive losses respectively. The results indicates an accurate estimation of the different loss components. However, to strengthen the validity, further measurements have been performed in order to separate the switching and the conductive losses, which will be presented in Section 8.5.2.

8.5. Measurements of the frequency converter losses at IM operation

Table 8.4 Measurement data

T_{Load} (Nm)	ΔT_T (°C)	P_T (W)	ΔT_D (°C)	P_D (W)	ΔT_F (°C)	P_F (W)
7.88	12.5	3.0	17.7	2.0	19.6	4.9
10.50	13.8	3.3	19.3	2.2	22.0	5.8
13.12	17.5	4.0	18.4	2.1	21.6	5.6
15.75	19.6	4.5	19.6	2.3	22.7	6.0
18.38	23.2	5.4	21.3	2.4	22.2	5.8
21.00	26.7	6.2	23.1	2.5	23.3	6.1
23.62	33.2	7.8	26.3	2.7	24.0	6.2
26.25	49.7	11.5	29.0	3.0	25.1	6.4

Figures 8.18 and 8.19 shows the results for the freewheeling diodes, F1-F6, and the series diodes, D1-D6, respectively. It can be noted that the calculated and the measured losses for D1-D6 indicates a fairly accurate estimate. The losses in F1-F6 on the other hand does not show the same trend, possible causes are further analyzed in Section 8.5.2.

Figure 8.20 shows the measured losses with the input output method, meaning that the losses are determined from the difference in the measured input and output power to the converter, together with the calculated and measured losses using the temperature of each component. Note that the so called bleeding losses, namely the losses in the converter at 330V DC link voltage when the transistors are off, is subtracted from the input power. These losses are approximately 12W and results from the power dissipation in resistors used to discharge the capacitors.

The difference can be explained by the inaccuracy in the measurements. The input and output power is relatively large compared to the losses. For example, the input and output power to the converter are 4847W and 4652W respectively at rated operation. Hence a small error in the measurement results in a large error in the loss components. At least the trend is the same. However, these results clearly indicates the usefulness of the "temperature method" used here.

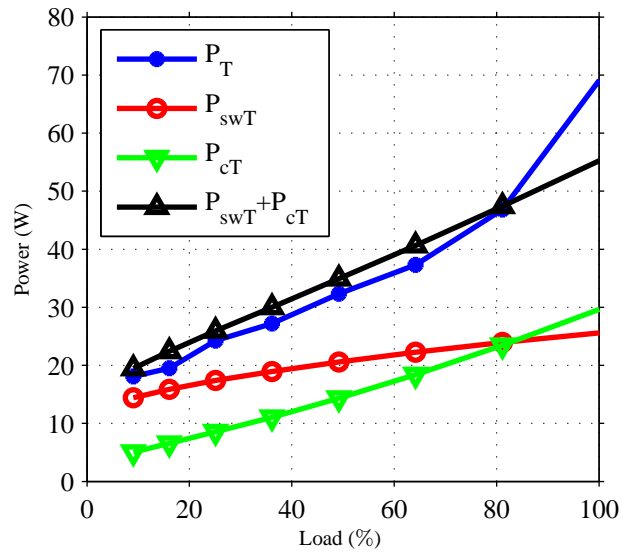


Fig. 8.17 Measured and calculated losses in the transistors (T1-T6).

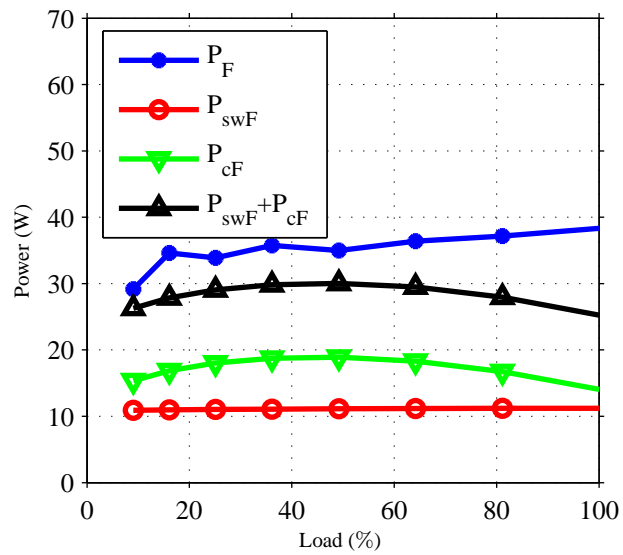


Fig. 8.18 Measured and calculated losses in the freewheeling diodes (F1-F6).

8.5. Measurements of the frequency converter losses at IM operation

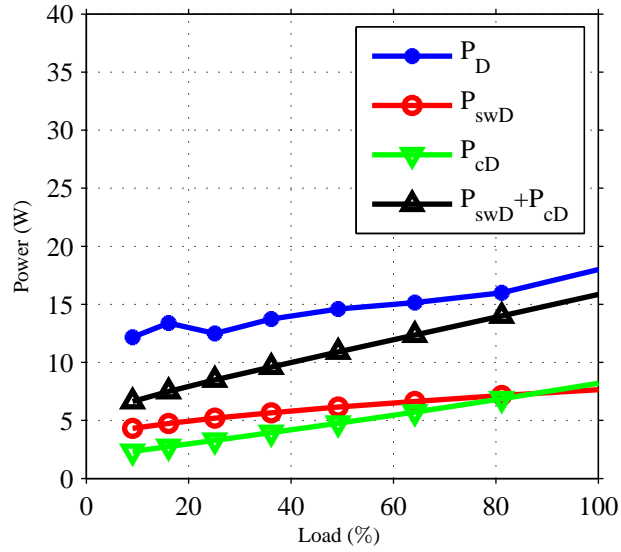


Fig. 8.19 Measured and calculated losses in the diodes (D1-D6).

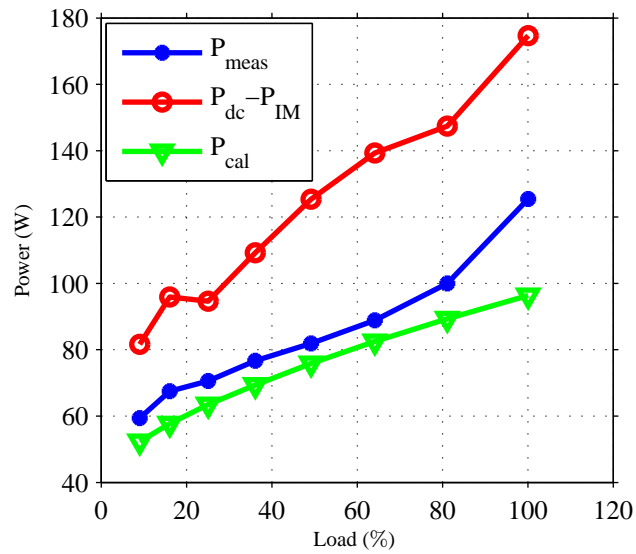


Fig. 8.20 Measured losses using input output method, temperature measurement including bleeding losses and calculated losses.

8.5.2 Varying switching frequency

In order to validate the calculations and to investigate the cause of difference between the measured and calculated losses, a series of measurements were performed for a fix load situation using different switching frequencies. The IM was operated at 40Hz and loaded with 22Nm. The same measurement procedure was then performed for switching frequencies in the range of 5kHz to 20kHz with 3kHz increments. Figure 8.21 shows the measured losses in each component together with the linear regression of the measurement points. It should be noted that the voltage decreases with approximately 2% from 5kHz to 20kHz due to the blanking time at each switching instant. However, it was not possible to distinguish any difference in the phase current between the different measurements. Hence, the conductive losses are assumed to be constant and can be obtained from the linear regression. Table 8.5 presents the calculated and the measured conductive losses.

Table 8.5 Conductive losses

Component	Measured (W)	Calculated (W)
T1-T6	20.5	19.3
D1-D6	10.3	5.9
F1-F6	10.9	18.7

It can be concluded that the calculated conductive losses in the transistors are close to the measurement. The cause of the difference in the measurement and calculation for D1-D6 and F1-F6 has not yet been established.

The accuracy in the switching losses can be evaluated by calculating the slope of the linear regression curves and the calculated loss curve. Table 8.6 presents the calculated and the measured slope of the loss curves. Again, the calculated and estimated losses in T1-T6 are close in magnitude. Furthermore, the estimated switching losses in D1-D6 are also fairly close whereas the switching losses in the freewheeling diode differs substantially from the measurement. The reason for this is unknown and is a subject for further research.

Table 8.6 Energy loss change with frequency

Component	Measured (W/kHz)	Calculated (W/kHz)
T1-T6	0.92	1.15
D1-D6	0.25	0.34
F1-F6	1.33	0.56

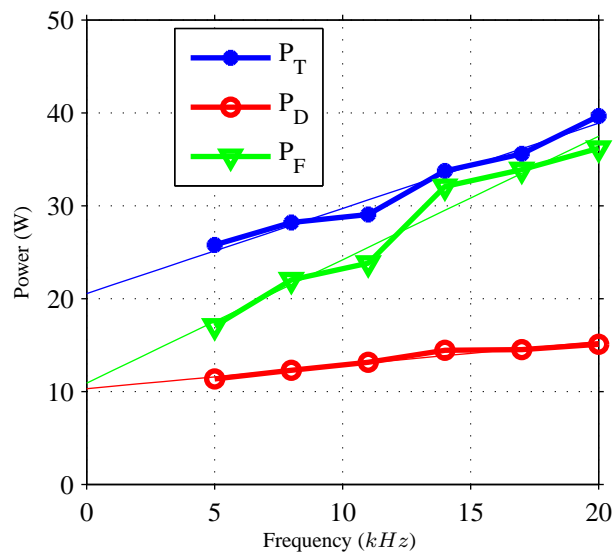


Fig. 8.21 Measured losses in the different components together with a linear regression of the measurement points.

8.5.3 DPWM60 and DPWM30

The same measurements were performed for the switching reduction strategies DPWM60 and DPWM30lag presented in Section 5.3.

8.5.4 Comparison of the different switching schemes

The measured losses in the components for the different PWM schemes are presented in figure 8.22. The result clearly shows a decrease in the losses when changing from SVM to DP60 as expected. The losses decreases further for DP30 which also is in correspondence with the expectations.

Figure 8.23 shows the losses normalized to SVM.

In order to compare the measurements with the simulations made in Chapter 5 the losses in T1-T6 are considered. The calculated conductive losses for T1-T6 are subtracted from the measurement, since only the switching losses were accounted for in the simulation. Figure 8.24 shows the measured switching losses together with the simulated switching losses in the transistor. It can be noted that the simulation are in agreement with the measurement. Figure 8.25 shows the efficiency of the converter using the sum of the measured output power and the power dissipation obtained from the temperature measurement as input power.

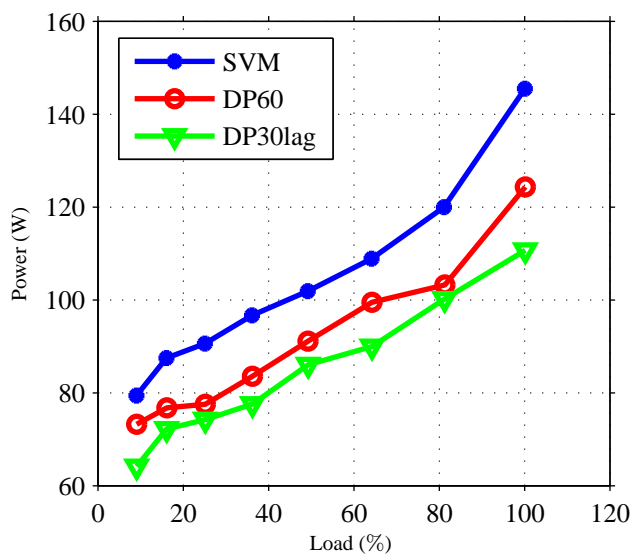


Fig. 8.22 Measured losses at the different switching schemes.

The total efficiency of the drive system are presented in figure 8.26. It can be noted that only the load at 30-50Hz are presented in order to see a difference between the different setups.

8.5. Measurements of the frequency converter losses at IM operation

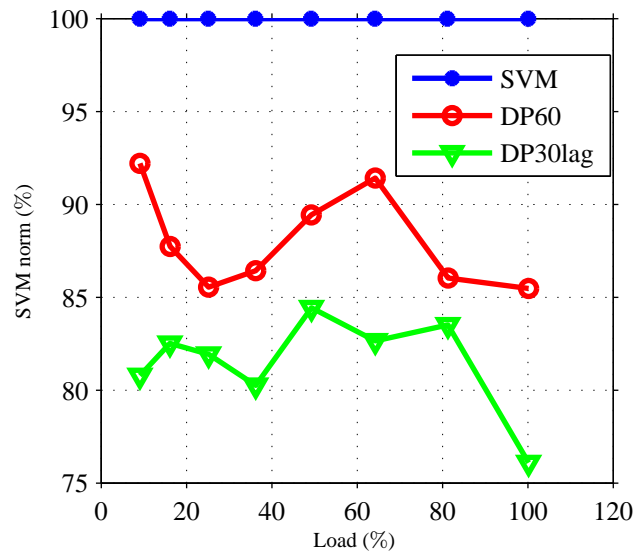


Fig. 8.23 Measured losses normalized to SVM.

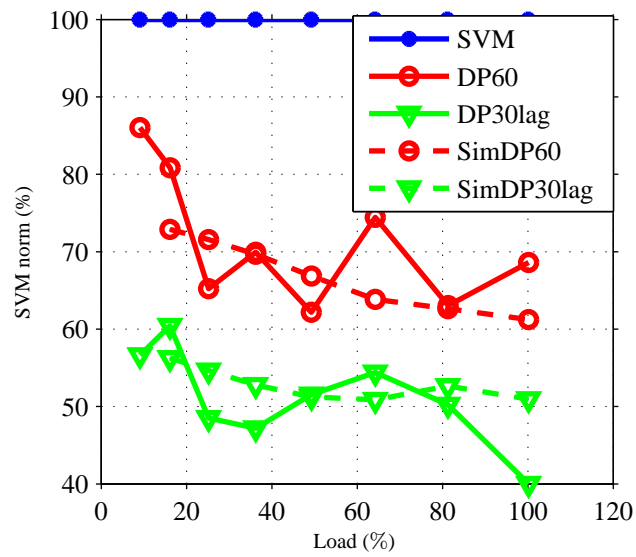


Fig. 8.24 Simulated and measured switching losses in the transistors normalized to SVM.

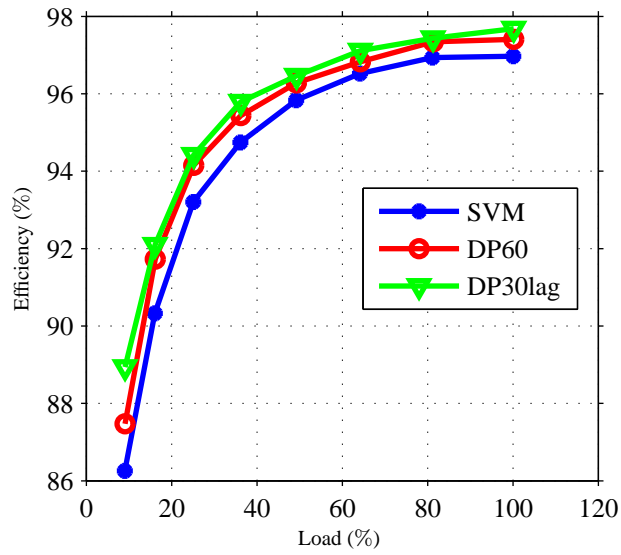


Fig. 8.25 Measured converter efficiency for the different switching schemes.

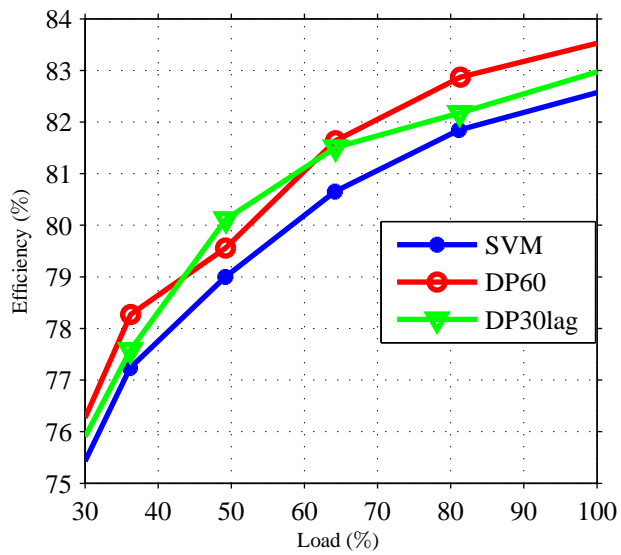


Fig. 8.26 Efficiency of the drive system.

8.5.5 Influence on IM efficiency

The difference in the IM efficiency between different switching schemes was not possible to determine from the input output method. However, the difference can be estimated from the difference in harmonic losses between the switching schemes. Figure 8.27 shows the measured harmonic content in the active power. It can be noted that the continuous SVM has lower harmonic losses as expected. The maximum difference is however only 5W. However, the result is not in accordance with the theoretical harmonic estimation presented in Chapter 5 which will be a topic for future work.

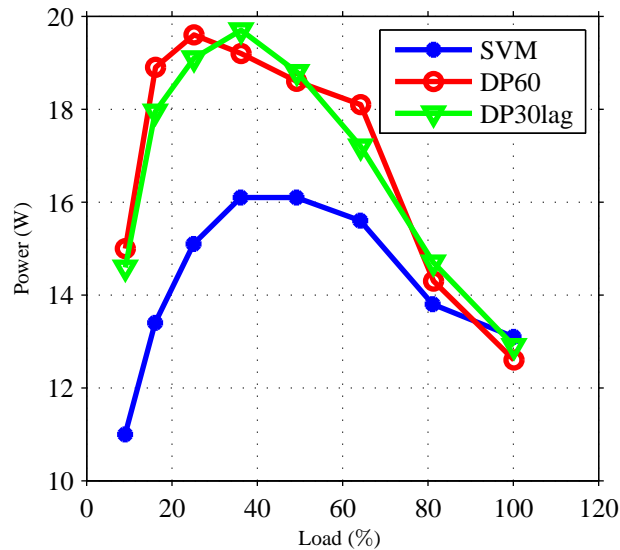


Fig. 8.27 Measured harmonic losses for SVM and DP30lag.

In order to validate the accuracy in the harmonic loss measurement, the IM was fed by a generator providing a pure sinusoidal voltage with variable voltage and frequency. Measurement were performed at no load operation, for SVM converter control and for the generator supply, with equal fundamental frequency and voltage. The no load operation was chosen in order to achieve a well defined operation. The measured harmonic losses was negligible when the IM was fed from the generator ($< 0.2\text{W}$). Furthermore, by comparing the fundamental power between the two cases, which ideally should be identical, it was found that the difference was at maximum 3%. The harmonic power component were further in close correlation to the result presented in figure 8.27.

8.6 Efficiency measurements at optimal V/Hz operation

This section will present the results from the measurements made with optimal V/Hz control of the IM.

Measurements were performed for a quadratic load characteristic, $T_L = b\omega^2$, having rated torque at rated speed. Figure A.15 show the efficiency for constant V/Hz and for optimal V/Hz ratio together with the simulated result presented in Chapter 5.

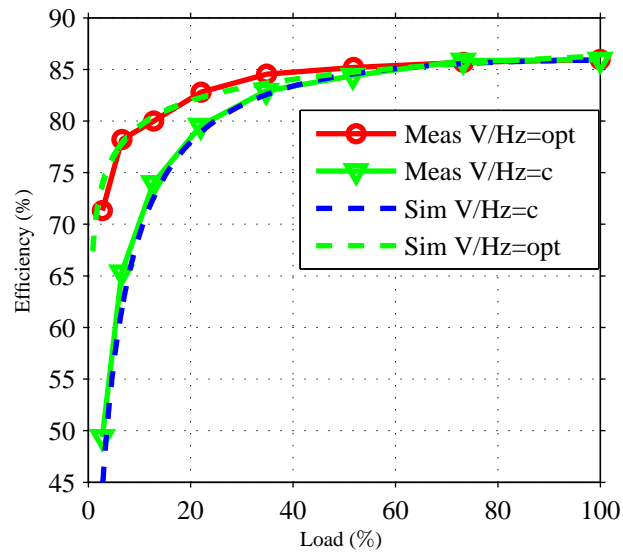


Fig. 8.28 Measured and calculated efficiency using constant V/Hz and optimal V/Hz control.

Chapter 9

Experimental investigation of BLDC and PMSM drives

This chapter will present the measurement results made on the 375W BLDC and the 4kW PMSM motor analyzed in Chapter 6. Furthermore, comparison with the measurement result of the eff1 4kW IM presented in Chapter 8 be presented for comparison. Finally, the measurement result of the 1.2kW PMSM and BLDC motors presented in Chapter 7 will be presented.

9.1 Measurement setup of 375W

This section will present some key results obtained from the measurements made. Due to the lack of detailed motor data, as described in Chapter 6, the absolute accuracy between the simulations and measurements are expected to show a difference. Due to this fact the measurements will only be presented to a show similar trend compared to the simulations. For a more detailed analysis of the simulation accuracy compared to measurement refer to section 9.6

The motor was fed by the frequency converter built for the IM testings presented in Chapter 8. The current control was made identical to the one presented in section 6.1.2. The motor was mounted in a breaker, measuring the torque and speed of the motor. Table 9.1 presents the measurement equipment used during the test.

The load was adjusted to have a linear characteristic with a load constant of 0.03 for all operating points. The current reference was set to 0.5-3.5 in steps of 0.25. Each measurement was started with the motor having the ambient temperature of 20-22°C. Each measurement point were made after 1min of operation taking 30 measurement samples. After each operating point, the stator resistance was measured.

The friction losses is, according to Section 6.2, $P_{fric} = bw_r$, where b is calculated to give 5W losses at 1000rpm.

Table 9.1 Measurement instruments

Type	Measured quantities
Norma 61D2 3-phase power analyzer	$I_{a,b,c}, U_{a,b,c}, P_{a,b,c}$
Lecroy digital Oscilloscope 9304 CM	$I_{a,b,c}, U_{a,b,c}, I_{dc}, V_s$
Lecroy Differential voltage probe AP032	U_{abc}, V_s
Lecroy Current probe AP015	I_{abc}, I_{dc}
Vibro-meter FW865	T_e

9.2 Measurement results of the original 375W BLDC

Figure 9.1 shows the current waveforms for two different operating points, 1A and 3.25A current reference respectively. It can be noted that the behavior is similar to the result presented in Chapter 6. One difference that is worth to point out is the current ripple which are higher in the measurements. This can partially be explained by the uncertainty of the motor material but also that the BH-curve used in the simulation only take one frequency component into account, as explained in Chapter 3.

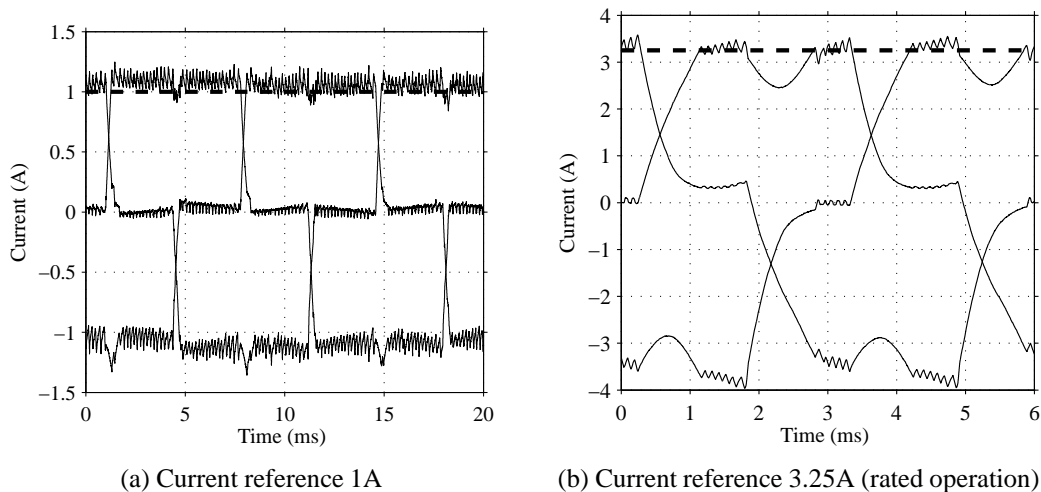


Fig. 9.1 Example of phase currents of the BLDC motor operated at two different speeds, when connected to a linear load $T=b\omega$

Figure 9.2 shows the efficiency of the motor when operated with ICP and BLDC current control. It can be noted that the behavior is similar to the result obtained in Chapter 6, namely that the efficiency when operated with ICP becomes larger than for the BLDC control at higher load lower at light load. The large drop in efficiency at light load for the ICP control can be explained by the iron losses which was found to be higher for the ICP case, in accordance with the simulations. Figure 9.3 shows the calculated iron losses from the measurements.

The increase in efficiency for the ICP at higher load is due to the loss in controllability

9.2. Measurement results of the original 375W BLDC

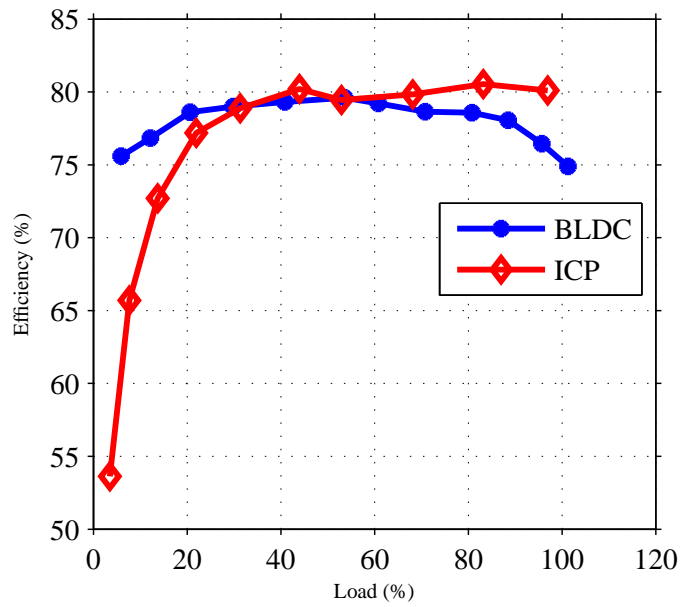


Fig. 9.2 Measured efficiency of the 375W BLDC motor when operated with BLDC and ICP current control.

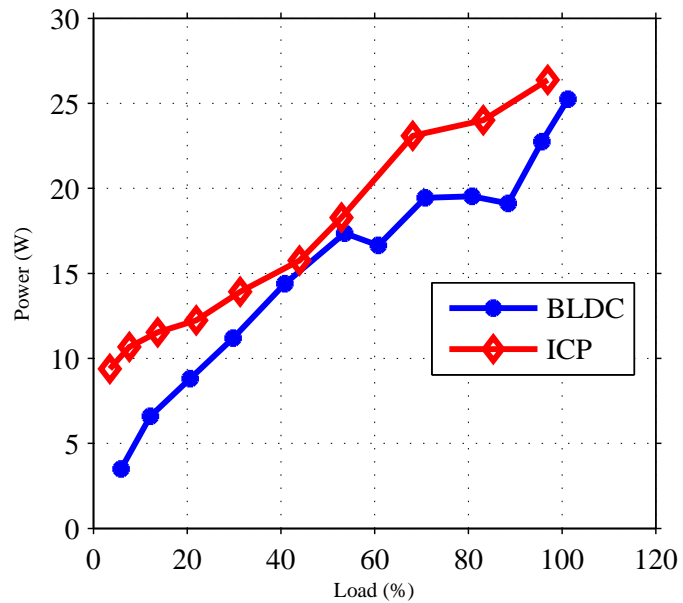


Fig. 9.3 Measured iron losses of the 375W BLDC motor when operated with BLDC and ICP current control.

of the BLDC current control as was shown in figure 9.1. This can also be seen in figure 9.4 where the difference in torque/current becomes larger for the ICP control at higher load.

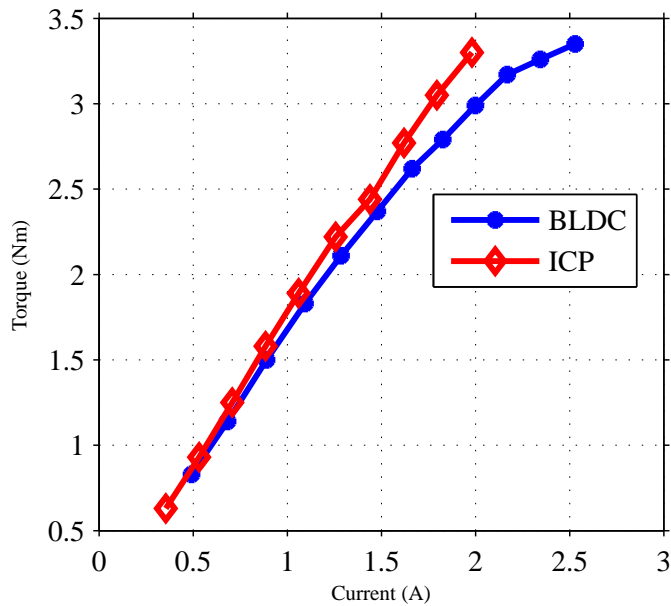


Fig. 9.4 Measured torque and current of the 375W BLDC motor when operated with BLDC and ICP current control.

9.3 Measurement setup for the 4kW PMSM

The 4kW PMSM motor was operated using the associated frequency converter. Each measurement point was made after 1min of operation, starting from the ambient temperature. The DC resistance was measured after each operating point. The measurement setup, described in Section 9.1, was now modified. The motor was loaded with a DC machine and the torque was measured with a GmbH DR2212 torque transducer. Figure 9.5 shows the efficiency of the motor having a quadratic load characteristic, $T=b\omega^2$, providing 4kW at 1455rpm. The figure also include the measurement result on the 4kW eff1 IM for comparison, using the same measurement procedure. It can be noted that the efficiency of the PMSM motor is higher in the whole operating range. This result will be used in Chapter 10 in order to exemplify the potential saving for different HVAC load profiles.

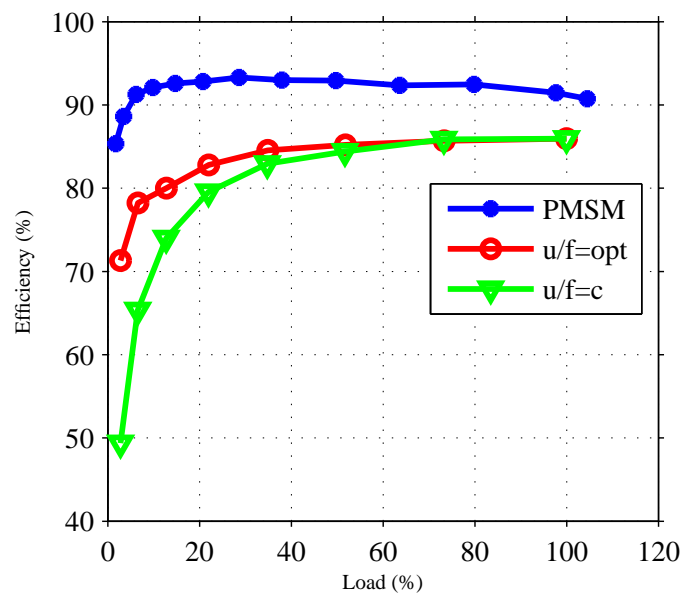


Fig. 9.5 Measured efficiency of of the 4kW PMSM and IM motor when connected to identical load characteristics, $T=b\omega^2$, providing 4kW at 1455 rpm (100% load).

9.4 Measurement results of a 1.2kW PMSM and BLDC motor

This section will present the measurement results of the 1.2kW PMSM and BLDC motor presented in Section 7.3. The measurement setup and procedure used for the 4kW PMSM, presented in section 9.3, will be used. The load torque has a quadratic speed dependence providing 1.2kW at 1000rpm. The inverter is operated with Dspace, where the BLDC and ICP control scheme are implemented as described in Chapter 6. The friction losses is, according to Section 7.3.1, $P_{fric} = b\omega_r^2$, where b is calculated to give 6W losses at 1000rpm.

9.4.1 1.2kW PMSM

The PMSM motor is operated with the ICP control, having an updating frequency of 20kHz. The stator resistance is measured for each operating point and used as an input in the simulation. This is made in order to get a more accurate estimation of the stator resistance due to the difficulty in temperature determination. Figure 9.6 shows the efficiency for the measurement together with the simulation result. It can be noted that the calculations are in good agreement with the measurement.

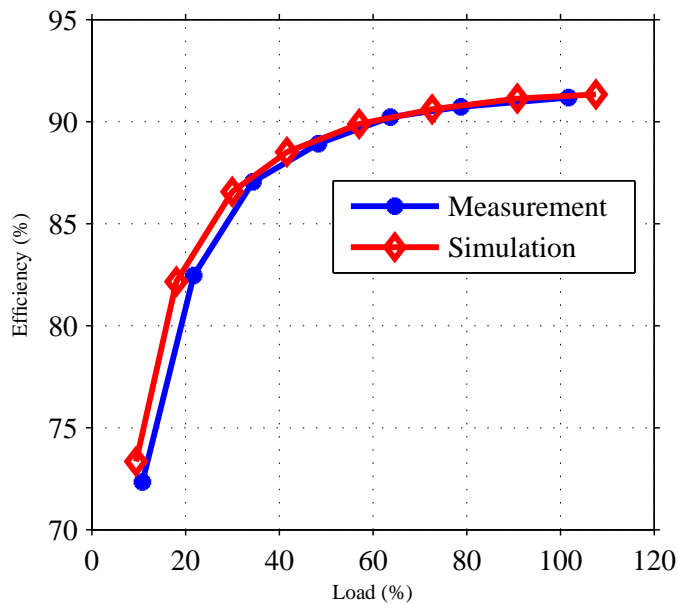


Fig. 9.6 Measured and simulated efficiency of the PMSM motor controlled with ICP. The motor is connected to a quadratic load characteristics, $T=b\omega^2$, providing 1.2kW at 1000 rpm (100% load).

Figure 9.7 shows the measured and simulated iron losses in the stator core and the copper losses in the windings for the same load situation. The core losses for the ideal

case, neglecting the inverter supply and feeding the motor with pure sinusoidal currents, is included for comparison. The result clearly shows that it is important to include the harmonic consequences of the inverter supply in the calculations, since the ideal, (sinusoidal), calculated iron losses are far from the measured result. It should also be pointed out that the so called measured iron losses are the remaining losses after subtracting the copper and mechanical losses, making it a difficult task to get an accurate iron loss measurement.

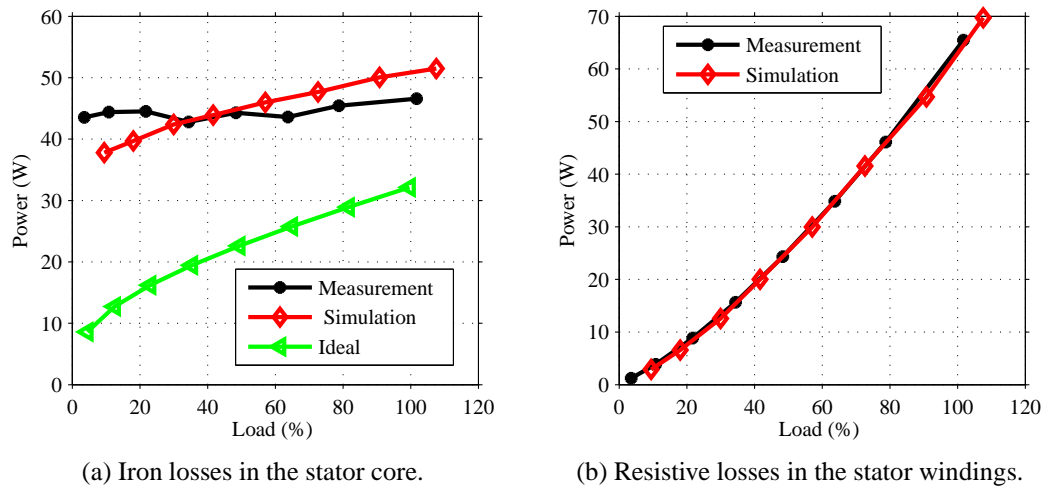
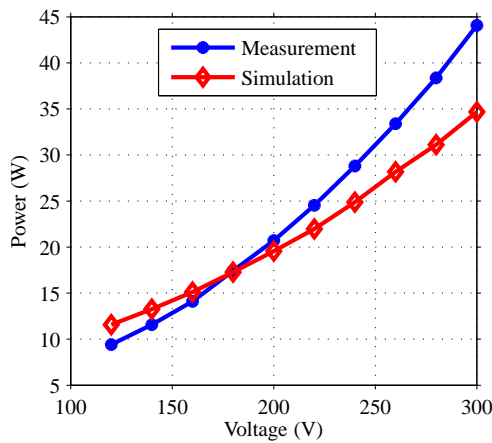


Fig. 9.7 Measured and simulated resistive losses and iron losses for the 1.2kW PMSM motor controlled with ICP. The motor is connected to a quadratic load characteristics, $T=b\omega^2$, providing 1.2kW at 1000 rpm (100% load).

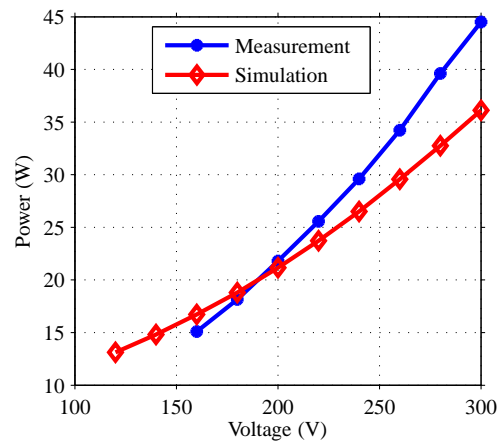
Iron loss evaluation

In order to investigate the accuracy regarding the iron loss calculation different simulation and measurement setups have been made. At low load, the current ripple is relatively high due to the large difference in induced voltage and DC bus voltage. Due to the complex nature of the iron losses it is interesting to investigate whereas the iron losses caused by the current ripple are accurately modeled. Figure 9.8 shows the simulated and the measured iron loss component in the motor when varying the DC bus voltage. The measurements and simulations are made for two setups, 320rpm and 44W output power and 400rpm 130W output power. When the DC bus voltage decreases the current ripple decreases. It can be noted that the deviation in predicted iron losses are similar between the two cases. It can further be concluded that the accuracy in the iron loss determination is fairly low. However, due to the many factors neglected the result still gives a good indicator on how the DC bus voltage affects the iron loss component. It should again be pointed out, that if the iron losses were calculated, neglecting the iron losses arising from the inverter

supply, the calculated iron losses would be constant only 1/3 of the actual iron losses at 300V DC bus voltage.



(a) 320rpm, 44W of output power.



(b) 400rpm, 130W of output power.

Fig. 9.8 Measured and simulated iron losses at two different constant speeds and output power when varying the DC bus voltage.

9.4.2 1.2kW BLDC

The BLDC was connected to identical load as the 1.2 kW PMSM and identical measurement procedure where performed. Figure 9.9 shows the resistive losses in the stator windings and the iron losses in the stator core. It can be noted that the measurement match well with the simulation result.

Figure 9.10 shows the measured and simulated efficiency. It can be noted that the efficiency is approximately 91.2% and 91.8% in the measurement and simulation respectively. Hence the difference is approximately 0.6% or 7W of the rated power which can be considered to be in good agreement of the expectations.

Finally, figure 9.11 shows the efficiency of the BLDC and PMSM motor. It can be noted that the difference is almost negligible at rated operation. However, the efficiency of the drive system can be expected to be larger for the BLDC case due to the lower amount of switching losses in the inverter stage.

9.4. Measurement results of a 1.2kW PMSM and BLDC motor

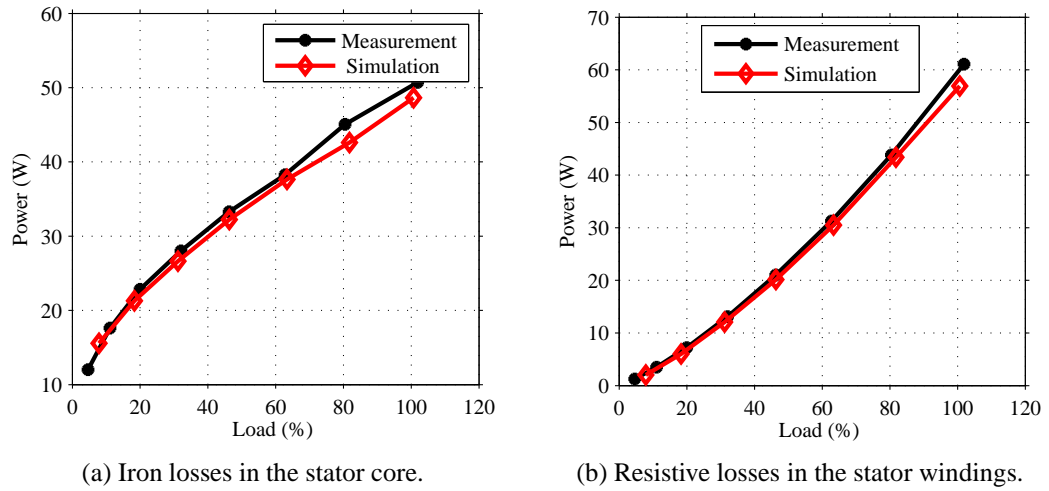


Fig. 9.9 Measured and simulated resistive losses and iron losses for the 1.2kW BLDC motor. The motor is connected to a quadratic load characteristics, $T=b\omega^2$, providing 1.2kW at 1000 rpm (100% load.)

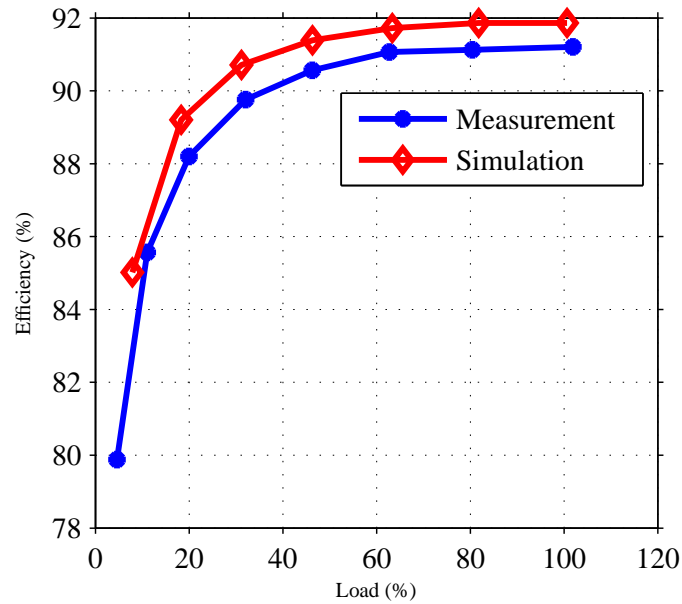


Fig. 9.10 Measured and simulated efficiency of the BLDC motor. The motor is connected to a quadratic load characteristics, $T=b\omega^2$, providing 1.2kW at 1000 rpm (100% load).

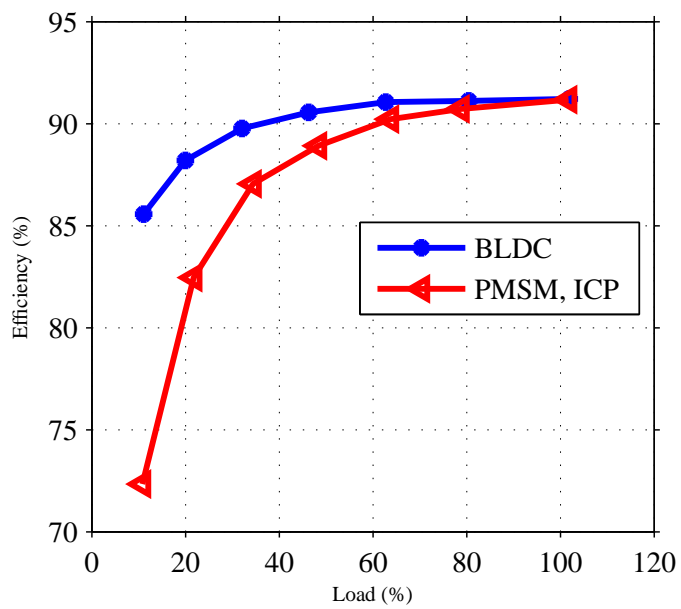


Fig. 9.11 Measured efficiency of the PMSM and BLDC motor. The motor is connected a quadratic load characteristics, $T=b\omega^2$, providing 1.2kW at 1000 rpm (100% load).

Chapter 10

Energy potential savings for different load profiles

This chapter will use the theory presented in previous chapters in order to estimate the potential saving for different load profiles, associated to various HVAC applications. Different motor controls, motor designs and dimensioning aspects will be considered.

10.1 Energy consumption calculation

The annual energy consumption of a drive system can be calculated as

$$W = \int_0^{8760} p_{in}(t) dt \quad (10.1)$$

where $p_{in}(t)$ is the power demand as a function of time and 8760 is the number of hours during a year. The electric input power to the drive system and the time duration of each load situation will be determined from the load profiles described in Chapter 2. Each profile consists of a different number of constant levels resulting in different power demands. Given each power demand and time distribution, the energy consumption can be calculated as

$$W = \int_0^{t_1} P_1 + \int_0^{t_2} P_2 + \dots + \int_0^{t_n} P_n \quad (10.2)$$

where t_1, t_2, \dots, t_n is the time duration of the electric power input P_1, P_2, \dots, P_n .

10.2 Induction motor drive setups

Chapters 5 and 8 analyzed different setups of an IM drive. The loss model valid for different energy labels, eff1-eff3, using constant and optimal V/Hz control will be used in order to estimate the potential savings for different load profiles.

For the applications described in this thesis, it is assumed that the pump/fan speed is proportional to the flow, according to the affinity laws. This means that it is assumed that the torque demand of the pump/fan is proportional to the square of flow. Assuming a constant pump/fan efficiency, the torque speed demand of the driving motor can be derived from a given load profile, Q ,

$$\mathbf{n} = n_N \frac{Q}{Q_{max}} \quad (10.3)$$

$$\mathbf{T} = T_N \frac{Q^2}{Q_{max}^2} \quad (10.4)$$

where n_N and T_N is the rated speed and torque respectively and Q_{max} is the maximum flow resulting in rated motor operation.

It should be pointed out that the assumption that the efficiency of a pump/fan is constant underestimates the potential saving. This is due to the fact that the actual power demand will be higher since the efficiency of the pump/fan decreases at lighter load.

In order to investigate the influence of IM dimensioning, the load demand, using the same pump/fan speed, will be decreased, meaning that the torque demand of the pump/fan will be decreased. The dimensioning will be referred to as the percentage of the original flow demand, e.g. a dimensioning of 80% corresponds to a decrease of the flow to 80% which means that the torque will decrease to 64% of its original value.

It should also be noted that in order to compare the different types of energy labels, identical operating points needs to be considered. Hence, the input parameters are the speed and torque demand, where the maximum is set to 1435 rpm and 26.6Nm corresponding to rated operation for the eff3 IM. As a result, the same operating point for the eff2 and eff1 IM will result in a slight overload since the frequency needs to be decreased 0.3-0.5Hz from the rated frequency.

Since the number of different IM ratings are limited the standard ratings of 1.1kW, 1.5kW, 2.2kW, 3kW 4kW are considered. The calculations are based on the 4kW IM and scaled to fit for the different machines. Hence, it should be noted that the efficiency is assumed to be identical for a fixed percentage of rated load. As a result, the savings made by moving down in motor size is slightly overestimated since the actual efficiency decreases with decreased motor rating.

The following subsections provides the results for different load profiles.

10.2.1 Load profile A

Load profile A was presented in Chapter 2 describing a two level load operating at 100% for two thirds of the time and at 50% for one third of the time.

Figure 10.1 shows the energy consumption for different IM setups using an eff3 with constant V/Hz control as a reference. First the eff3 IM is replaced by an eff1 IM with the same rating resulting in a 4-7% decrease in energy consumption. The next step is to move from 4kW rating to a lower rating when possible. The difference becomes evident when the dimensioning percentage decreases. Finally, both the IM and control of the IM is changed which results in the largest decrease in energy consumption. It should be noted that the consumption of the 4kW eff1 with optimal V/Hz control becomes almost identical to the smaller ratings with optimal control. This is due to the fact that the calculation for the smaller IM ratings are derived from the 4kW IM. Hence, since decreased IM rating in practice results in a decrease in efficiency, over dimensioning actually results in a lower energy consumption if the oversized IM is operated at optimal V/Hz, in accordance with the result presented in Chapter 5.

Cost analysis

The largest saving is provided when both the IM and the frequency converter is replaced. However, this also results in the largest investment. Hence, the saving potential must be related to the initial cost. It is here assumed that a frequency converter and a eff3 IM costs 1000 SEK/kW. It is further assumed that an eff1 IM costs 1500 SEK/kW and an eff2 1250 SEK/kW. The annual saving between the eff3 and eff1 class in SEK, where it is assumed that 1kWh costs 1 SEK, can be found in figure 10.2.

In order to include interest rate in the investment, the following expressions can be used in order to calculate the payback time and the total saving,

$$T_p = \frac{I_0 + \sum_{n=1}^N (I_0 - \frac{I_0}{N}n) \frac{r}{100}}{A_{save} W_{cost}} \quad (10.5)$$

$$Saving = A_{save} W_{cost} (T_{Life} - T_p) \quad (10.6)$$

where T_p is the payback time (years), I_0 is the investment (SEK), r is the interest rate (%), A_{save} is the annual saving (SEK), W_{cost} price of 1kWh (SEK) and T_{Life} is the life time of the drive system (years).

Another important fact to consider is if the drive system are to be replaced, e.g due to renovation. In that case, the cost difference between the different choices are of interest, not the total investment, this of course reduces the payback time substantially. Table 10.1 presents the payback time and the total savings that can be made assuming 20 years of operation and a 5% interest rate. Note that the investment is accounted for in the total saving. In the case where the eff2 and eff1 IM are considered, only the price difference

between the different choices are accounted for, in order to investigate if there is any reason for choosing an eff2 IM instead of an eff1 IM.

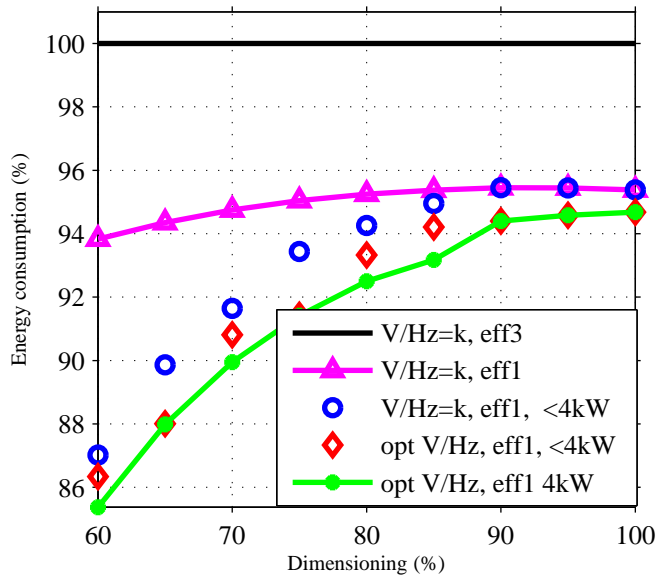


Fig. 10.1 Potential energy savings for load profile A

Table 10.1 Saving potential with load profile A

Replacement	Dim. (%)	I_0	T_p	Tot. saving	Tot. energy cost
eff3, V/f=k → eff1, V/Hz=k	100	6 000	6	20 000	589 000
eff3, V/f=k → eff1, V/Hz=k	80	6 000	9	12 000	385 000
eff3, V/f=k → eff1, V/Hz=k	60	6 000	10	8 000	234 000
eff3, V/f=k → eff1, opt V/Hz	100	10 000	9	18 000	585 000
eff3, V/f=k → eff1, opt V/Hz	80	10 000	10	15 000	375 000
eff3, V/f=k → eff1, opt V/Hz	60	10 000	11	21 000	215 000
eff2, V/Hz=k → eff1, V/Hz=k	100	1 000	2	17 000	589 000
eff2, V/Hz=k → eff1, V/Hz=k	80	1 000	3	8 000	385 000
eff2, V/Hz=k → eff1, V/Hz=k	60	1 000	4	6 000	234 000
eff2, opt V/Hz → eff1, opt V/Hz	100	1 000	2	16 000	585 000
eff2, opt V/Hz → eff1, opt V/Hz	80	1 000	3	7 000	375 000
eff2, opt V/Hz → eff1, opt V/Hz	60	1 000	6	3 000	215 000

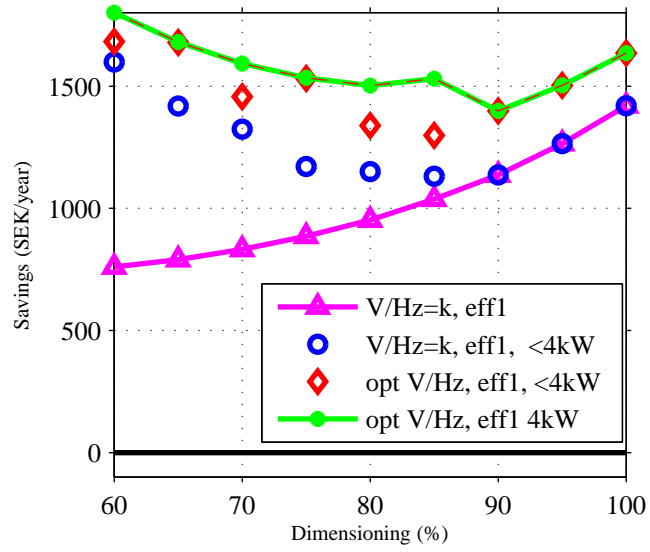


Fig. 10.2 Potential annual savings in SEK for load profile A

10.2.2 Load profile B

Load profile B was presented in Chapter 2 and describes a VAV load. Figure 10.3 shows the energy consumption for different IM setups using an eff3 with constant V/Hz control as a reference. The result becomes similar to that of the load profile A.

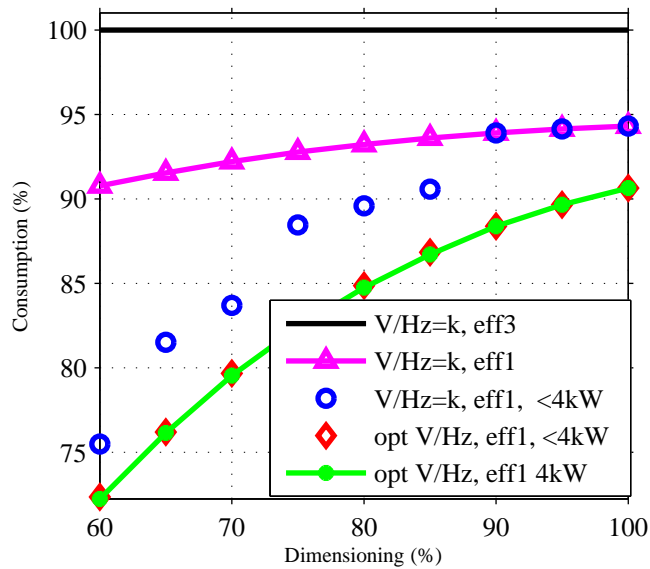


Fig. 10.3 Potential energy saving for load profile B

Cost analysis

An identical cost analysis made for load profile A is presented in figure 10.4 and Table 10.2.

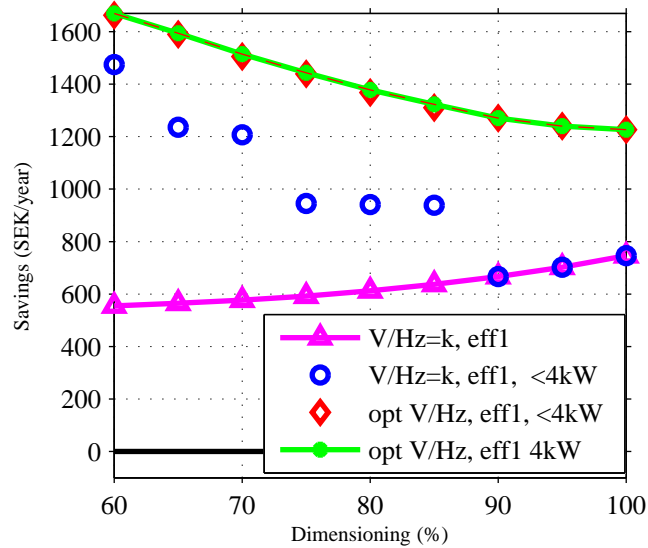


Fig. 10.4 Annual potential saving for for load profile B

Table 10.2 Saving potential with load profile B

Replacement	Dim. (%)	I_0	T_p	Tot. saving	Tot. energy cost
eff3, V/Hz=k → eff1, V/Hz=k	100	6 000	11	7 000	248 000
eff3, v/Hz=k → eff1, V/Hz=k	80	6 000	13	5 000	170 000
eff3, V/Hz=k → eff1, V/Hz=k	60	6 000	14	4 000	110 000
eff3, V/Hz=k → eff1, opt V/Hz	100	10 000	12	10 000	239 000
eff3, V/Hz=k → eff1, opt V/Hz	80	10 000	11	13 000	155 000
eff3, V/Hz=k → eff1, opt V/Hz	60	10 000	9	29 000	89 000
eff2, V/Hz=k → eff1, V/Hz=k	100	1 000	4	6 000	248 000
eff2, V/Hz=k → eff1, V/Hz=k	80	1 000	5	4 000	170 000
eff2, V/Hz=k → eff1, V/Hz=k	60	1 000	6	3 000	110 000
eff2, opt V/Hz → eff1, opt V/Hz	100	1 000	4	5 000	239 000
eff2, opt V/Hz → eff1, opt V/Hz	80	1 000	7	3 000	155 000
eff2, opt V/Hz → eff1, opt V/Hz	60	1 000	12	1 000	89 000

10.2.3 Load profile C

Load profile C describes a load with a low load demand during 80% of the time and 100% load demand for 20% of the time. Figure 10.5 shows the same setups as for profile A and B. In this case only the maximum load demand is decreased when the dimensioning are considered, since the 20% load demand already is extremely low.

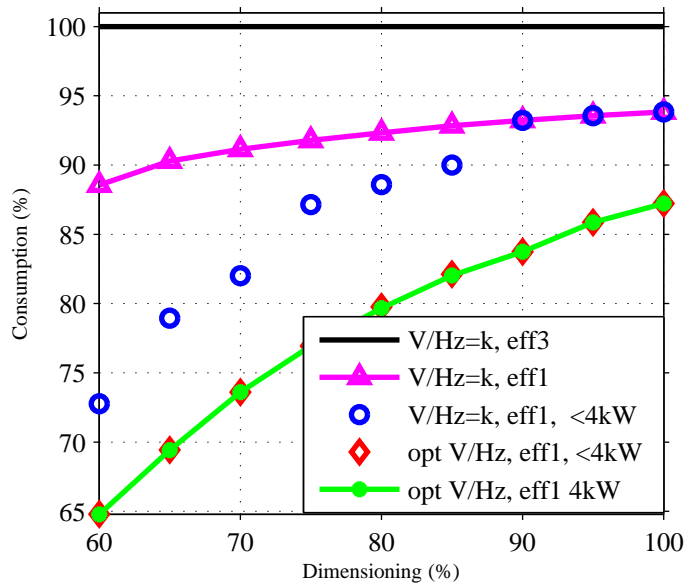


Fig. 10.5 Potential saving for load profile C

Cost analysis

An identical cost analyze made for load profile A and B is presented in figure 10.6 and Table 10.3.

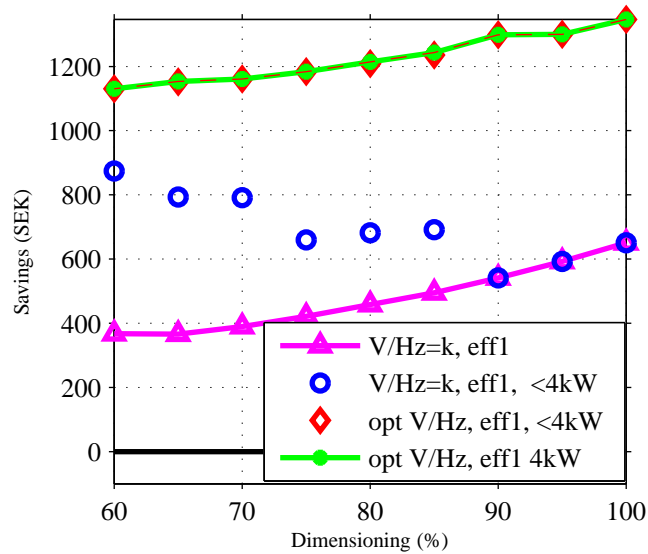


Fig. 10.6 Annual potential saving for load profile C

Table 10.3 Saving potential with load profile C

Replacement	Dim. (%)	I_0	T_p	Tot. saving	Tot. energy cost
eff3, V/Hz=k → eff1, V/Hz=k	100	6 000	13	5 000	198 000
eff3, V/Hz=k → eff1, V/Hz=k	80	6 000	16	2 000	119 000
eff3, V/Hz=k → eff1, V/Hz=k	60	6 000	20	0	72 000
eff3, V/Hz=k → eff1, opt V/Hz	100	10 000	11	12 000	185 000
eff3, V/Hz=k → eff1, opt V/Hz	80	10 000	12	10 000	105 000
eff3, V/Hz=k → eff1, opt V/Hz	60	10 000	12	9 000	57 000
eff2, V/Hz=k → eff1, V/Hz=k	100	1 000	4	6 000	198 000
eff2, V/Hz=k → eff1, V/Hz=k	80	1 000	6	3 000	119 000
eff2, V/Hz=k → eff1, V/Hz=k	60	1 000	9	2 000	72 000
eff2, opt V/Hz → eff1, opt V/Hz	100	1 000	5	4 000	185 000
eff2, opt V/Hz → eff1, opt V/Hz	80	1 000	10	2 000	105 000
eff2, opt V/Hz → eff1, opt V/Hz	60	1 000	15	500	57 000

10.2.4 Load profile D

Load profile D describes a constant load demand 100% of the time. Figure 10.7 shows the same setups as for profile A , B and C.

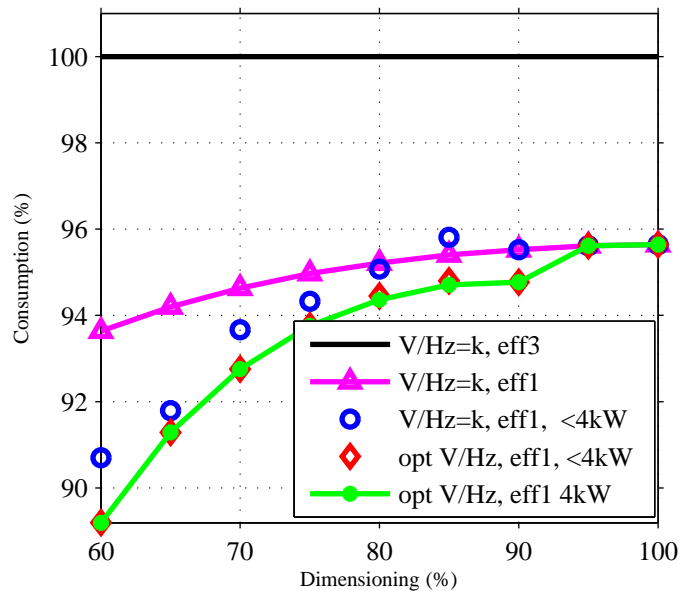


Fig. 10.7 Potential saving for load profile D

Cost analysis

An identical cost analyze made for load profiles A-C is presented in figure 10.8 and Table 10.4.

Table 10.4 Saving potential with load profile D

Replacement	Dim. (%)	I_0	T_p	Tot. saving	Tot. energy cost
eff3, V/Hz=k → eff1, V/Hz=k	100	6 000	5	28 000	821 000
eff3, V/Hz=k → eff1, V/Hz=k	80	6 000	8	14 000	426 000
eff3, V/Hz=k → eff1, V/Hz=k	60	6000	12	5 000	192 000
eff3, V/Hz=k → eff1, opt V/Hz	100	10 000	8	22 000	821 000
eff3, V/Hz=k → eff1, opt V/Hz	80	10 000	12	10 000	424 000
eff3, V/Hz=k → eff1, opt V/Hz	60	10 000	13	7 000	184 000
eff2, V/Hz=k → eff1, V/Hz=k	100	1 000	1	23 000	821 000
eff2, V/Hz=k → eff1, V/Hz=k	80	1 000	2	11 000	426 000
eff2, V/Hz=k → eff1, V/Hz=k	60	1 000	5	5 000	192 000
eff2, opt V/Hz → eff1, opt V/Hz	100	1 000	1	23 000	821 000
eff2, opt V/Hz → eff1, opt V/Hz	80	1 000	3	9 000	424 000
eff2, opt V/Hz → eff1, opt V/Hz	60	1 000	5	4 000	184 000

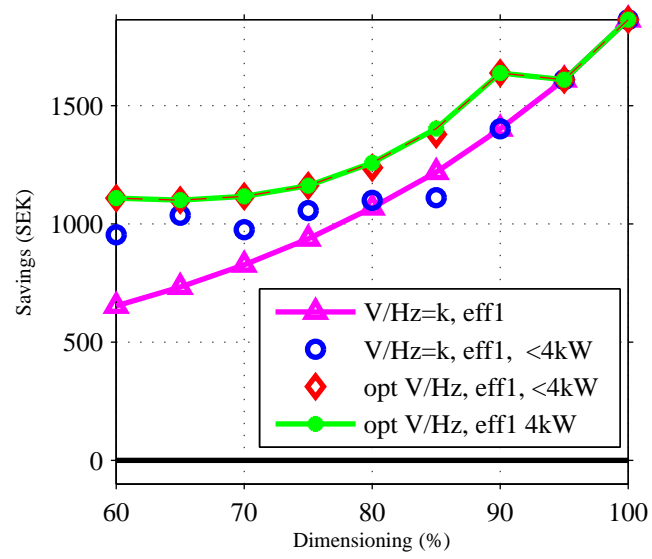


Fig. 10.8 Annual potential saving for load profile D

10.3 Evaluation of the potential saving

Load profiles A-D covers a wide range of different possible load profiles. The largest saving with an IM replacement is when the load demand is high. This becomes evident for load profile D where the load demand is high during the whole time interval. As the load demand decreases, the savings of replacing the IM decreases. The extreme case was shown with load profile C where the payback time came close to break even for a poor dimensioning. The opposite is valid for the optimal control of the IM. However, even if the energy savings are large relative to the constant V/Hz control at light load, the energy cost decreases with decreasing load. Hence, the savings does not necessarily increase as the load decreases.

When the system are to be replaced and the choice of IM is eff2 or eff1, the eff1 is the overall best choice. Again, the payback time is shorter for an application with high load demand but even for the extreme case, load profile C, savings can be made.

The analysis regarding dimensioning of the IM showed that the potential savings decreases when a smaller IM rating is used, provided that the control is optimal.

An additional factor to consider is that the efficiency of the pump/fan is assumed to be constant, as mentioned in section 10.2. As a result the potential saving is expected to be larger due to the drop in efficiency of the pump/fan at lower speeds, resulting in a higher power demand of the motor.

10.4 BLDC, PMSM vs AM

4kW IM vs 4kW PMSM

This section will present a comparison between an IM drive system and the commercially available 4kW PMSM. The comparison is based on the measurements made on the 4kW PMSM, presented in Chapter 9 and the 4kW eff1 (IE2) motor operated with efficiency optimal V/Hz. In order to estimate if the the increased investment cost are acceptable the net present value (NPV) is calculated. Provided the interest rate, r , the annual saving A_{save} and the live time, T_{Life} , the maximum investment can be calculated as

$$NPV = A_{save} \left(\frac{1}{r} - \frac{1}{r(1+r)^{T_{Life}}} \right) \quad (10.7)$$

where r is expressed in decimal form.

Table 10.5 presents the annual saving in kWh for different load profiles and two different dimensioning situations, 100% and 80%. It also provides the NPV for a life time of 20 years, an interest rate of 10% and an expected energy price of 1SEK/kWh. It can be noted that annual savings can be made for all cases except in the extreme case, load profile C with dimensioning of 80%. This is due to the drop in efficiency for the PMSM

at the extremely light load. The NPV indicates that the difference in investment can be relatively large and still be profitable.

Table 10.5 Saving potential PMSM vs IM

Load profile	Dim. (%)	A_{save} (kWh)(SEK)	NPV (SEK)
A	100	2068	17600
A	80	1382	11766
B	100	1325	11280
B	80	832	7083
C	100	703	6215
C	80	-233	-
D	100	2647	22500
D	80	1995	17000

375W IM vs 375W BLDC

It is also of interest to evaluate the potential savings between the 375W BLDC motor, analyzed in Chapter 6, the modified outer rotor design and a comparable IM. Measurements on a 375W, 6 pole, standard IM have been performed, operated at efficiency optimal control. The measurement procedure and results are not presented in this thesis, but the results are used in this section in order to exemplify the possible energy saving. Table 10.6 presents the annual savings in kWh by changing between the different drive systems. It also provides the NPV using the same input parameters as before.

It should be noted that only the motor efficiency are accounted for. However, it can be expected that the loss components in the inverter stage are higher for the IM compared to the BLDC motor. The results shows that the annual saving can be increased significantly using a different BLDC motor design. The result also indicates that the payback time, due to the difference in investment cost can be expected to be relatively short.

Table 10.6 Saving potential BLDC vs IM

Replacement	Load profile	Dim. (%)	A_{save} (kWh) (SEK)	NPV (SEK)
IM vs original BLCD	A	100	409	3480
IM vs original BLCD	A	80	201	1700
Inner rotor BLDC vs outer rotor BLDC using improved iron grade	A	100	379	3220
Inner rotor BLDC vs outer rotor BLDC using improved iron grade	A	80	234	2000
IM vs outer rotor motor using improved iron grade	A	100	788	6710
IM vs outer rotor motor using improved iron grade	A	80	440	3750

Chapter 11

Concluding Remarks and future work

11.1 Concluding Remarks

In this thesis an overview of different electric drive systems and power electronic components have been presented. Furthermore, HVAC load profiles have been described in order to analyze saving potentials for different drive system setups. Focus during the analysis was placed on different IM designs, (different energy labels), different control schemes of the IM and the frequency converter. Furthermore, different permanent magnet motor topologies, motor design aspects and control strategies has been analyzed using both simulations and measurements.

11.1.1 Induction motor drive system

The analysis of potential savings using different IM and different control was based on the simulations, however measurements were used to verify the simulations over the whole operating range. The main conclusion was that the saving potential was higher for an over dimensioned IM if it was operated at optimal V/Hz. It was further observed that the potential increased with increased over dimensioning. The latter can be explained by the improved efficiency that is achieved using optimized V/Hz control at light loads. The impact of the losses in the inverter stage for an over dimensioned drive was also quantified and it could be concluded that using a converter with lower rating, compared to the over sized motor, increases the overall efficiency of the drive system. It has further been shown that the potential saving made by replacing the IM or by replacing both the IM and the converter is highly load dependent. The analysis of IM replacement was straight forward since the potential saving increases with increasing load. The worst case scenario was a break even situation when an eff3 IM was replaced with an eff1 IM for a extremely light load. The analysis has also shown that the choice between an eff2 and eff1 IM, for the given load profiles, always generate the highest economical saving for the eff1 IM. It is interesting to note that, during the time period 1998-2003, eff2 label took 86% of the

market share compared to eff1 8% and eff3 6%.

When it comes to the analysis of the difference between constant and optimal V/Hz it has been shown that the relative saving increases with decreasing load but not necessarily the absolute economical savings since the power demand decreases with decreasing load. However, the general conclusion is that economical savings will be made for all of the given load profiles except the extreme cases of load profile C and 60% load demand during.

It has further been shown that the simulated results of the switching losses in a frequency converter, using different SVM schemes, showed a close correlation compared to the measurement. In addition, it has further been shown that the simulated efficiency difference between constant V/Hz control and optimal V/Hz control reproduced with close correlation during the measurements. Regarding the loss components in the semiconductor devices, the calculation and measurements differed, to some extent, for the diode in series with the MOSFET and the freewheeling diode, whereas the calculation for the transistor was well matched with the measurement. It could be determined that the conductive losses in the series diode and the switching and conductive losses in the freewheeling diode differed from the calculated values. The reason for this cause could not be determined explicitly. Possible modification of the measurement procedure would be to isolate each component from the nearby components, extend the temperature measurement to more components using additional equipment.

11.1.2 Permanent magnet motor drive systems

Different control strategies for a commercially available BLDC motor and a PMSM motor were analyzed, using FEM calculations, and it could be concluded that the importance regarding the control strategy was significant with aspect to the efficiency of the drive system. Different sinusoidal control schemes were tested on both motors and it could be concluded that the efficiency of the drive system can be increased significantly by active zero vector placement. The main difference was at light load where simple control algorithms showed poor motor and converter efficiency compared to more complex algorithms using active zero vector placement. It was shown that the switching losses could be reduced in the converter stage and the iron losses in the motor were highly dependent on the control strategy, both for the BLDC and the PMSM.

It was further shown that the efficiency of the BLDC motor, using classical BLDC current control, could be increased by operating the motor as a PMSM at high load. Alternatively, modifying the BLDC control by change the angle of phase commutation.

Furthermore, motor design aspects has been investigated. It has been shown that by replacing the magnet material, from ceramic 8 to NdFe35, the motor size can be reduced by 80% for one commercially BLDC motor tested. However, a reduced physical motor size results in a lower efficiency.

A comparison between an inner rotor and outer rotor motor has been performed, testing different BLDC motor designs. It has been shown that the efficiency can be increased in the whole operating range and that replacement of the iron grade can be beneficial from an energy efficiency point of view.

A PMSM and a comparative BLDC motor design were also presented and manufactured for laboratory measurements. It was shown that measurements were in close agreement with the simulations. It could further be concluded that the BLDC motor had higher efficiency in the whole operating range, including the losses in the inverter stage.

11.1.3 PMSM/BLDC vs IM

The potential saving replacing an IM drive system with a PM motor has been exemplified for the 4kW PMSM. It was shown that annual savings will be made in almost all cases except for the case with an extremely light load, where the IM provided higher efficiency.

The potential saving, comparing a 375W IM and two different BLDC motor designs were exemplified. It was concluded that the difference between the inner and the designed outer BLDC motor was significant. The results further indicated that the payback time, due to the increased investment cost, can be expected to be short.

11.2 Proposals of Future Work

In this thesis many different studies have been performed, sometimes with a lack of depth. Hence, many of the proposed works will aim to go in to deeper into the different topics. The proposed studies are as follows

- Model the IM using FEM calculations and investigate the iron losses for the different SVM schemes tested.
- Investigation of DCC/DTC control of the IM, using different zero voltage vector placement strategies, and its impact on the energy efficiency using FEM calculation including frequency converter coupling.
- Investigate the impact on energy efficiency for a given load profile when different PMSM/BLDC motor ratings are used.
- Investigation of the efficiency impact on the drive system, using an active PFC frequency converter, which allows a variation of the DC-bus voltage as a function of load/speed.
- Implementing FOC on a PMSM using SVM, and zero vector placement and investigate the impact on the energy efficiency.

Chapter 11. Concluding Remarks and future work

- EMC related issues regarding different drive system setups. How will the energy efficiency be affected, when the different drive systems proposed in this thesis are adapted to fit various EMC levels and standards?
- Investigation of bearing currents in IM and PMSM motors.
- Comparative studies of a switch reluctance motor and corresponding PMSM/BLDC/IM.
- Further cost investigation, regarding motors and power electronics.

References

- [1] *Energiläget 2010, ET2010:45, Statens energimyndighet, 2010, Eskilstuna*
- [2] *Från byggsekt till byggsektor SOU 2000:44, May 2000*
- [3] Rooks, J, Wallace A, *Energy efficiency of variable speed drive systems, Pulp and Paper Industry Technical Conference, June 2003, pp) 160- 163*
- [4] Nilsson L. *Energy systems in transition-Electricity use in pumping and air-handeling systems*, LTH (Lund Institute of Technology, Thesis for lic.Eng. Lund), 1991
- [5] Nilsson L. *A system oriented assessment of electricity use and efficiency in pumping and air-handeling*, LTH (Lund Institute of Technology, Report 1 IMES/EESS Lund), 1991
- [6] Barry Crozier *Application guide AG Enhancing the Performance of Oversized Plant*, May 2000
- [7] F. Abrahamsen *Energy Optimal Control of induction Motor Drives*, Institute of Energy Technology, Alborg University, February 2000
- [8] F. Abrahamsen F. Blaabjerg, J. K. Pedersen, P. Z. Grabowski, P. Thøgersen *On the Energy Optimized Control of Standard and High-Efficiency Induction Motors in CT and HVAC Applications*, IEEE Transactions, vol. 34, No. 4 July 1998
- [9] Cao-Minh Ta, Yoichi Hori *Convergence improvement of Efficiency optimization control of induction motor drives*, IEEE, 2001
- [10] A. Lamine, E. Levi, *Dynamic induction machine modelling considering the stray load losses*, Universities Power Engineering Conference, 6-8 Sept. 2004, pp. 582-586
- [11] A. Wallace, A.Juanne, A. Nagornyy *Evaluation of stray load losses in induction motors at different supply frequencies*, Industry Applications Conference, 13-18 Oct. 2002. pp 2296-2300
- [12] D. Holmes Grahame , A. Lipo Thomas *Pulse Width Modulation for Converters Principles and Practice*, IEEE press 2003

References

- [13] Trzynadlowski, A.M.; Kirlin, R.L.; Legowski, S.F. *Space vector PWM technique with minimum switching losses and a variable pulse rate*, Industrial Electronics, IEEE Transactions on Volume 44, Issue 2, April 1997
- [14] Yu, Z. Mohammed, A. Panahi, I., *A review of three PWM techniques*, American Control Conference, 1997. Proceedings of the 1997 Volume 1, 4-6 June 1997
- [15] L. Deboy, G. Zverev, I. *Matched pair of CoolMOS transistor with SiC-Schottky diode - advantages in application Lorenz*, Industry Applications IEEE Transactions on Volume 40, Issue 5, Sept.-Oct. 2004, pp 1265 - 1272
- [16] Ozpineci, B.; Tolbert, L.M. *Characterization of SiC Schottky diodes at different temperatures*, Power Electronics Letters, IEEE Volume 1, Issue 2, June 2003, pp 54 - 57
- [17] Ozpineci, B., Tolbert, L.M., Islam, S.K., Hasanuzzaman, M. *Effects of silicon carbide (SiC) power devices on HEV PWM inverter losses*, Industrial Electronics Society, 2001. IECON '01. The 27th Annual Conference of the IEEE Volume 2, 29 Nov.-2 Dec. 2001, pp 1061 - 1066
- [18] Y. Li and H. Zhu, *Sensorless control of permanent magnet synchronous motor a survey*, Vehicle Power and Propulsion Conference, 2008. VPPC '08. IEEE, 2008, pp. 1-8
- [19] I. Junaid, K. Qudsia, Byung-il Kwon , *Improved model of the iron loss for the permanent magnet synchronous motors*, International Conference on Electrical Machines and Systems (ICEMS), oct 2010, pp 1246
- [20] C.C. Mi, G.R. Slemon, R. Bonert, , *Minimization of iron losses of permanent magnet synchronous machines*, IEEE Transactions on Energy Conversion, March 2005, vol 20, pp 121
- [21] J. Soulard, S. Meier, Y.K. Chin, *Modeling of Iron Losses in Permanent Magnet Motors with Field-Weakening Capability*, Nordic Workshop on Power and Industrial Electronics, Aug 2002
- [22] S. Iwasaki, R. Deodhar, Y.Liu, A. Pride, Z.Q. Zhu, J. Bremer, *Influence of PWM on the Proximity Loss in Permanent Magnet Brushless AC MACHines*, Industry Applications Society Annual Meeting, 2008. IAS '08. IEEE, pp. 1-8
- [23] S. Iwasaki, R. Deodhar, Y.Liu, A. Pride, Z.Q. Zhu, J. Bremer, *Investigation of Proximity Losses in a High Speed Brushless Permanent Magnet Motor*, Industry Applications Conference, 2006. 41st IAS Annual Meeting. Oct 2006, vol 3, pp. 1514

- [24] Z.Q. Zhu, K. Ng, N. Schofield, D. Howe, D. *Improved analytical modelling of rotor eddy current loss in brushless machines equipped with surface-mounted permanent magnets, IEE Proceedings Electric Power Applications, Nov. 2004, vol. 151 pp. 641*
- [25] Aníbal T. De Almeida João L. C. Marinho Fernando J. T. E. Ferreira Paula Fonseca *Inception Report: Analysis of existing technical and market, 2006, ISR-University of Coimbra*
- [26] A. T. de Almeida *Electric motor standards, ecodesign and global market transformation, Industrial and Commercial Power Systems Technical Conference, 2008. ICPS 2008. IEEE/IAS, 2008, pp. 1-9.*
- [27] Ned Mohan, *Electric Drives an integrative approach 2003 pp 15-1 to 15-12*
- [28] Lelkes, A. Krotsch, J. De Doncker, R.W. *Low-noise external rotor BLDC motor for fan applications , Industry Applications Conference, 2002. 37th IAS Annual Meeting. Conference Record of the Volume 3, 13-18 Oct. 2002, pp 2036 - 2042, vol.3*
- [29] Lelkes, A. Bufe, M. *BLDC motor for fan application with automatically optimized commutation angle , Power Electronics Specialists Conference, PESC 04. 2004 IEEE 35th Annual Volume 3, pp 2277 - 2281, Vol.3*
- [30] Mora, J.L.V., Lelkes, A., Pacas, J.M. *External rotor PM motor fed by a load commutated inverter for fan applications , Industrial Electronics Society, IEEE 2002 28th Annual Conference, Volume 1, 5-8 Nov. 2002, pp 767 - 770*
- [31] C. B. Rasmussen, H.R. Andersen, E, Ritchie, J. K Pedersen *Design and Efficiency Comparison of Electric Motors for Low Power Variable Speed Drives with Focus on Permanent Magnet Motors, IEEE, Electrical Machines and Drives, sep 1995*
- [32] Linder, S. *Power Semoconductors, 2006: EFPL Press. 300*
- [33] N. Mohan, T.Undeland ,W.P. Robbins *Power Electronics Converters, Applications and Design,John Wiley and Sons, Inc 1995.*
- [34] M. Tack, *Energy efficient power MOSFETs, IC Design and Technology (ICICDT), 2010 IEEE International Conference on, pp. 159-163.*
- [35] J. Dodge, J. Hess, *“IGBT Tutorial”, Advanced power technology, July 1 2002*
- [36] Abel, E. Elmroth, A., *Byggnaden son system, Forskningsrådet Formas, 2006*
- [37] Hans P. Andersen *Europeans agree on energy standards for pumps, Grundfos, March 2005*

References

- [38] Karlsson A. *Behovsstyrd ventilation i lokalbyggnader; Innebörd och strömningstekniska konsekvenser*, Departement of Energy and Environment, Chalmers 2005
- [39] Danfoss *The drive to reduce Costs and Improve System Control*, May 2000
- [40] D. W. Novotny and T.A Lipo *Vector control and dynamics of AC drives*, Oxford science publications, 1996, ISBN 0 198564392
- [41] Y. Sozer, D.A. Torrey *Adaptive Torque Ripple Control of Permanent Magnet Brushless DC Motors*, Applied Power Electronics Conference and Exposition, Feb. 1998. vol1 pp15-19
- [42] Clayton R. Paul *Introduction to Electromagnetic Compatibility*, Wileyinterscience, 2006
- [43] László Tihanyi *Electromagnetic compatibility in power electronics*, 1995
- [44] Keith Armstrong *Banana skins compendium*, Cherry Clough Consultants 5th March 2007
- [45] *IEEE Standard test Procedure for Polyphase Induction Motors and generators*, March 10 1991
- [46] T. Thiringer *Measurements and Modelling of Low-Frequency Disturbances in Induction Machines generators*, , Chalmers University of Thechnology, 1996
- [47] Sozer, Y. Torrey, D.A. *Adaptive torque ripple control of permanent magnet brushless DC motors*, Applied Power Electronics Conference and Exposition, APEC '98. Conference Proceedings 1998, Thirteenth Annual Volume 1, 15-19
- [48] Jeon, Y.S. Mok, H.S. Choe, G.H. Kim, D.K. Ryu, J.S. *A new simulation model of BLDC motor with real back EMF waveform*, *Computers in Power Electronics, The 7th Workshop on 16-18 July 2000*, pp 217-220
- [49] D. Lin, P. Zhou, W. N. Fu, Z. Badics, Z.J. Cendes *A dynamic core loss model for soft ferromagnetic and power ferrite materials in transient finite element analysis*, *IEEE Transactions on Magnetics*, April, 2004, vol. 30, pp. 1318
- [50] S. Park, T. Kim, S. Ahn, D. Hyun *An Improved Current Control Method for Torque Improvement of High-Speed BLDC Motor*, , Applied Power Electronics Conference and Exposition, 2003. APEC Eighteenth Annual IEEE, 9-13 Feb. 2003, vol. 1 pp. 294
- [51] J. Holtz *Pulse width Modulation - A Survey*, *IEEE Transactions on Industrial Electronics*, vol.39 no 5, December 1992, pp 410-420

- [52] K. Zhou, D. Wang, *Relationship between Space-Vector Modulation and Three-phase Carrier based PWM: A Comprehensive Analysis*, *IEEE Transactions on Industrial Electronics*, vol.49 no 1, February 2002, pp 410-420
- [53] C.Rossi A. Tonielli *Robust Current Controller for Three-Phase Inverter Using Finite-State Automaton*, *IEEE Transaction on Industrial Electronics*, vol. 42, no. 2, April 1995
- [54] Y.Wang, J.G.Zhu Y.G.Guo *A survey of direct torque control schemes for permanent magnet synchronous motor drives*, *Power Engineering Conference, 2007. AUPEC 2007. Australasian Universities, 9-12 Dec. 2007*
- [55] I. Takahashi, T. Noguchi, *A new quick-response and high efficient control strategy of an induction motor*, *IEEE Transactions on Industry Applications*, vol.22 no 5, 1986, pp 820-827
- [56] M. Depenbrock *Direct self-control (DSC) of inverter fed induction machine*, *IEEE Transactions on Power electronics*, vol. 3 no 4, 1988, pp 420-429
- [57] L. Zhong, M.F.Rahman, W.Y. Hu, K.W.Lim *Analysis of direct torque control in permanent magnet synchronous motor Drives*, *IEEE Transactions on Power electronics*, vol. 2 no 4, 1997
- [58] E. Urlep, A. Polic, K. Jezemik *Speed Sensorless Control of PM synchronous machine using Direct Current Control*, *Power Electronics and Applications, 2005 European Conference, Dresden, 07 August 2006*

References

Appendix A

Derivation of maximum active power for non sinusoidal voltage and current

It can be shown that the maximum active power for a given RMS current is provided when the current and voltage have the same frequency components and same ratio of each component, provided that the voltage and current are in phase. This can be shown by solving the following optimization problem

$$\begin{aligned} &Max \quad \sum_{j=1}^n u_j i_j \\ &Subject \quad to \\ &\sqrt{\sum_{j=1}^n i_j^2} = k \end{aligned} \tag{A.1}$$

where u_j and i_j are the RMS voltage and current for the j^{th} frequency component.

If the condition is squared the allowed area becomes the boundary to a sphere. Further, replacing the equal sign to less than or equal sign (relaxing the problem). As a result, points inside the sphere are allowed provided that $u_j \geq 0$ and $i_j \geq 0$. The optimization problem can now be rewritten on the so called standard form as follows

$$\begin{aligned} &Min \quad - \sum_{j=1}^n u_j i_j \\ &Subject \quad to \\ &\sqrt{\sum_{j=1}^n i_j^2} - k \leq 0. \end{aligned} \tag{A.2}$$

This is now a convex problem and the optimal solution i^* is a so called KKT-point satisfying the following condition

$$\nabla f(i^*) + \lambda \nabla g(i^*) = 0 \tag{A.3}$$

$$\lambda \geq 0 \quad (\text{A.4})$$

$$g(i^*) \leq 0 \quad (\text{A.5})$$

$$\lambda g(i^*) = 0 \quad (\text{A.6})$$

$$\nabla f(i^*) = \begin{pmatrix} -u_1 \\ -u_2 \\ \cdot \\ \cdot \\ -u_n \end{pmatrix} \quad (\text{A.7})$$

$$\nabla g(i^*) = \begin{pmatrix} 2i_1 \\ 2i_2 \\ \cdot \\ \cdot \\ 2i_n \end{pmatrix} \quad (\text{A.8})$$

where λ is the Lagrange multiplier. Furthermore,

$$-u_j + 2\lambda_j i_j^* = 0 \quad (\text{A.9})$$

$$\sum_{j=1}^n i_j^{*2} - k^2 \leq 0 \quad (\text{A.10})$$

$$\lambda \left(\sum_{j=1}^n i_j^{*2} - k^2 \right) = 0 \quad (\text{A.11})$$

$$\lambda \geq 0 \quad (\text{A.12})$$

If $u_j \neq 0$, $\lambda \neq 0$. Hence $\lambda > 0$ and (A.9) can be written as

$$\frac{i_j^*}{u_j} = \frac{1}{2\lambda} \quad (\text{A.13})$$

let

$$\alpha = \frac{1}{2\lambda} > 0 \quad (\text{A.14})$$

(A.13) and (A.15) can now be inserted in (A.11)

$$\alpha^2(\sum_{j=1}^n u_j^2) - k^2 = 0$$
$$\therefore \alpha = \sqrt{\frac{k^2}{\sum_{j=1}^n u_j^2}} \quad . \quad (A.15)$$

Finally the optimal solution can be written as

$$i_j^* = u_j \alpha = \frac{k}{\sqrt{\sum_{j=1}^n u_j^2}} = u_j \frac{I_{rms}}{U_{rms}}. \quad (A.16)$$